

# **Solving inverse radiometric problems arising from infrared recordings**

by

**Stephanus Johannes Paulus Retief**



Submitted in partial fulfilment of the requirements for the degree

*Philosophiae Doctor (Physics)*

in the

Faculty of Natural & Agricultural Sciences

University of Pretoria

Pretoria

July 2018

## DECLARATION

I, Stephanus Johannes Paulus Retief, declare that the thesis, which I hereby submit for the degree Philosophiae Doctor (Physics) at the University of Pretoria, is my own work and has not previously been submitted by me for a degree at this or any other tertiary institution.

SIGNATURE:  .....

DATE: 2018/07/02



## SUMMARY

---

### **Solving inverse radiometric problems arising from infrared recordings**

by

**Stephanus Johannes Paulus Retief**

Supervisor: Prof. A. Kijko, Director: University of Pretoria Natural Hazard Centre  
Department: Physics  
University: University of Pretoria  
Degree: Philosophiae Doctor (Physics)  
Keywords: Infrared radiometry, infrared modelling, inverse problems, aircraft plume, radiance, intensity, irradiance

The work presented in this thesis arose from the requirement in the military environment to obtain infrared radiation source/signature values of target objects usually of interest to infrared missiles under development. *In situ* measurements made of such objects are typically over a range of 100–3000 m and are influenced by the environment and by the instrument itself; the need therefore exists for measurement methods and data reduction techniques that incorporate corrections of these unwanted influences on the observed radiation.

In this thesis, a measurement equation describing the infrared measurement of solid and gaseous type objects and the influence of the environment and the measuring instrument itself on these measurements is formulated. The measurement equation then forms the starting point of the formulation of a data reduction equation, which represents an inverse radiometric problem to be solved in order to obtain the radiation source values of the object being measured.

An aircraft engine plume, for which a radiometric inverse problem is formulated and solved, is the target object of main interest in this work. *In situ* recordings of a turbine jet engine aircraft were

used, but it is also shown that recordings of a micro turbine engine can be used in concept studies of plume emission. An inversion technique is presented for obtaining the three-dimensional inner radiance structure of a plume after the plume source values have been obtained from measurements. The inversion technique makes use of a discretized version of the formal solution to the equation of radiative transfer, which leads to a matrix equation from which the radiances of the volume elements inside the plume are obtained. The plume emission model based on this inner radiance structure is able to predict the observed plume emission at any arbitrary position outside the plume. The intensity predictions of the plume model are verified at the aspect angles for which measurements are available.

It is also shown that under controlled laboratory conditions, the influence of the instrument on its own measurements by means of its spectral response can be resolved. The specific measurement set-up, involving only the instrument and a blackbody radiator, is described and the results are used as input to a novel inversion technique. The measurement equation for this instance is a Fredholm Integral Equation of the First Kind (IFK), which is manipulated in such a way that the resulting data reduction equation can be used to obtain the instrument spectral response. The IFK is, however, extremely ill-conditioned and the regularization method of Tikhonov is used in order to obtain a stable answer.

The significance of the measurement methods and data reduction techniques presented lies in the improved capability of obtaining accurate radiation source parameters of objects of interest – especially for gaseous type objects such as an aircraft plume, for which the inner radiance structure can also be obtained. With improved source parameter values, the accuracy in the modelling of these objects also improves, leading to the resultant improvement of any electro-optical product being manufactured for the detection, identification and tracking of such objects whenever simulations form part of the product development.

## TABLE OF CONTENTS

<b>CHAPTER 1 INTRODUCTION .....</b>	<b>1</b>
1.1 TOPIC.....	1
1.2 BACKGROUND AND MOTIVATION .....	1
1.3 OBJECTIVES.....	2
1.4 APPROACH.....	3
1.5 CONTRIBUTIONS AND THESIS OUTLINE.....	4
 <b>CHAPTER 2 INFRARED RADIOMETRY .....</b>	 <b>6</b>
2.1 IMPORTANT CONCEPTS AND BACKGROUND .....	6
2.2 MEASURING INSTRUMENTS USED .....	9
2.3 RADIOMETRY FROM RECORDED IMAGES.....	11
 <b>CHAPTER 3 INFRARED RECORDINGS OF AN AIRCRAFT PLUME AT DIFFERENT                     INFRARED WAVELENGTHS .....</b>	 <b>17</b>
3.1 INTRODUCTION .....	17
3.2 PUBLICATION – INFRARED RECORDINGS FOR CHARACTERIZING AN AIRCRAFT PLUME .....	17
 <b>CHAPTER 4 MID-WAVE INFRARED CHARACTERIZATION OF AN AIRCRAFT                     PLUME.....</b>	 <b>34</b>
4.1 INTRODUCTION .....	34
4.2 PUBLICATION – MID-WAVE INFRARED CHARACTERIZATION OF AN AIRCRAFT PLUME .....	36
4.3 PUBLICATION – MEASUREMENTS OF A MICRO GAS TURBINE PLUME AND DATA REDUCTION FOR THE PURPOSE OF INFRARED SIGNATURE MODELING 44	

<b>CHAPTER 5 OBTAINING THE AIRCRAFT PLUME INNER STRUCTURE .....</b>	<b>56</b>
5.1 INTRODUCTION .....	56
5.2 PUBLICATION – AIRCRAFT PLUME INFRARED RADIANCE INVERSION AND SUBSEQUENT SIMULATION MODEL .....	58
<b>CHAPTER 6 OBTAINING THE MEASURING INSTRUMENT’S SPECTRAL         RESPONSE.....</b>	<b>74</b>
6.1 INTRODUCTION .....	74
6.2 PUBLICATION – A TECHNIQUE FOR RESOLVING THE SPECTRAL RESPONSE OF A WIDE-BAND INFRARED MEASURING INSTRUMENT FROM MEASUREMENTS WITHOUT THE NEED FOR A SPECTRALLY TUNEABLE RADIATION SOURCE .....	75
<b>CHAPTER 7 CONCLUSION.....</b>	<b>93</b>
<b>REFERENCES.....</b>	<b>95</b>

## LIST OF FIGURES

Figure 2-1 Radiative transfer between a source ( <i>s</i> ) and observer ( <i>o</i> ) in a lossless optical medium...	9
Figure 2-2 Clockwise from top left: Cedip Jade III MWIR camera, FLIR SC2500 SWIR camera, Telops TEL-1000-VLW camera, Bomem MR200 spectroradiometer.....	11
Figure 2-3 Throughput for optical system with source image that fills the detector focal plane array (FPA).....	12
Figure 2-4 The GUI of the data reduction program showing a fighter aircraft in flight. ....	14
Figure 2-5 A high level diagram of the input information required by the data reduction program and the associated output that can be created with this information. Input data are indicated with parallelograms and output data with rectangles. ....	15
Figure 4-1 The measurement system used in acquiring MWIR image sequences of an in-flight target aircraft. ....	35
Figure 4-2 Typical recording, shown in false colours, of the target aircraft.....	36
Figure 5-1 The ‘observed’ profile (black curve bottom graph) is used as input to the reconstruction techniques indicated in the figure.....	58

## LIST OF TABLES

Table 2-1 Different radiometric quantities.....	8
Table 2-2 Parameters of the Cedip Jade III camera relevant for the work reported.....	10

## LIST OF ABBREVIATIONS

3D	Three-dimensional
A2D	Analogue to Digital
AA	Aspect Angle
ATP	Acceptance Test Procedure
CVF	Circular Variable Filter
CUI	Camera Under Investigation
DL	Digital Level(s)
EGT	Exhaust Gas Temperature
FADEC	Full Authority Digital Engine Control
FOV	Field of View
FPA	Focal Plane Array
FTIR	Fourier Transform Infrared
GPS	Global Positioning System
GUI	Graphical User Interface
IFK	Fredholm Integral Equation of the First Kind
IFOV	Instantaneous Field of View (i.e. Pixel FOV)
IR	Infrared
IRC	Infrared Camera
LOS	Line of Sight
LWIR	Long-wave Infrared/Very Long-wave Infrared
LS	Least Squares
MWIR	Mid/Medium-wave Infrared
MTV	Magnesium/Teflon/Viton
NDF	Neutral Density Filter
NETD	Noise Equivalent Temperature Difference
NIR	Near Infrared
NUC	Non-uniformity Correction
POI	Point of Interest
RMSE	Root Mean Square Error
ROI	Region of Interest

RMSE	Root Mean Square Error
RPM	Rotations per Minute
SPIE	The International Society for Optical Engineering
SR	Spectroradiometer
SVD	Singular Value Decomposition
SWIR	Short-wave Infrared
UAV	Unmanned Aerial Vehicle
VLWIR	Very Long-wave Infrared



## CHAPTER 1 INTRODUCTION

### 1.1 TOPIC

The measurement of the infrared energy content of electromagnetic fields, i.e. *infrared recordings*, originating from an incoherent radiation source, seldom yields the sought-after source radiant energy parameters. The reason for this is related to the influence of the non-ideal measuring instrument on the observed radiant energy as well as the influence of the environment on the measurement. In order to retrieve the source radiant energy values, the first step is to set up a phenomenological model of the measurement, i.e. a measurement equation, which models the radiant energy value registered by the measuring instrument. This model must be adequate in the sense that all mechanisms influencing the radiant energy measured by the instrument are considered ('forward' modelling of measurement). Once such a mathematical model exists, it can be attempted to *solve* the radiometric parameter(s) used in the modelling of the source radiant energy. Isolation of the radiometric source parameter from the model results in the *inverse radiometric problem* ('reverse' modelling of measurement). If, however, the model parameter is known beforehand, some other parameter in the measurement equation, such as the instrument response, might become the parameter for which a solution is desired. Whatever the sought-after model parameter in the measurement equation is, formulating an *inverse radiometric problem* provides a way of obtaining the value of such a parameter. The topic of this thesis is centred on *solving inverse radiometric problems arising from infrared recordings*.

### 1.2 BACKGROUND AND MOTIVATION

The need for radiation source values of objects of interest in the military environment arises from, amongst others, the requirement of an infrared missile under development to be 'trained' to discriminate between its target and other objects in its observable environment. The infrared signature of the target object, e.g. an offensive aircraft for a surface-to-air or air-to-air missile, would typically have been used to prepare missile seeker head algorithms before an actual engagement of the missile with the target could have taken place successfully. The task of the

infrared measurement and the modelling scientist is to make, whenever possible, *in situ* target infrared measurements during field and flight tests over a typical range of 100–3000 *m*, and then create a physics-based mathematical target model of high fidelity. The physical scale of a typical flight test is an order of magnitude smaller than in the field of remote sensing – allowing more freedom in the planning of the experimental set-up. The continual need exists for improved measurement methods and data reduction techniques to improve the accuracy of the target model. This model then forms the basis of a computer model that can be used in simulations where the missile algorithms are developed. Once the infrared source radiance/signature is known after the radiometric inversion problem has been solved, the target can be simulated under any atmospheric conditions and in any static or dynamic geometrical configuration with respect to the missile.

During the data reduction process, information other than the infrared measurements of the object of interest is required in order to solve the radiometric inversion problem. This supplementary information includes meteorological measurements, modelled atmospheric properties based on the meteorological measurements, geometrical information of the positions of the target and measuring instrument, and information about the measuring instrument itself, such as its spectral response to measured radiation. All this information needs to be obtained and integrated in the process of solving the inverse radiometric problem.

### 1.3 OBJECTIVES

Although the target object focussed on in this work is limited to aircraft, the principles and techniques presented for measurement and data reduction equally apply to other targets or objects of interest. In this respect, an aircraft is ideal in the sense that it covers both solid type objects (aircraft fuselage) and gaseous type objects (engine plume), with gaseous type objects being more challenging than solid type objects.

The objectives of the work presented were to:

1. Formulate measurement equations for both solid phase and gas/plasma phase objects.
2. Formulate and solve the inverse radiometric problem of the mentioned objects in order to determine their infrared source signature, with emphasis on the gaseous type object of an aircraft engine plume.
3. Formulate and solve the inverse radiometric problem of determining the inner radiometric structure of an aircraft plume.
4. Formulate and solve the inverse radiometric problem for resolving the measuring instrument's spectral response.

## 1.4 APPROACH

A purely theoretical approach can be used to model the target's infrared signature by using calculations from fields such as physics, chemistry, aerodynamics and thermodynamics. However, due to target and environmental complexity, measurements must also be made and data reduction (inverse radiometric problem solving) must be done to obtain a calibrated/best fitting theoretical model of the target infrared signature. If this theory-driven model is incomplete in its prediction ability for some possible target and observation positions, it is supplemented by an empirical model.

An example of the construction of a radiometrically hybrid model, as explained above, is found in the altitude dependence of the plume emission of an aircraft. The aircraft plume intensity is typically correlated with the aircraft's fuel consumption, which, in turn, is a function of the amount of oxygen available for the combustion process. The available amount of oxygen is in turn related to the partial pressure of oxygen in the atmosphere, which is altitude dependent. The fuel consumption of the aircraft engine is, however, also influenced by factors such as its aerodynamic design (drag of fuselage and any armament carried by the aircraft), mass, engine type and engine setting as well as its optimization in the mechanical workshop. With all these (inter)dependencies and influences, it makes sense to simply measure the plume intensity as a function of altitude (which have the above described complex but explicative relationship) for a specific aircraft with a specific engine setting and then fit an empirical model to this data. This empirical model is then used together with a sound physics-based model of radiative transfer to determine the radiance distribution inside the three-dimensional plume volume so that the resultant plume emission at the outside of the plume can be calculated.

Measurements of targets are made for as many observer-target configurations as practically and economically possible. These measurements can usually not be done under controlled circumstances in a laboratory, but are made of the *in situ* target with a measuring instrument on a mobile platform following the target. Meteorological measurements, observer and target trajectory measurements, sun position calculations and the logging of parameters such as the infrared measuring instrument's internal temperature, which affects its readings, are made in parallel with the target infrared measurements. Most of the information so obtained is synchronized and integrated with bespoke software developed for this purpose by the present author.

## 1.5 CONTRIBUTIONS AND THESIS OUTLINE

Chapter 2 presents the necessary radiometry concepts and background required to follow the succeeding chapters. The basic definitions of radiometric quantities, as used in this thesis, are given to prevent any possible confusion since the same radiometric terms can have different meanings and units in different fields, for example, astronomy [1]. It is also shown how to obtain radiometric values from infrared image recordings.

Chapter 3 contributes a publication [2], which points out the most suitable infrared measurement bands for an aircraft plume within the commonly used wavelength region of 1–15  $\mu\text{m}$ , in consideration of the atmospheric windows and aircraft plume emission lines. Investigation into these infrared bands is done by expressing some basic theoretical considerations, which are backed by modelling and measurement results using infrared cameras in different infrared bands as well as a spectroradiometer. The usefulness of a cost-effective micro turbine engine for concept plume studies related to full-scale aircraft plumes is also argued and demonstrated by measuring and analysing subbands within the mid-wave infrared (MWIR) band; these measurements can be used for automatic plume identification. If the measurements are done correctly, they can be used for constructing a plume model, which can in turn be used in the testing of algorithms in simulations related to plume recognition under conditions for which no recordings exist. More detail on the measurements and data reduction is supplied in the subsequent chapters.

The two publications presented in Chapter 4 [3,4] detail the MWIR characterization of an aircraft in terms of the necessary measurement set-up, accompanying measurement equation and data reduction procedure for obtaining the source emission values. The prerequisite target information required to enable data reduction of *in situ* aircraft measurements is specified in the publication in Section 4.2; some data reduction results for the measured aircraft plume are also shown. In the second publication, presented in Section 4.3, technical detail of MWIR plume measurements and data reduction for the purpose of infrared signature modelling is added when a micro turbine engine is used, as discussed in Section 3.2.

With the MWIR plume source emission values being obtained as described in Chapter 4, the technique developed in the publication [5] in Chapter 5 is used to solve the source inversion problem of obtaining the inner structure of a gaseous emitter. The plume inner structure, i.e. the volumetric radiance distribution, is necessary in order to construct a plume model capable of simulating the emission of the plume from any arbitrary observation position. The predicted

intensity of the plume is verified by comparing it with the intensities at observation positions of which the measurements were not used during data reduction.

In the publication [6] presented in Chapter 6, the MWIR camera used in the plume recordings becomes the object of interest when the infrared emission from the target object is known beforehand. In contrast to the inversion problems solved in the preceding chapters, the measurement equation is now manipulated in such a way that the resulting data reduction equation is directed towards solving the spectral response of the instrument. The resultant Fredholm Integral Equation of the First Kind (IFK) that must be solved in this instance is as notorious as many other IFKs, which are mostly extremely ill-conditioned and not easily invertible. This inversion issue is resolved by making use of the regularization method of Tikhonov.

The thesis is concluded in Chapter 7 by summarizing the contributions presented and by reflecting on the applicability of the methods used.

## CHAPTER 2 INFRARED RADIOMETRY

### 2.1 IMPORTANT CONCEPTS AND BACKGROUND

Although the word ‘radiometry’ itself means the measurement of radiation [7], and is defined as the measurement of optical radiant energy [8], it also refers more generally to the principles and laws behind the generation, propagation and detection of optical radiation [9]. Radiometry, in its widest definition, actually covers all forms of manipulation, including creation, measurement, calculation, modelling, and simulation of optical flux [10], including the analysis and modelling of measured data. ‘Infrared radiometry’, as studied in this thesis, limits itself to the radiometry of the infrared part of the electromagnetic spectrum.

Table 2-1 summarizes the different radiometric quantities commonly used in the field of infrared radiometry (see e.g. [11–13]). The transfer of radiant power,  $\Phi$ , from a source (target object) to an observer (measuring instrument) can be represented schematically as shown in Figure 2-1. In this figure, the (geometrically invariant) radiance is

$$L = \frac{\Delta\Phi}{\Delta\omega_o \overline{\Delta\mathbf{A}_o} \cdot \hat{\mathbf{r}}_o} = \frac{\Delta\Phi}{\frac{\Delta A_s \cos\theta_s}{r^2} \Delta A_o \cos\theta_o}, \quad (1)$$

where

$$\Delta\omega_o \equiv \frac{\overline{\Delta\mathbf{A}_s} \cdot \hat{\mathbf{r}}_s}{r^2} = \frac{\Delta A_s \cos\theta_s}{r^2} \quad (2)$$

is the solid angle subtended by the source with flat surface area  $\Delta A_s$ . The two surfaces of the source and object are separated by a distance  $r$  in a lossless optical medium, with  $\hat{\mathbf{r}}_s$  being the unit vector directed from the source to the observer, and  $\hat{\mathbf{r}}_o$  the unit vector directed from the flat observer area  $\Delta A_o$  towards the source. The angle between the surface area vector  $\overline{\Delta\mathbf{A}_s}$  and  $\hat{\mathbf{r}}_s$  is  $\theta_s$ ; the angle

between  $\overrightarrow{\Delta A_o}$  and  $\hat{r}_o$  is  $\theta_o$ . It must be noted that sufficient accuracy of Equation (1) and the other equations of radiometric quantities (Table 2-1) to follow require the condition  $r^2 \gg \max(\Delta A_o, \Delta A_1)$ ; i.e. the separation distance between source and receiver must be relatively large in comparison with the surface areas of the source and observer.

Since the measurement instruments used in this work have a potential difference or current output, which is proportional to the radiance of the source being measured, it is desirable to obtain the radiometric quantities in terms of  $L$ . From Equation (1) and the definition of irradiance,  $E$ , it can be seen that the irradiance at the observer surface is obtained from  $L$  by

$$\Delta E_o = \frac{\Delta \Phi}{\Delta A_o} = L \cos \theta_o \Delta \omega_o, \quad (3)$$

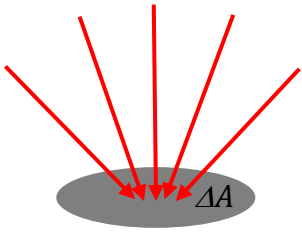
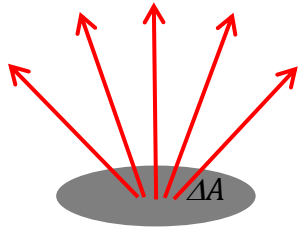
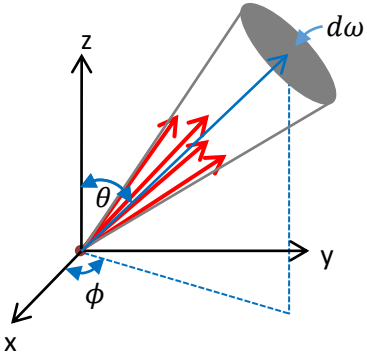
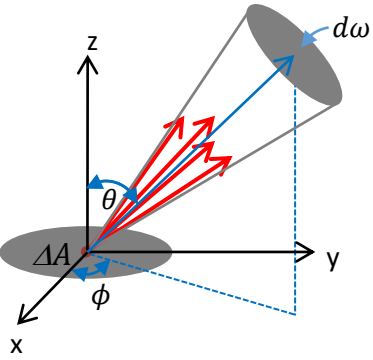
while the exitance at the source surface is obtained by

$$\Delta M_s = \frac{\Delta \Phi}{\Delta A_s} = L \Delta \omega_s \cos \theta_s. \quad (4)$$

The intensity of the source is obtained from  $L$  by

$$\Delta I_s = \frac{\Delta \Phi}{\Delta \omega_s} = \frac{\Delta \Phi}{\frac{A_o \cos \theta_o}{r^2}} = L \Delta A_s \cos \theta_s. \quad (5)$$

Table 2-1 Different radiometric quantities.

Radiometric quantity	Symbol and units	Description	Graphical description	Defining equation
Radiant energy	$Q$ [J]	The total energy contained in a radiation field.	--	--
Radiant power	$\Phi$ [W]	The rate of radiant energy transfer.	--	$\Phi = \frac{dQ}{dt}$
Irradiance	$E$ [W.m <sup>-2</sup> ]	The radiated power per unit area incident on a surface, i.e. it is the power that is received by a surface.		$E \equiv \frac{d\Phi}{dA}$
Exitance	$M$ [W.m <sup>-2</sup> ]	The power per unit area radiated from a surface into the overlying hemisphere, i.e. it is the power that exits a source.		$M \equiv \frac{d\Phi}{dA}$
Intensity	$I$ [W.sr <sup>-1</sup> ]	The radiant power emitted per unit solid angle by a source in a specific direction. The source under consideration is a point source.		$I \equiv \frac{d\Phi}{d\omega}$
Radiance	$L$ [W.m <sup>-2</sup> .sr <sup>-1</sup> ]	The radiant power emitted per unit solid angle in a specific direction per unit projected source area. The source area under consideration is seen as a continuous distribution of point sources from which the cones of radiation originates.		$L \equiv \frac{\partial^2 \Phi}{\partial A \cos \theta \partial \omega}$



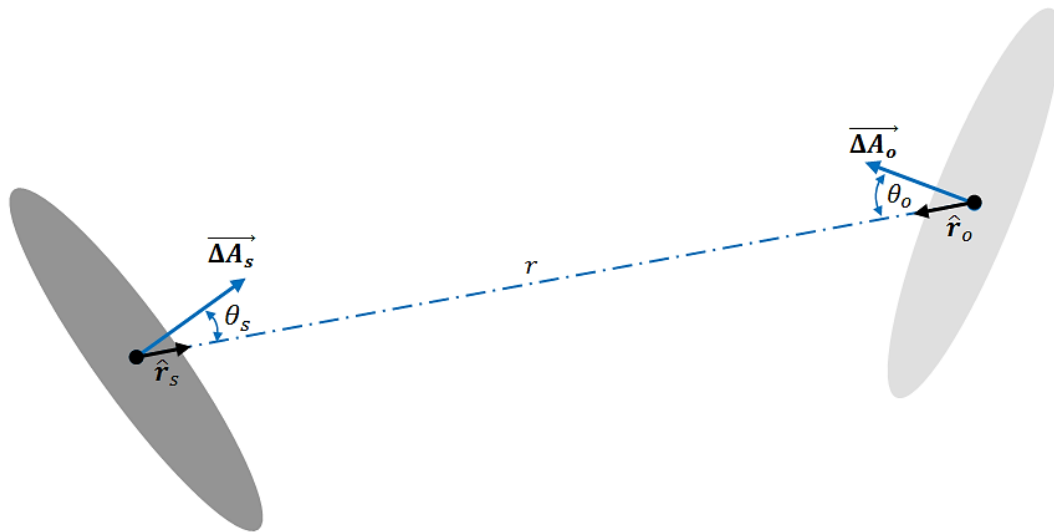


**Figure 2-1 Radiative transfer between a source (*s*) and observer (*o*) in a lossless optical medium. The source area size and direction are given by the area vector  $\overline{\Delta A}_s$  (perpendicular on the area with size  $\Delta A_s$ ) and that of the observer is given by  $\overline{\Delta A}_o$ . The unit direction vector  $\hat{r}_s$  is directed from the source to the observer and differs with an angle of  $\theta_s$  with respect to  $\overline{\Delta A}_s$ ; the vectors and angle at the observer area are similarly defined.**

## 2.2 MEASURING INSTRUMENTS USED

The main measuring instrument used was the Cedip Jade III MWIR camera. Measurements made with this instrument were used in the work reported in Chapter 3 – Chapter 6. This camera was calibrated by measurements of a blackbody at various temperatures (over a short distance of approximately 30 cm) for which the radiance spectra were calculated and used together with the instrument spectral response to determine the measured band radiances. The band radiances were then linked to the recorded digitized voltage output of the camera – see Section 4.3 and Chapter 6 for more detail. Repeated calibration efforts over the last 10 years indicated a high degree of stability in the output of the camera associated with each of the blackbody calibration temperatures, especially since an upgrade to the camera was made by the manufacturer in 2006 (before any of the measurements reported on in this thesis were done). A dependency of the camera output towards its internal housing temperature, however, still exists – a variation in the camera output of almost 5% was observed when the camera housing temperature varied over a very wide range of approximately 23 °C. This dependency is usually taken care of by means of attempting to maintain a constant camera housing temperature during measurements by control of the camera's direct environment, or by extending the calibration to include calibration measurements obtained at different housing temperatures.

Non-uniformity corrections (NUCs) of individual pixels for each integration time were based on measurements of a uniformly textured, high emissivity black plate filling the camera's field of view (FOV). A description of all relevant parameters of this camera and the range of settings used during measurements are given in Table 2-2.

**Table 2-2 Parameters of the Cedip Jade III camera relevant for the work reported.**

Parameter	Description/Value/Setting Used
Model name	Cedip Jade III (2003 model)
Detector	Cooled ( $\sim 74\text{ K}$ ) InSb
NETD (Noise equivalent temperature difference)	$< 25\text{ mK}$
Camera internal housing stabilising temperature	$\pm 39.5\text{ }^\circ\text{C}$ at an ambient temperature of $22\text{ }^\circ\text{C}$
Waveband	MWIR, $3.6\text{--}5.2\text{ }\mu\text{m}$
Resolution, pixel pitch	$320 \times 240$ pixels, $30\text{ }\mu\text{m}$
Integration times	Multi – $30\text{ }\mu\text{s}$ , $240\text{ }\mu\text{s}$ , $1000\text{ }\mu\text{s}$ and $2800\text{ }\mu\text{s}$
Frame rate	$20\text{--}100\text{ Hz}$
Lens focal distance and FOV	$50\text{ mm}$ : $10.97^\circ$ ( <i>horz.</i> ) $\times$ $8.24^\circ$ ( <i>vert.</i> ) $200\text{ mm}$ : $2.75^\circ$ ( <i>horz.</i> ) $\times$ $2.06^\circ$ ( <i>vert.</i> )
Instantaneous FOV (IFOV), i.e. pixel FOV calculated from pixel pitch/focal distance	$50\text{ mm}$ : $600\text{ }\mu\text{rad}$ $200\text{ mm}$ : $150\text{ }\mu\text{rad}$
f/#	2
Analogue to digital (A2D)	14 bit

Use was also made of a short-wave infrared (SWIR) camera (sensitive in  $1.1\text{--}1.5\text{ }\mu\text{m}$ ) and a very long-wave infrared (VLWIR or LWIR) camera (sensitive in  $7.7\text{--}11.8\text{ }\mu\text{m}$ , with subbands within this range) in a qualitative manner for the work reported in Chapter 3. These cameras were equipped with an uncooled InGaAs<sup>1</sup> detector and a cooled HgCdTe<sup>2</sup> detector respectively. Spectral information was obtained with a Bomem MR200 Fourier Transform Infrared (FTIR) spectroradiometer. Measurements made with this instrument were used in the work reported in Chapter 3 – Chapter 5. The spectrometer was calibrated either before or after use by the

<sup>1</sup> Indium gallium arsenide

<sup>2</sup> Mercury cadmium telluride

measurement of a blackbody at various temperatures. Photos of the various instruments used are shown in Figure 2-2.



Figure 2-2 Clockwise from top left: Cedip Jade III MWIR camera, FLIR SC2500 SWIR camera, Telops TEL-1000-VLW camera, Bomem MR200 spectroradiometer.

### 2.3 RADIOMETRY FROM RECORDED IMAGES

Each of the infrared instruments records an image with a pixel resolution determined by its detector. A spectroradiometer recording can be considered as a special case of an image having a  $1 \times 1$  pixel resolution, but with a wavelength radiation spectrum associated with this pixel. For a camera, the radiation recorded by each of its pixels is the summation of the spectral radiation over all wavelengths in the band in which the instrument operates, i.e. for a calibrated, ideal camera with a flat spectral response the measured pixel wide-band radiance is

$$L_{\lambda_1-\lambda_2}(\text{pixel}) = \int_{\lambda_1}^{\lambda_2} L(\lambda) d\lambda, \quad (6)$$

where  $L(\lambda) \equiv \frac{dL}{d\lambda}$  is the spectral radiance recorded by the pixel (detector), and  $\lambda_1$  and  $\lambda_2$  are the wide-band wavelength boundaries ( $\lambda_1 < \lambda_2$ ). The wide-band radiance is generally just referred to as  $L$  without subscript, with the context indicating the specifics of the band (SWIR, MWIR, LWIR).

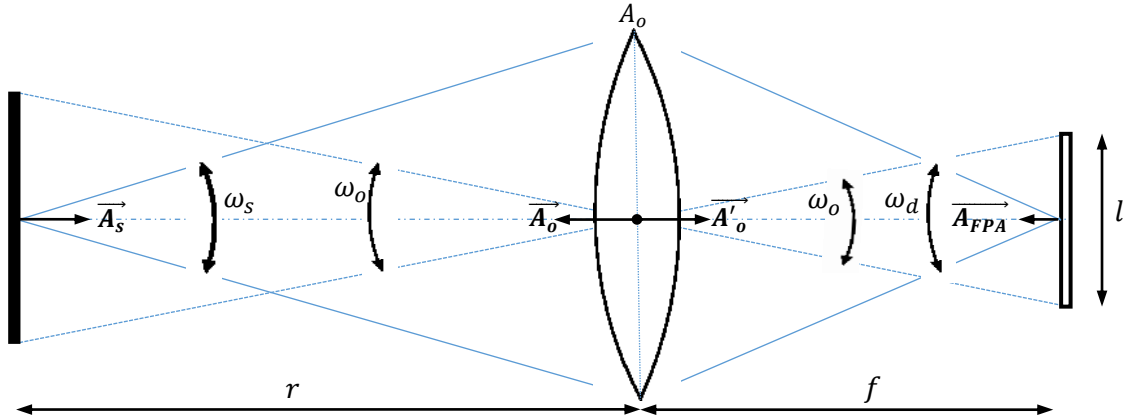


**Figure 2-3 Throughput for optical system with source image that fills the detector focal plane array (FPA). The same symbols are used as in Figure 2-1, but with area  $A_o$  now representing entrance pupil (lens) area of a camera; also shown is the FPA area vector  $\vec{A}_{FPA}$  and the solid angle  $\omega_d$  at the FPA subtended by the area  $A_o$ . The focal length of the camera is given by  $f$ . Note that  $\vec{A}_o$  and  $\vec{A}'_o$  are vectors of the same size but in opposite directions.**

Figure 2-3 shows a schematic diagram of an optical system, i.e. a camera in this work, directed directly towards a source/target object with the object filling the FOV of the camera with the resultant image also filling the FPA of detectors/pixels. The left-hand side of the figure showing the source area  $A_s$  and observer area  $A_o$  is similar to Figure 2-1, but now with  $\theta_s = 0$  and  $\theta_o = 0$ . The area of the FPA is represented by vector  $\vec{A}_{FPA}$ , which is also in line with the optical axis of the camera. The throughput of such an optical system, [11], is given by

$$A_s \omega_s = A_s \left( \frac{A_o}{r^2} \right) = \left( \frac{A_s}{r^2} \right) A_o = \left( \frac{A_{FPA}}{f^2} \right) A'_o = \left( \frac{A_{FPA}}{f^2} \right) A_o, \quad (7)$$

i.e.

$$\frac{A_s}{r^2} = \frac{A_{FPA}}{f^2}. \quad (8)$$

Radiance is invariant and, therefore, the target radiance at the detector plane is the same as the radiance of the target object at the source (given that there are no transmission losses), so that

$$L_{target} = \frac{\phi}{\left( \frac{A_s}{r^2} \right) A_o} = \frac{\phi}{\left( \frac{A_{FPA}}{f^2} \right) A_o}, \quad (9)$$

where  $\phi$  is the flux from the target object incident on the camera lens. Since the FPA is composed of a two-dimensional array of  $m \times n$  square detectors, each with an area of  $A_d$ , Equation (9) can be rewritten as

$$\begin{aligned}
 L_{target} &= \frac{\sum_{i=1}^m \sum_{j=1}^n \Delta\phi_{i,j}}{\left(\frac{NA_d}{f^2}\right) A_o} \\
 &= \frac{1}{N} \sum_{i=1}^m \sum_{j=1}^n L_{ij} \\
 &= \bar{L}_{pixel},
 \end{aligned} \tag{10}$$

where  $\Delta\phi_{ij}$  is the flux on the pixel in row  $i$  and column  $j$ , i.e. at pixel  $(i,j)$ , and  $L_{ij}$  is the corresponding radiance. From Equation (10) it can be seen that the radiance of an extended source, with image filling the FPA, is equal to the average pixel radiance  $\bar{L}_{pixel}$ . If the target image does not fully cover the FPA, Equation (10) can be written as

$$L_{target} = \frac{1}{N_{tpixels}} \sum_{tpixels} L_{ij} = \bar{L}_{tpixel}, \tag{11}$$

where the summation takes place over all pixels filled by the target, i.e. over all target pixels ( $tpixels$ ), and with  $N_{tpixels}$  being the number of target pixels and  $\bar{L}_{tpixel}$  being the average target pixel radiance.

The intensity of the target object in such an image is obtained from Equations (5) and (11) as

$$\begin{aligned}
 I_{target} &= \bar{L}_{tpixel} A_s \\
 &= \bar{L}_{tpixel} \sum_{tpixels} \Delta A_{sij} \\
 &= \bar{L}_{tpixel} \sum_{tpixels} (r\theta_{ifov})^2 \\
 &= \bar{L}_{tpixel} N_{tpixels} r^2 \theta_{ifov}^2,
 \end{aligned} \tag{12}$$

where  $\theta_{ifov}$  is the instantaneous field of view (IFOV), i.e. the FOV of a single detector/pixel.

The observed irradiance is derived as

$$\begin{aligned}
 E_o &= \bar{L}_{tpixel} \omega_o \\
 &= \bar{L}_{tpixel} \sum_{tpixels} \Delta\omega_{oij} \\
 &= \bar{L}_{tpixel} \sum_{tpixels} \frac{\Delta A_{sij}}{r^2} \\
 &= \bar{L}_{tpixel} N_{tpixels} \theta_{ifov}^2.
 \end{aligned}
 \tag{13}$$

From Equations (12) and (13), the well-known relationship between source intensity and observed irradiance [11] can be deduced:

$$E_o = \frac{I_{target}}{r^2}.
 \tag{14}$$

Extensive use of an infrared data reduction computer program, as developed by the present author, was made in obtaining the radiometric quantities of target radiance and intensity from measurements by means of the methods reported in this thesis. This program, of which the graphical user interface (GUI) is shown in Figure 2-4, was written using the Matlab<sup>®</sup> software package.

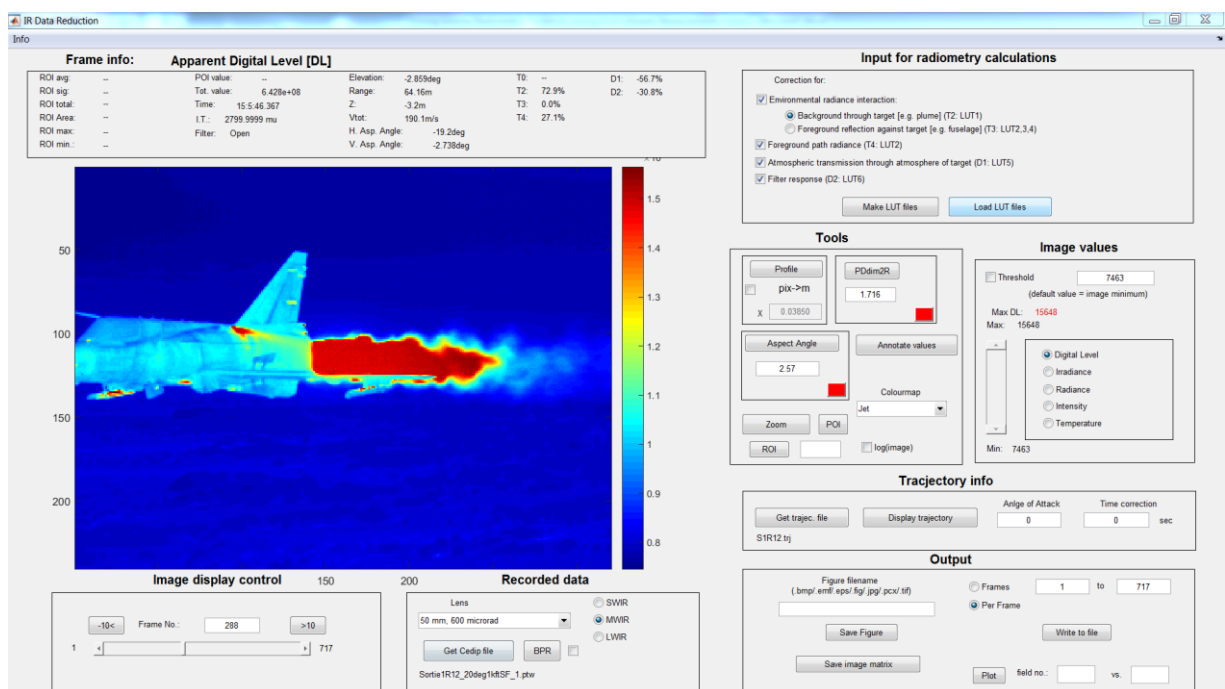
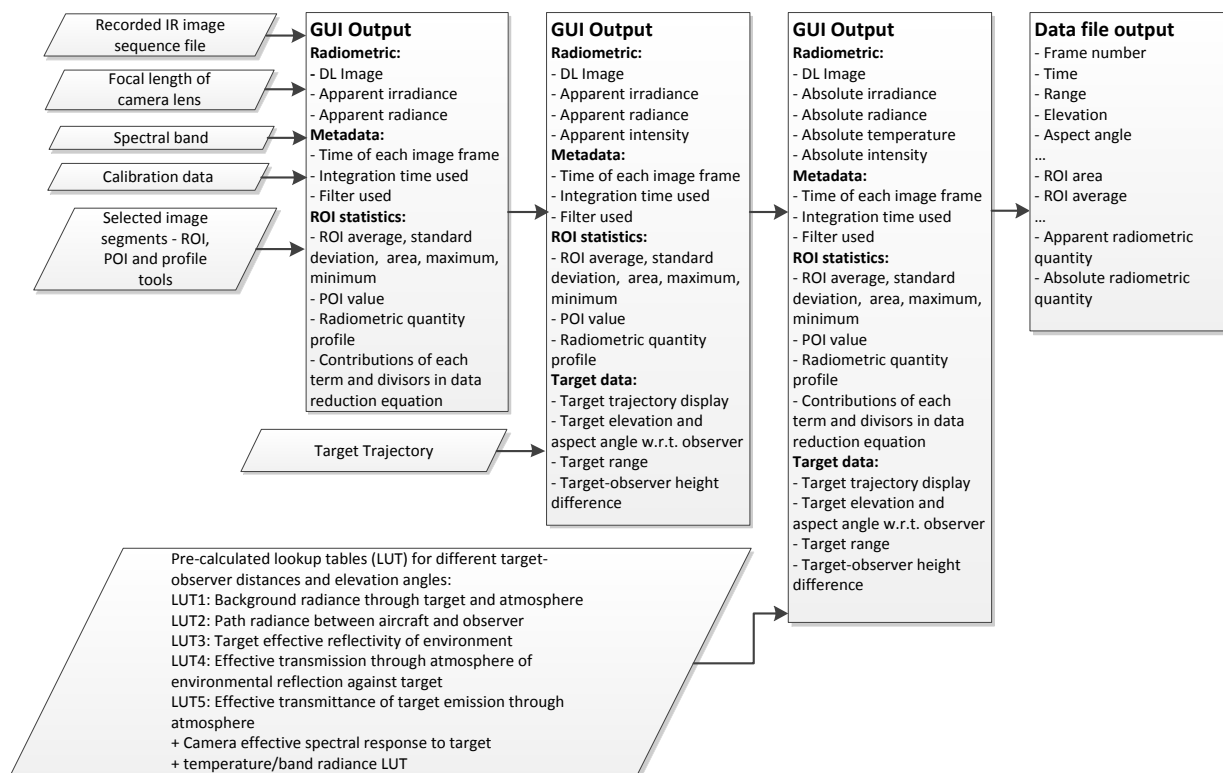


Figure 2-4 The GUI of the data reduction program showing a fighter aircraft in flight.

The program integrates and synchronizes the recorded infrared images (for which the camera set-up must be specified) with the relative observer-target trajectory as well as atmospheric properties modelled on meteorological measurements made at the time of the infrared recordings. Various types of output, e.g. plume intensity, fuselage intensity, plume radiance profiles or fuselage temperature, can be obtained and saved to a data file. A schematic diagram of the required input data and the generated output data for this program is shown in Figure 2-5.



**Figure 2-5 A high level diagram of the input information required by the data reduction program and the associated output that can be created with this information. Input data are indicated with parallelograms and output data with rectangles.**

Uncertainties in the mentioned outputs obtained from the data reduction can arise due to, amongst others, the following reasons:

- Uncertainty in the positions of the observer and target and the resulting observer-target distance during the measurements. An estimate for these uncertainties usually exist and depends on the equipment used to obtain the trajectories.
- Calibration inaccuracies and dependencies on camera internal housing temperature. These uncertainties can be handled as discussed in Section 2.2.

- Uncertainty in die instrument response spectrum of the camera used. It is not always possible to obtain an accurate instrument spectral response spectrum – this is an important topic to which Chapter 6 is devoted.
- Uncertainties in the model used to predict the atmospheric transmittance and path radiance – the model typically requires meteorological altitude profiles obtained from a weather balloon at the time of the recording; these balloons are usually only launched about an hour before (or after) measurements (were made). The ideal of direct, spectral measurements of the path radiance and transmittance between the observer and target is seldom practically possible, and it is therefore problematic to obtain an estimate of the uncertainties arising from the modelled parameter values.
- The unavailability of the target spectral radiance values if only recordings made with a wide-band camera are available. The spectral radiance values are required, together with the spectral transmittance values, in order to obtain the target source value. If these spectral values are not available, assumptions are usually made regarding the target radiance spectrum – an estimate of the uncertainties arising from these assumptions is problematic to obtain.
- The influence of radiometric sources not accounted for during data reduction, such as reflections by the target of its environment. In principle, a complete three-dimensional radiometric model of the target's environment is required in order to obtain an estimate of the contribution of the environment towards the measured radiance value.

An indication of the effect of uncertainties in the atmospheric transmittance and the target spectral emission (in terms of spectral emissivity and target temperature) alone can be found in [14] – it is stated that the predicted IR intensity is indeed a range rather than a specific value. In the presence of the above mentioned uncertainties, many for which the magnitude is unknown, it is not a trivial task to determine the propagation of the uncertainties during data reduction and such an explicit analysis does not form part of this thesis. It is, however, always kept in mind that the quality of the absolute radiometric quantities obtained from data reduction is subject to the quality of the input information. The reasonableness of the obtained radiometric values can, however, be established if measurements are available for verification of the IR model of the target object which were constructed by means of a different set of measurements, as was the case presented in Chapter 5.



## **CHAPTER 3                    INFRARED RECORDINGS OF AN AIRCRAFT    PLUME AT DIFFERENT INFRARED WAVELENGTHS**

### **3.1    INTRODUCTION**

Observations by electro-optical instruments are made at different wavelengths/wavelength bands for different applications. The publication [2] in Section 3.2 investigates the accessible infrared wavelength bands and their applicability in aircraft plume observations by means of measurement illustrations and a discussion of the basic emission and transmission agents at play – the relevant molecular species in the atmosphere and in a gas turbine engine plume are identified and their relevant properties discussed. This discussion guides the investigation towards the suitability of the MWIR band and its subbands for concept studies related to automatic plume detection and identification based on physical emission attributes of the plume that can be utilized in addition to existing image processing techniques in current use. The suitability of the MWIR band for plume detection forms the rationale behind some existing missile seeker heads for operating in this wavelength region (although they might not be limited to this band alone), and is also the reason for the detailed MWIR characterization of an aircraft plume, which follows in the publications presented in Chapter 4.

### **3.2    PUBLICATION – INFRARED RECORDINGS FOR CHARACTERIZING AN    AIRCRAFT PLUME**

Since the measurements made for this publication involved the simultaneous use of all instruments mentioned in Section 2.2, the present author was assisted by two of his workplace colleagues with the SWIR camera and spectroradiometer recordings, and the associated retrieval of the measured spectra from the spectroradiometer; for this reason, they are stated as co-authors of the publication. The remainder of the work, i.e. measurements with the MWIR and LWIR cameras, the publication itself and all calculations contained therein, was the sole work of the present author. The publication was reviewed by the conference chair/committee members of the conference where it was presented. Relevance of the publication to other researchers can be deduced from three references made to the publication at this stage:

- The peer-reviewed journal article [15] refers to the discussion in the publication of the infrared signal transmission through the atmosphere.
- The peer-reviewed journal article [16] refers to the investigation in the publication regarding the usefulness and cost effectiveness of using a micro turbine engine for conceptual plume studies related to full-scale aircraft plumes.
- The peer-reviewed journal article [17] refers to the findings in the publication of the MWIR band being the most versatile for plume observations and the statement of the influence of the fuel consumption and observation configuration on the detected emission.

The article was published in the Proceedings of the Third SPIE (The International Society for Optical Engineering) Sensors, MEMS and Electro-Optical Systems conference held in Skukuza, Kruger National Park, South Africa [2].

## Infrared recordings for characterizing an aircraft plume

S. J. P. Retief\*, M. M. Dreyer, C. Brink

Simulation and Design Department, Denel Dynamics, P.O. Box 7412, Centurion, 0046, South Africa

### ABSTRACT

Some key electro-optical measurements required to characterize an aircraft plume for automated recognition are shown, as well as some aspects of the processing and use of these measurements.

Plume measurements with Short Wavelength Infrared ( $1.1 - 2.5 \mu\text{m}$ ), Mid-Wavelength Infrared ( $2.5 - 7 \mu\text{m}$ ) and Long Wavelength Infrared ( $7 - 15 \mu\text{m}$ ) cameras are presented, as well as spectroradiometer measurements covering the whole Mid-Wavelength, Long Wavelength and upper part of the Short Wavelength Infrared bands. The two limiting factors for the detection of the plume, i.e. the atmospheric transmission bands and the plume emission bands, are discussed, and it is shown how a micro turbine engine can assist in aircraft plume studies. One such a study, regarding the differentiation between an aircraft plume and a blackbody emitter using subbands in the Mid-Wavelength Infrared, is presented.

The factors influencing aircraft plume emission are discussed, and the measurements required to characterize an aircraft plume for the purpose of constructing a mathematical plume model are indicated. Since the required measurements are prescribed by the plume model requirements, a brief overview of the plume model, that can be used to simulate the results of the plume's emission under different conditions and observation configurations, is given. Such a model can be used to test the robustness of algorithms, like the mentioned subband method, for identifying aircraft plumes. Such a model furthermore enables the simulation of measurements that would be obtained by an electro-optical system, like an infrared seekerhead of a missile, of a plume for the purpose of algorithm training under various simulated environmental conditions.

**Keywords:** Short Wave, Mid-Wave, Mid-Wave subband, Long Wave, Infrared, Aircraft plume, Micro turbine, plume emission

### 1. INTRODUCTION

In this article the measurements of a turbine engine plume in different infrared (IR) bands within  $1 - 15 \mu\text{m}$  are shown, and the most useable band for plume detection is identified. Due to similarities in the combustion process of a full scale aircraft plume and a micro turbine engine plume, measurements made of a micro turbine engine plume were used to assist in this study. A simple method, using subbands in the Mid-Wave Infrared (MWIR) to automatically identify an aircraft plume amongst other IR emitting objects, is also presented. The exact form and amplitude of radiance spectra in these subbands are, however, dependent on various factors influencing the emission from the plume; these factors are briefly discussed and illustrated with some results from measurements reported earlier on<sup>1</sup>. To test the robustness of any plume identification technique, such as the presented subband method, the technique must still yield the correct results when any of these factors come into play. It is, however, impossible, unpractical or too costly to obtain measurements as a function of all the factors influencing the plume emission and a more feasible method of creating a mathematical model has to be employed. Such a model, however, needs as input certain measurements to characterize a plume in order to extract the source parameters required for usage in the plume model. This model can then be used to produce 'new' measurements by way of simulation.

The procedure to develop a mathematical aircraft plume model will not be fully discussed, since this was already reported on in [2], but an overview will be given for the sake of completeness. The intent is, therefore, to show the required recordings needed for constructing a radiometrically correct IR plume model, as prescribed by the model, that can be used in IR simulations to test algorithms for aircraft plume detection. This plume model is also useful in the training of algorithms (of e.g. missiles) in the tracking of aircraft, as well as to predict the intensity values of the aircraft plume under various conditions.

\*paul.retief@deneldynamics.co.za; phone +27 12 671-1817; www.deneldynamics.co.za



## 2. IR BANDS OF IMPORTANCE FOR PLUME OBSERVATIONS

The infrared wavelength bands, in which an aircraft plume is observable, are determined by two factors: the atmospheric transmission of the IR energy emanating from the plume and the emitting molecular species in the plume. Although other factors, like the IR path radiance of the atmosphere and the sensitivity of the instrument used for the observations also have an influence on the plume observability, the aforementioned two factors determine whether the plume will in principle be detectable or not.

Figure 1 shows the modelled atmospheric transmittance over a horizontal distance of 1 km for an altitude of ~1500 m above sea level for a Mid-Latitude Summer atmosphere. The main gases influencing the transmission through the atmosphere in the 1 – 15  $\mu\text{m}$  wavelength region is water ( $\text{H}_2\text{O}$ ) and carbon dioxide ( $\text{CO}_2$ ) as can be seen when comparing the bottom graph in Figure 1 showing the transmission of these two gases, with the top graph showing the total transmission. It is the band absorption areas within these two gases that defines the customary division of this wavelength range into the Short Wavelength IR (SWIR) region of 1.1 – 2.5  $\mu\text{m}$ , the Mid-Wavelength IR (MWIR) region of 2.5 – 7  $\mu\text{m}$  and the Long Wave IR (LWIR) region of 7 – 15  $\mu\text{m}$  (see [3]; the exact values of these definitions differ in the literature throughout the IR field). The transmittance within these bands, however, deteriorates as the length of the atmospheric path increases, resulting in a weaker IR signal from the object of interest.

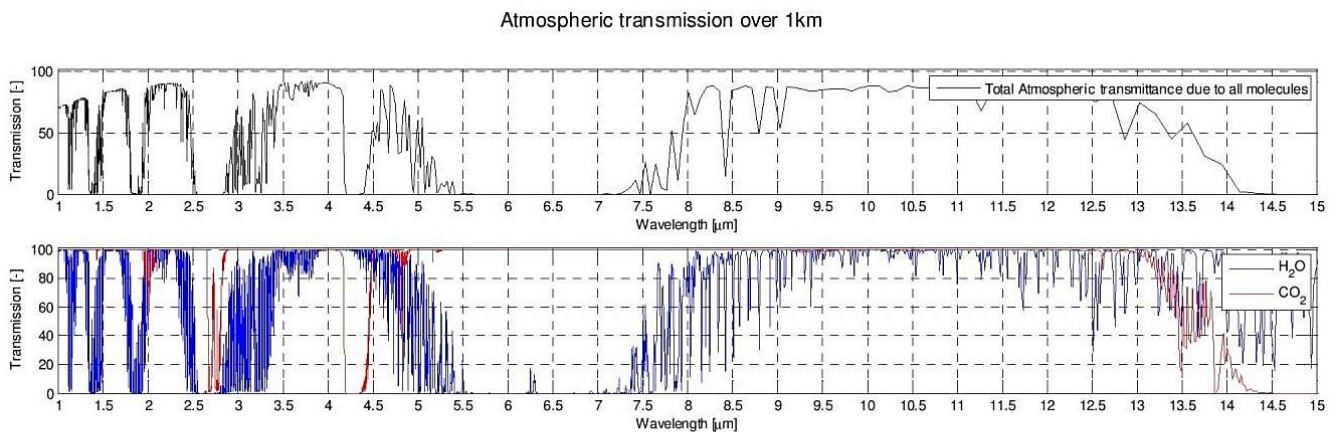
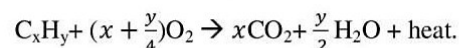
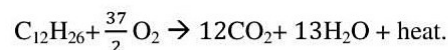


Figure 1. Modelled atmospheric transmission over 1 km for a mid-latitude summer atmosphere as calculated using the computer program PcModWin 4.0 (Ver. 1.01, June 2001, Ontar Corporation©). The top graph shows a low spectral resolution curve of the total transmittance through the atmosphere; all atmospheric molecules, like  $\text{CO}_2$ ,  $\text{H}_2\text{O}$ ,  $\text{O}_3$ ,  $\text{N}_2$ ,  $\text{NO}$ ,  $\text{NO}_2$ , etc., are considered in these calculations. The higher spectral resolution bottom graph, showing only the influence of the  $\text{CO}_2$  and  $\text{H}_2\text{O}$  molecules on the transmittance, indicates that these molecules play a major role in defining the atmospheric windows over the wavelength range of 1 – 15  $\mu\text{m}$ .

The fuels used in gas turbine engines are usually hydrocarbons (e.g. methane, butane, propane, diesel, paraffin, jet fuel, etc.) having the general form<sup>4</sup>  $\text{C}_x\text{H}_y$ . The oxidizer used in gas turbines is atmospheric air, and the complete combustion of the hydrocarbon fuel with oxygen can be described by the general reaction



Jet fuel (kerosene) is a mixture of different hydrocarbons, amongst which dodecane,  $\text{C}_{12}\text{H}_{26}$ , is prominent. The stoichiometric combustion reaction for this hydrocarbon in oxygen is



The products of this reaction might dissociate into C, CO, OH and O, and the presence of nitrogen in the atmospheric air (gas turbine oxidizer) on the reactant side of the chemical equation will also result in  $\text{N}_2$  as being one of the products of the reaction; any other fuel additives might also contribute to the emission from the plume, as well as soot in the case of



incomplete combustion. However, the main IR radiation of energy during the combustion process is considered to be at the resonance frequencies of  $\text{CO}_2$  and  $\text{H}_2\text{O}$ .

Due to the finite length of the emitted wavetrains resulting from the molecular energy level transitions, there is a spread over wavelength at the emission lines present in the emitted IR radiation, known as their natural linewidths<sup>5</sup>. This wavelength spectra of emission lines of the plume gases broadens further due to the random thermal motion of the molecules (Doppler broadening) and collisions of the radiating molecules (Lorentz broadening). If the density of the molecules increases, the molecules act upon each other in such a manner that a slight shift in their respective energy levels occurs. The end result is a spreading out of the original energy levels, thereby blurring them in continuous bands. The emission spectrum from a very dense gas/plume at thermal equilibrium is expected to approach that of a Planck radiator, or blackbody<sup>6</sup>.

Taking the chemistry of the outlined combustion process into consideration, a study of the IR emission from a turbine powered aircraft is not necessarily limited to a full scale aircraft – much can be learned from a micro turbine engine<sup>7</sup>, which functions on the same underlying principles as that of a full scale turbine engine and uses the same fuel. In most of the measurements described in this article, use was made of a Kingtech K80 micro turbine engine, shown in Figure 2, running on Jet A-1 fuel. This engine was set up to run at 135 000 RPM during the measurements (93% of max RPM at 145 000 RPM), during which the Exhaust Gas Temperature (EGT) was in the region of 525 – 540°C. Recordings in different IR bands of this engine plume over a distance of 5 m, as well as full scale aircraft plumes, are elaborated on in Sections 2.1 – 2.5. Unfortunately, no afterburner settings are usually available for micro turbine engines, thereby not making it possible to study afterburner plumes using a micro turbine.



Figure 2. Micro turbine set-up used for IR measurements. The turbine used a propane/butane gas mixture only for startup, after which the fuel supply was switched to Jet A-1 fuel.

## 2.1 Spectroradiometer recordings

The micro turbine plume spectrum, as recorded by the MCT detector of a Fourier Transform IR (FTIR) spectroradiometer (Bomem MR200) over the mentioned distance of 5 m, is shown in Figure 3. The instrument's field of view (FOV) covered the whole area of the plume. It is easily established that the emission band centered at a wavelength of  $\lambda = 4.3 \mu\text{m}$  is that of  $\text{CO}_2$ , considering the molecular species present in the plume ( $\text{CO}_2$  and  $\text{H}_2\text{O}$ ) and the transition lines of  $\text{CO}_2$  (as can be deduced from Figure 1). The bottom graph in Figure 3 shows a blue spike (shorter wavelength) and red spike<sup>8</sup> (longer wavelength) of the plume emission. Note that the data contains a fair amount of noise towards the short wavelength cut-off of the detector and therefore all measurements for  $\lambda < 2 \mu\text{m}$  were discarded; also, all negative radiance values resulting from the noise were clipped to a value of zero.

As a reference, a commercial blackbody radiator, having the same temperature than the nominal plume temperature of 540°C (measured in the exit nozzle of the turbine), was also measured over a distance of 5 m. In the top graph of Figure 3 the transmission effect of the atmosphere on the blackbody can be seen when comparing its measured radiance with the theoretical radiance of the blackbody. The spectral transmission through this thickness of atmosphere  $\tau_{5m}(\lambda)$ , was easily calculated by dividing the measured radiance of the blackbody by its theoretical radiance. In the noisier part of the

measured spectrum, i.e.  $\lambda \leq 3 \mu\text{m}$ , the transmission values at certain wavelengths were erroneously larger than one. Such values were clipped to a maximum value of one.

The top graph also clearly shows the strong  $\text{CO}_2$  absorption of the atmosphere at  $4.3 \mu\text{m}$ , the same wavelength that forms the center of the plume emission band. It must, however, be noted that the absorption band of the atmosphere is narrower than the emission band of the plume. The gap between the two spikes can therefore be explained by the narrow band  $\text{CO}_2$  absorption in the atmosphere (and cooler outer layers of the plume<sup>9</sup>) of the wider  $\text{CO}_2$  emission band of the plume. As a result, the plume emission is split into two parts, referred to as the ‘blue’ spike at the short wavelength side of the center wavelength, and the ‘red’ spike at the long wavelength side of the center wavelength. Although some emission at the center wavelength is still observed in the plume measurement over 5 m, this value quickly drops towards zero as the atmospheric path length increases, as illustrated by an additional measurement over 10 m shown in the bottom graph of Figure 3. The  $\text{CO}_2$  plume emission usually reaching a distant observer is only the red and blue spike flanks of the Doppler and Lorentz broadened emission band, broadened beyond the width of the  $\text{CO}_2$  absorption band of the atmosphere and cooler outer layers of the plume. It is this broadening, caused by the relatively high temperature and high density of the  $\text{CO}_2$  emitting molecules in the plume, which makes distant observation of the plume possible.

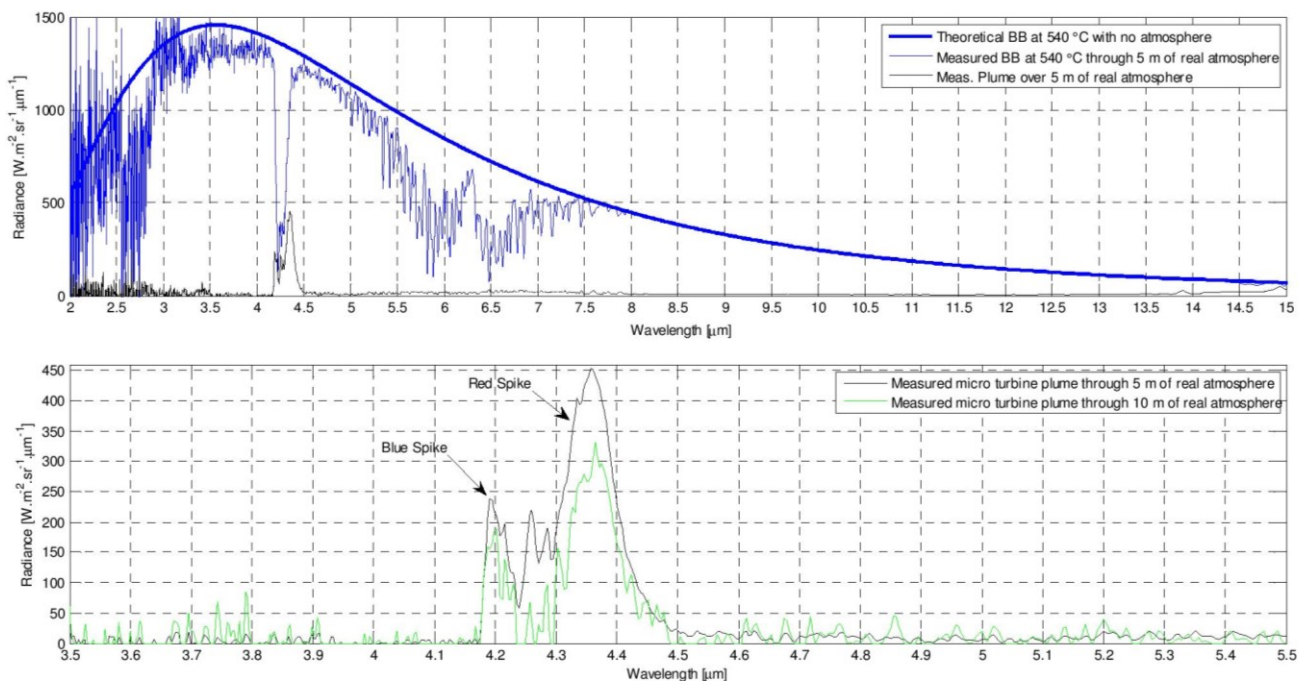


Figure 3. Measured micro turbine and blackbody spectra. The top graph shows the turbine spectrum together with that of a blackbody of similar temperature than the plume. The theoretical Planck curve is also shown. The bottom graph zooms in on the  $3.5 - 5.5 \mu\text{m}$  region, where the plume is a strong emitter, to show the plume measurements over the two distances of 5 m and 10 m.

## 2.2 SWIR recordings

Figure 4 shows the recordings of plumes from the micro turbine engine as well as a full scale aircraft. No plume is visible for the micro turbine or the aircraft with non-afterburner engine setting. Only scintillation of the objects behind the (visually invisible) plume could be seen during measurements. It is not surprising that the afterburner plume, consisting of a dense gas and most probably carbon soot (creating a continuum spectrum), is visible – the emission for the afterburner is a result of this dense gaseous volume having an emission spectrum approaching that of a Planck radiator, as explained in the previous section. It must be noted that all three images in Figure 4 were obtained with a SWIR camera (Cedip SWIR), utilizing a InGaAs detector and band filter spanning only  $\lambda = 1.1 - 1.5 \mu\text{m}$ . A wider



response, covering the region of  $\lambda = 1 - 3 \mu\text{m}$ , should result in higher levels of IR energy detection due to the presence of a  $\text{CO}_2$  and water emission bands at  $2.7 \mu\text{m}$ <sup>6</sup>.

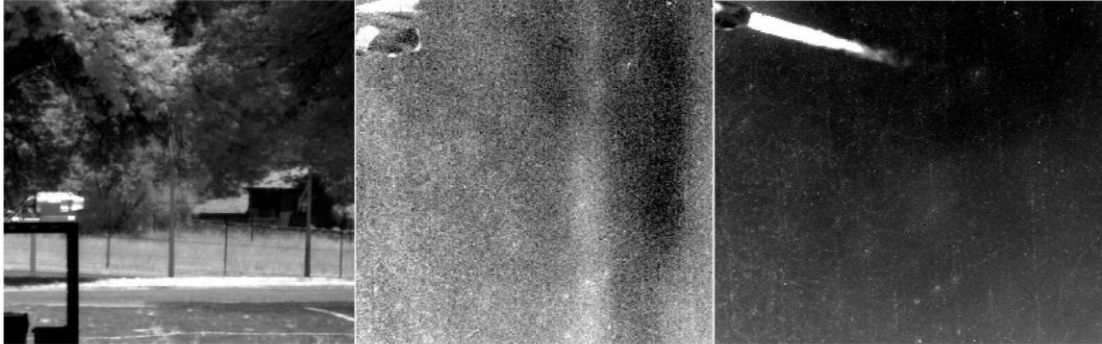


Figure 4. SWIR recordings of the micro turbine engine running at 135 000 RPM (left), rear end of aircraft at full thrust (middle) and aircraft at full thrust with afterburner (right).

### 2.3 MWIR recordings

In Figure 5 the plume of the micro turbine can clearly be seen as recorded with a MWIR camera (Cedip Jade) equipped with an InSb detector, sensitive in the wavelength region  $\lambda = 3.7 - 5.1 \mu\text{m}$ . The observed emission is mainly resulting from the flanks of the  $\text{CO}_2$  emission band centered around  $4.3 \mu\text{m}$ .



Figure 5. MWIR recordings of the micro turbine engine running at 135 000 RPM (left), rear end of aircraft at full thrust (middle) and aircraft at full thrust with afterburner (right).

### 2.4 LWIR recordings

LWIR recordings of the micro turbine plume were done with a Telops TEL-1000-VLW multispectral camera, covering the wavelength band of  $\lambda = 7.7 - 11.7 \mu\text{m}$  with its MCT detector. Figure 6 shows the subband filter transmissions of this multispectral imager. No image for the subband  $\lambda = 11.3 - 11.7 \mu\text{m}$  (rightmost spectrum in the figure) is shown, due to a problem experienced in the recording in this subband.

Close observation of micro turbine recordings in Figure 7 shows only the slightest indications of plume radiation in the subbands, appearing to be more prominent in the first few subbands covering the shorter wavelengths. The full band (i.e. no filter) recording of the plume is also shown in Figure 7, together with the full band recording when no plume is present and the engine is cold. These observations can be related to the water absorption lines in Figure 1, indicating that energy transitions observed in the LWIR band are most probably due to  $\text{H}_2\text{O}$  emissions.

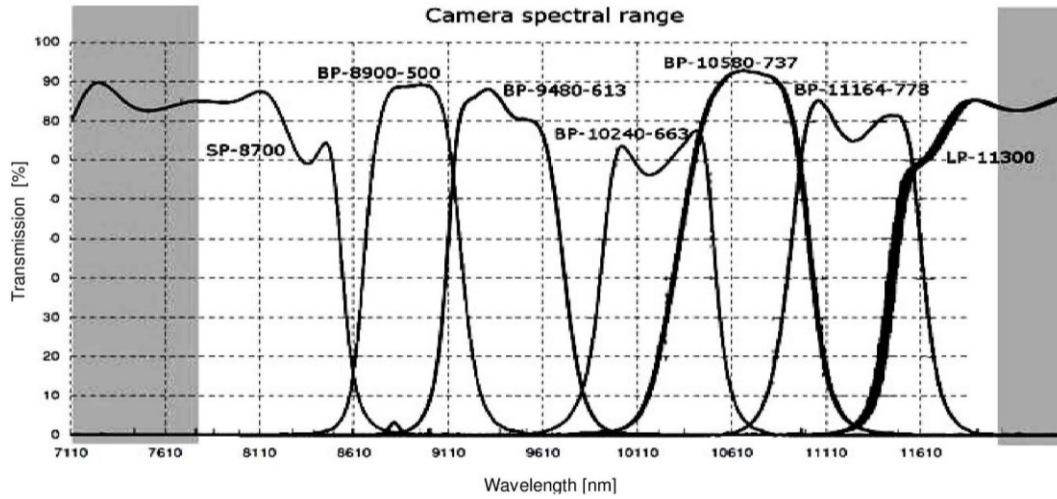


Figure 6. Filter transmissions of the Telops TEL-1000-VLW multispectral camera.

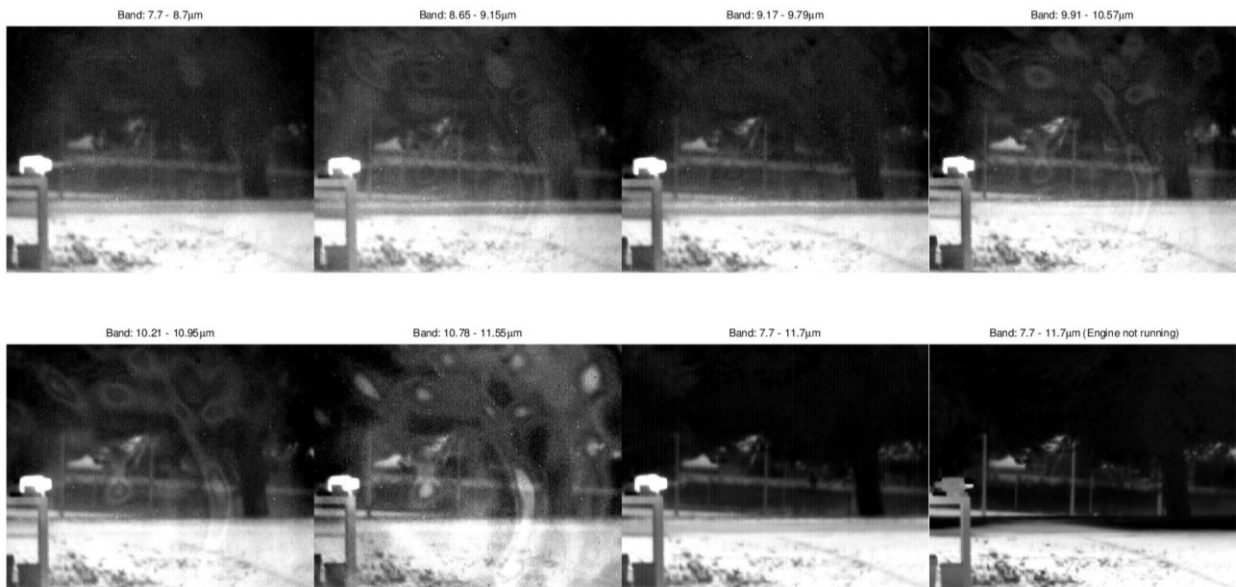


Figure 7. LWIR multispectral camera recordings of the micro turbine plume. The different bands are indicated for each image, with the full 7.7 – 11.7  $\mu\text{m}$  band image given in (row,column) position (2,3). The last image, i.e. position (2,4) – bottom right, is a recording of the cooled down engine while not in operation, for comparison with the other images during which the engine operated at the usual 135 000 RPM. Artefacts are present in some images due to unsatisfactory non-uniformity corrections.



## 2.5 Summary of plume observations

Table 1 shows a summary of the plume observations with the IR cameras and FTIR spectrometer in the different IR bands. The table is not complete, but populated mostly by the measurements done by the authors of the micro turbine plume or real aircraft.

Table 1. Summary of IR camera (IRC) and spectroradiometer (SR) observations in the different IR wavelength bands for a turbine plume originating from hydrocarbon fuel.

Wavelength region	Wavelengths covered by instrument	Plume emission agent	Plume condition	Emission strength (relative)
SWIR (1.1 – 2.5 $\mu\text{m}$ )	1.1 – 1.5 $\mu\text{m}$ (IRC)	$\text{H}_2\text{O}$	Normal	None
			Afterburner	Strong
	1.5 – 2.5 $\mu\text{m}$ (SR)	$\text{H}_2\text{O}$ , $\text{CO}_2$	Normal	Incomplete/noisy measurements
			Afterburner	No measurements
MWIR (2.5 – 7 $\mu\text{m}$ )	2.5 – 3.7 $\mu\text{m}$ (SR)	$\text{H}_2\text{O}$ , $\text{CO}_2$ (2.7 $\mu\text{m}$ )	Normal	None (some emission expected <sup>6</sup> )
			Afterburner	No measurements
	3.7 – 5.1 $\mu\text{m}$ (IRC + SR)	$\text{CO}_2$ (4.3 $\mu\text{m}$ )	Normal/Afterburner	Strong
	5.1 – 7 $\mu\text{m}$ (SR)	$\text{H}_2\text{O}$	Normal	Minimal
Afterburner			No measurements	
LWIR (7 – 15 $\mu\text{m}$ )	7 – 7.7 $\mu\text{m}$ (SR)	$\text{H}_2\text{O}$	Normal	Minimal
			Afterburner	No measurements
	7.7 – 11.7 $\mu\text{m}$ (IRC + SR)	$\text{H}_2\text{O}$	Normal	Minimal
			Afterburner	No measurements
11.7 – 15 $\mu\text{m}$ (SR)	$\text{H}_2\text{O}$ , $\text{CO}_2$	Normal	Minimal, more at longer wavelengths	
		Afterburner	No measurements	

## 3. IDENTIFICATION OF PLUME USING MWIR SUBBANDS

It should be apparent from the previous section that the most useful band for observing an aircraft plume is the MWIR band. The spectral information in this band was therefore chosen for a study concerning the automatic differentiation between an aircraft plume and a non-plume ‘hot’ object, also emitting IR waves.

Figure 8 shows the measured radiance of the blackbody from the previous section,  $L_{BB \rightarrow 5m}(\lambda, T)$ , with temperature  $T = 540^\circ\text{C}$ , and that of the micro turbine plume,  $L_{plume \rightarrow 5m}$ , measured through 5 m of atmosphere, together with modelled measurements through 15 m and 50 m of atmosphere. The modelled radiances were obtained by multiplying the measured radiance over 5 m with the transmittance mentioned in Section 2.1, e.g. for 10 m of atmosphere  $L_{BB \text{ modelled} \rightarrow 10m} = L_{BB \rightarrow 5m}(\lambda, T)\tau_{5m}(\lambda)$ , where the distance through the intervening atmosphere being modelled increases by 5 m each time the radiance is multiplied by  $\tau_{5m}(\lambda)$ . Extrapolations of the modelled measurements were limited to a maximum distance of 50 m, i.e. for the blackbody  $L_{BB \text{ modelled} \rightarrow 50m} = L_{BB \rightarrow 5m}\{\tau_{5m}(\lambda)\}^9$ .

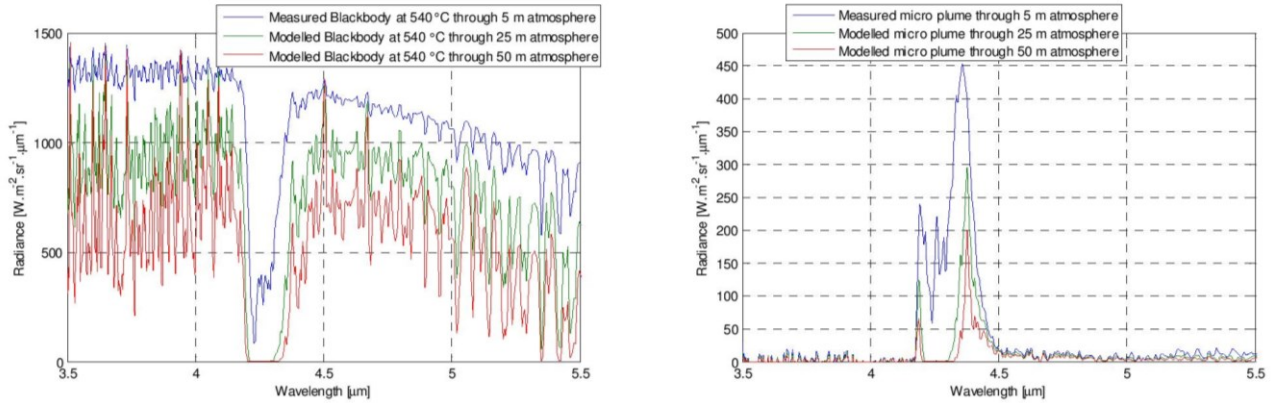


Figure 8. The radiance spectra of a blackbody (left) and micro turbine plume (right) as measured through a 5 m thick atmosphere, and modelled measurements for two thicker atmospheric paths through 25 m and 50 m. The blackbody has the same temperature as the exhaust gas temperature of the turbine.

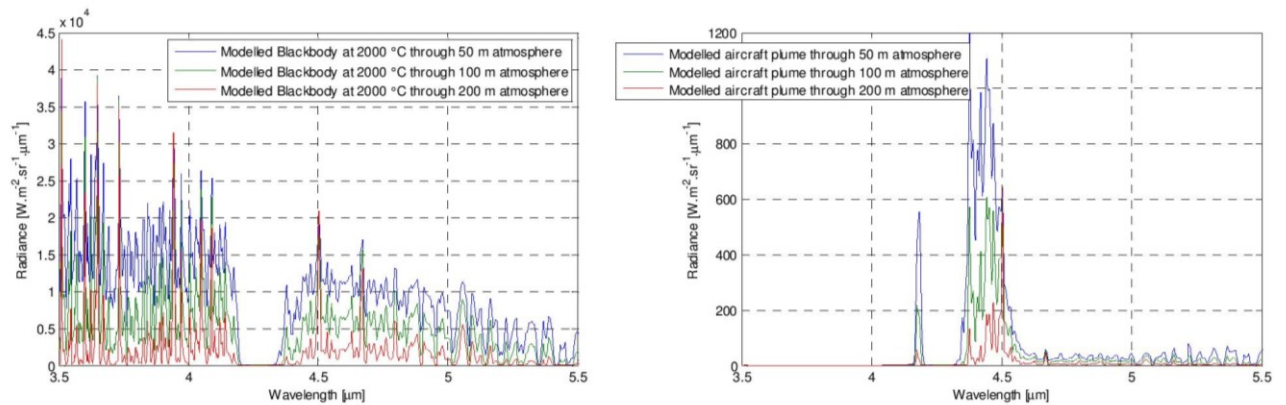


Figure 9. The modelled radiance spectra of a blackbody (left) and full scale turbine aircraft plume (right) as measured through a 50 m, 100 m and 200 m thick atmosphere. The blackbody has the same temperature as the nominal temperature of a typical aircraft countermeasure flare.

Figure 9 shows the modelled radiance of a blackbody at 2000°C through 50, 100 and 200 m of atmosphere. This temperature was chosen as it is in the order of the temperature of an aircraft countermeasure flare<sup>10</sup>, which has a typical blackbody spectrum. Also shown is the modelled full scale aircraft radiance spectrum obtained by applying a typical plume emissivity spectrum (from [2]) to a blackbody spectrum at 700°C, representing the gas exhaust temperature of a real scale aircraft. Although the temperature of the exhaust gas drops after exiting the exhaust nozzle<sup>6</sup>, this temperature was chosen deliberately to be higher by a fair amount than that of the micro turbine in order for the study a span a reasonable range of plume temperatures. Comparison of the plume spectra in Figures 8 and 9 shows the usefulness of micro turbine measurements due to the similarity in its spectrum with that of a real aircraft.

The modelled blackbody and plume spectra over various distances were used in attempting to obtain a spectrum-based method to distinguish the plume (micro turbine or full scale aircraft) from a blackbody (decoy). Use was made of the division of the MWIR wavelength band into three subbands, i.e. ,  $\lambda_{3.5-4.1\mu\text{m}}$ ,  $\lambda_{4.1-4.6\mu\text{m}}$   $\lambda_{4.6-5.5\mu\text{m}}$ . The 1<sup>st</sup> subband is to the left of the CO<sub>2</sub> emission band, the 3<sup>rd</sup> subband is to the right of the CO<sub>2</sub> emission band, and the 2<sup>nd</sup> band defines a narrow wavelength region around the CO<sub>2</sub> emission band. The spectral radiances within each band were integrated over wavelength, e.g.  $L_{3.5-4.1\mu\text{m}} = \int_{3.5\mu\text{m}}^{4.1\mu\text{m}} L_{BB}(\lambda, T = 700^\circ\text{C})\epsilon_{plume}(\lambda)\tau_{atm}(\lambda)d\lambda$  for the full scale aircraft plume (where  $\epsilon_{plume}$  is the spectral plume emissivity and  $\tau_{atm}$  the atmospheric spectral transmittance), to obtain the subband radiance

values  $L_{3.5-4.1\mu m}$ ,  $L_{4.1-4.6\mu m}$  and  $L_{4.6-5.5\mu m}$  for each of the modelled distances. The subband radiance values were used to test the possibility of obtaining a parameter that can be used to categorize an observed object into a legitimate ‘target’, i.e. aircraft plume, and a non-target, i.e. blackbody/flare decoy. This parameter should be relatively unaffected by the weakening of the object’s radiance signature due to transmission losses through the atmosphere.

The following parameters were established:

1. The ratio of the central subband and the sum of the three subbands:  $A = \frac{L_{4.1-4.6\mu m}}{L_{3.5-5.5\mu m}}$
2. The ratio of the central subband and the sum of the two side subbands:  $B = \frac{L_{4.1-4.6}}{L_{3.5-4.1\mu m} + L_{4.6-5.5\mu m}}$

Figure 10 shows parameters A and B for the micro turbine plume and a blackbody of similar temperature than the plume, as well as a blackbody at the typical flare temperature. Parameter A differs by a factor of between 3 and 4 between the plume and 540°C blackbody, and by roughly a factor 4 for the 2000°C blackbody.

Parameter B is even more promising in differentiating between the plume and blackbodies – it differs by a factor 10 or more over the range indicated when comparing its value for the plume with that of either the low or high temperature blackbody.

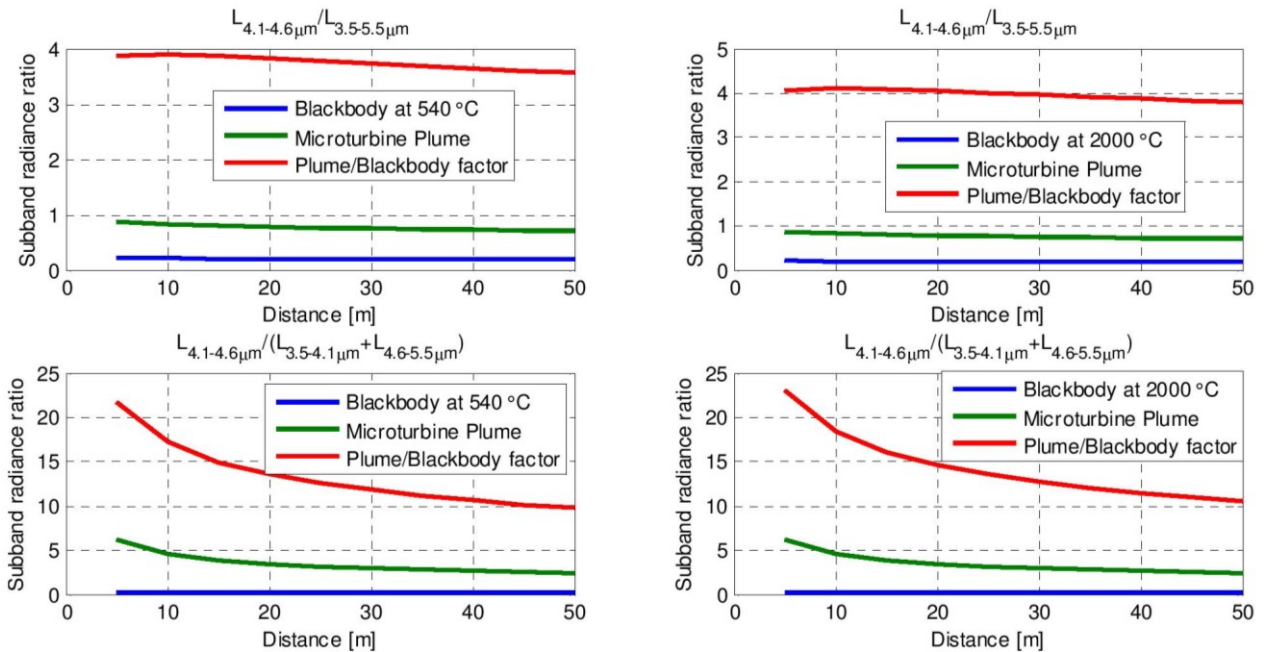


Figure 10. Different subband radiance ratios of a blackbody and micro turbine plume as observed through the atmosphere.

Figure 11 shows the results of the same calculations that were done for Figure 10, but for the full scale modelled aircraft plume and over longer distances. In these results it can also be seen that parameter B is more effective than A in distinguishing between the plume and a blackbody representing a flare – in fact, the factor difference between the plume and blackbody of 20 or more for parameter B is even higher for this modelled real scale aircraft and flare than for the micro turbine plume and blackbody, even though a wider range of distances were used. From this study it is clear that parameter B provides the most promising way for the automatic subband based recognition of an aircraft plume amongst decoy objects like flares.

In practice these subband radiance values can be obtained by e.g. using a set of two filters alternating in front of a MWIR detector – one filter being a narrow band filter transparent in the 4.1 – 4.6  $\mu m$  range, and the other filter blocking this  $CO_2$  band.



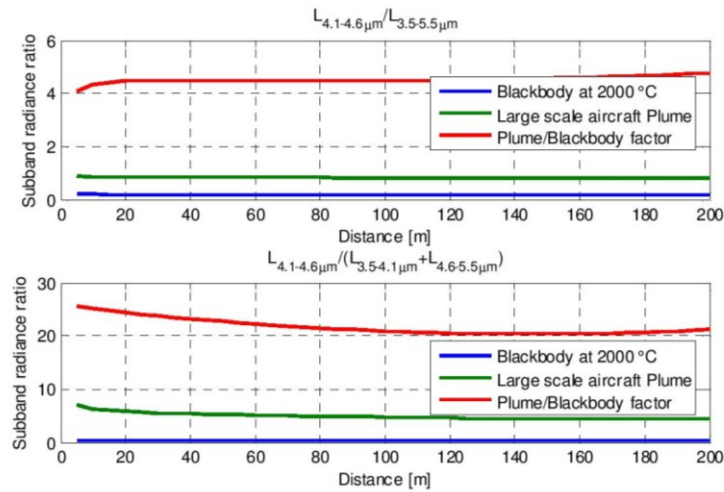


Figure 11. Different modelled subband radiance ratios of a blackbody/flare and a real scale aircraft plume through the atmosphere.

It must be noted that for modern decoy aircraft countermeasures, it is attempted to mimic the radiance spectrum of an aircraft plume. Older generation flares, e.g. MTV flares<sup>10</sup>, have a typical blackbody/Planck spectral distribution of their emitted radiation. In striving to mimic an aircraft plume, the chemical reactions in the modern generation flares are engineered to emulate the combustion of the plume through the creation of a CO<sub>2</sub> emitter. For such countermeasures, the MWIR subband method of differentiating between a plume and countermeasure must be used in conjunction with other methods taking cognizance of the dynamics, shape, relative size etc. of the object to be classified.

Any method, procedure or algorithm like the above described plume identification technique, needs to be tested more thoroughly to establish its robustness. The measurements required to characterize a plume sufficiently so that a mathematical model can be constructed for use in such robustness tests, are described in the following section.

#### 4. RECORDINGS FOR AIRCRAFT PLUME CHARACTERIZATION

The exact form and amplitude of the IR wavelength spectrum for a specific line of sight (LOS) directed towards an aircraft plume, depends on the distribution of the plume temperatures and density of emitting molecular species<sup>6</sup> throughout the thickness of the plume being traversed by the LOS. These parameters depend, in turn, on the fuel consumption of the turbine which converts the fuel into energy and the emitting molecular species in the plume, as shown earlier. The fuel consumption is affected by, amongst others, the following factors:

- The specific engine setting of the turbine – Expressed as percentage of the maximum revolutions per minute – %RPM<sub>max</sub>; higher %RPM<sub>max</sub> values lead to increased fuel flow and therefore increased IR emission,
- The specific engine type – e.g. turbojet vs. more fuel efficient turbofan with lower IR emission,
- The altitude of the aircraft – the density of atmospheric air, acting as oxidizer for fuel, changes with altitude; higher altitude results in lower fuel consumption and lower IR emission,
- The drag of the aircraft – more drag requires more thrust to maintain a specified speed, i.e. more fuel and higher IR emission,
- The load of the aircraft – bombs, missiles, etc., increases the aircraft's mass and more fuel is required, i.e. higher IR emission,
- The velocity of the aircraft – higher velocity increases air pressure at turbine intakes – Ram effect – and consequent thrust and fuel consumption increase, i.e. higher IR emission.

Keeping the above factors constant, the measured radiance values also vary according to the specific angle and position of the intersection of the LOS with the main axis of the plume, thereby changing the ‘thickness’ of plume traversed by the LOS and the specific temperatures and densities of the plume molecules encountered along the LOS. The plume *intensity* (as opposed to radiance) takes the emission of the whole plume into account by integrating the emitted radiance, from each position of the LOS through the plume, over the total area of the plume. This value can, like radiance, either be a spectral value or wavelength band integrated value. It should be obvious that the plume intensity will also be affected by most of the factors influencing the radiance of the aircraft plume.

It can be seen that the above mentioned factors influencing the IR emission would be specific to i) the aircraft under investigation, and ii) the observation configuration with respect to the aircraft. In a study reported on in [1], the radiance and intensity dependence of a turbojet fighter aircraft plume was investigated by doing in-flight recordings at different altitudes (i.e. different fuel consumptions) and aspect angles (observation configurations). Figure 12 illustrates the effect of aspect angle (angle between aircraft nose and LOS) on the intensity as determined by the size of the projected area associated with the specific aspect angle and the area of the plume obscured by the aircraft fuselage. Also shown in Figure 12 are the vertical radiance profiles through the plume at an altitude of 900 m, and the horizontal radiance profiles through the plume at different altitudes.

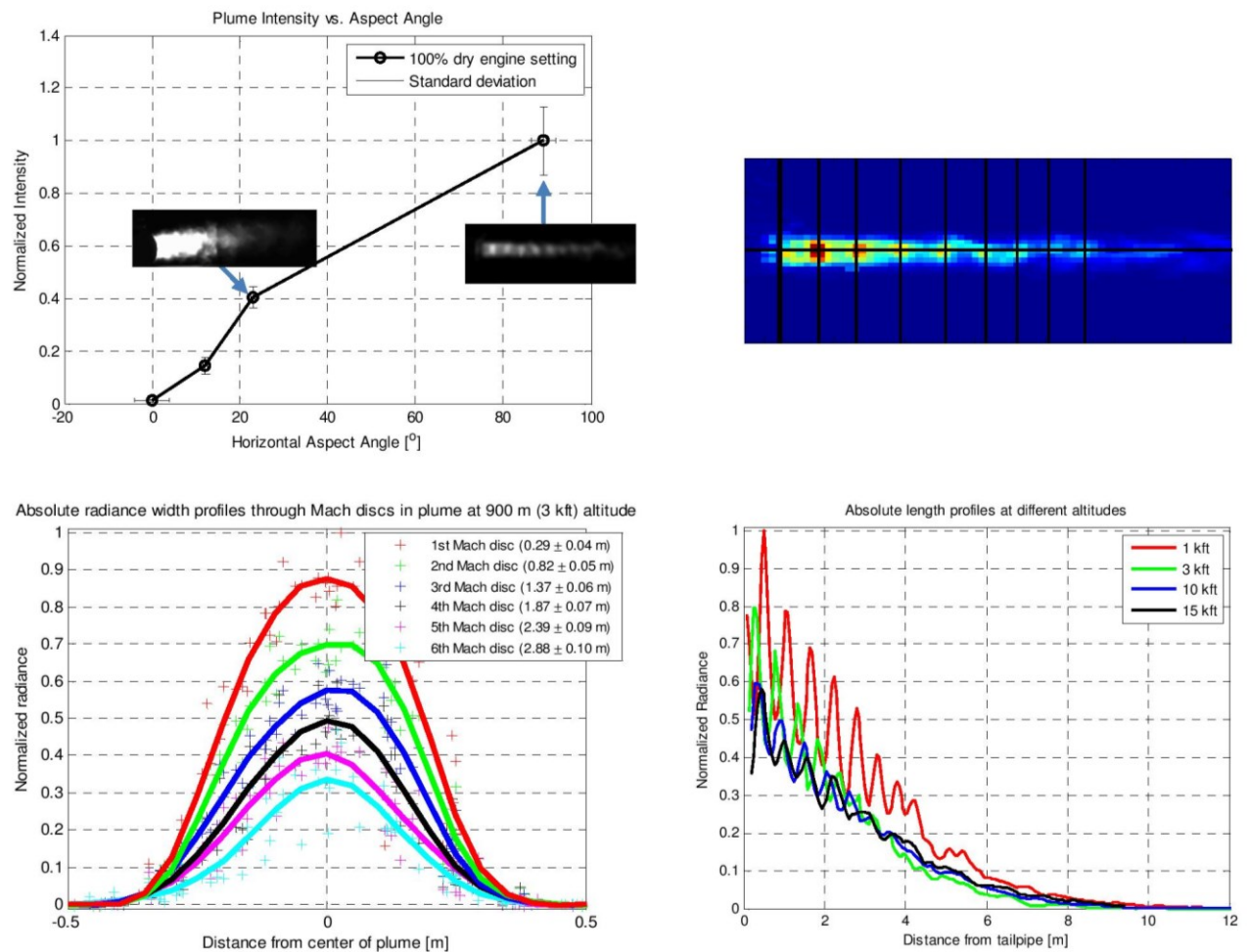


Figure 12. Measured aircraft plume MWIR band intensity as a function of aspect angle of the aircraft is shown in the top left graph; Vertical MWIR band radiance profile lines through the Mach discs of the top right image of the plume are shown in the bottom left graph; Horizontal MWIR band radiance profile lines, similar to the one in the top right image, are shown for different altitudes in the bottom right graph respectively.



All radiances and intensities shown in Figure 12 are the *absolute* (and normalized) radiometric values, i.e. the measured values after corrections for atmospheric attenuation, background emission of the background through the plume and the instrument spectral response of the MWIR camera. Such absolute values can be interpreted as the radiance or intensity values that would be measured with an ideal camera, having a flat spectral response within its wavelength band, right next to the plume, so that the atmosphere or background does not influence the measured energy from the plume. Such recordings, however, still represent the ‘projected’ values, i.e. the energy accumulated along the LOS through the partially transparent plume. In order to be able to create a mathematical (computer) model of the plume, these projected values must be further processed by means of a technique of radiance inversion. The following section will briefly touch on the corrections to be applied to the measurements and the processing thereof in order to obtain a plume model.

## 5. DATA REDUCTION AND INFRARED PLUME MODEL CONSTRUCTION

In Section 2 of this article, measurements were done with a spectroradiometer (SR) having a FOV which recorded the radiance spectrum of the plume as a whole. As the FOV is progressively changed to smaller values, the recorded spectrum would become less of an averaged spectrum for the plume as a whole and more of a local spectrum associated with a LOS through a specific position in the plume. Measurements were also done with IR cameras, which presented spatially resolved images with more than one pixel simultaneously covering the plume area, but each of the pixel radiance values consisted of the integrated spectral radiance over the sensitivity band of the camera. Ideally, plume measurements should consist of spectral radiance measurements as well as spectral transmittance measurements of the plume, sampled simultaneously over the whole spatial area covered by the plume, as can be done with a hyperspectral imager<sup>11</sup>. Such measurements simplify the processes of data reduction in order to obtain the absolute radiometric values of the plume, as well as radiance inversion in order to obtain the inner structure of the plume so that a three dimensional plume model can be constructed. A brief overview of the data reduction for such ideal measurement data will now be given, while the data reduction procedure for the first mentioned, non-ideal measurements can be found in [1] and [2].

The spectral radiance measured if an instrument is directed towards a specific position on an aircraft plume, can be described by the following spectral measurement equation:

$$L_{meas}(r) = L_{plume}(\lambda)\tau_{atm}(r, \lambda)\tau_{instr}(\lambda) + L_{bkg}(r, \lambda)\tau_{plume}(\lambda)\tau_{atm}(r, \lambda)\tau_{instr}(\lambda) + L_{path}(r, \lambda)\tau_{instr}(\lambda), \quad (1)$$

where  $r$  is the distance between the instrument and the plume,  $\tau_{instr}$  is the total responsivity of the instrument, i.e. detector response including lens and other optical element transmissions,  $L_{bkg}$  is the radiance of objects behind the plume,  $\tau_{plume}$  is the transmittance through the plume, and  $L_{path}$  is the radiance resulting from the atmosphere between the instrument and the plume. The remaining symbols are similar to their previous definitions in Section 2. This equation can be rewritten to form a data reduction equation, from which the plume spectrum follows:

$$L_{plume}(\lambda) = \frac{L_{meas}(\lambda) - L_{bkg}(r, \lambda)\tau_{plume}(\lambda)\tau_{atm}(r, \lambda)\tau_{instr}(\lambda) - L_{path}(r, \lambda)\tau_{instr}(\lambda)}{\tau_{atm}(r, \lambda)\tau_{instr}(\lambda)}. \quad (2)$$

The plume spectrum can be written as the product of a blackbody spectrum at a specified temperature,  $T_{plume}$ , and a emissivity spectrum,  $\varepsilon_{plume}$ , i.e.

$$L_{plume}(\lambda) = L_{BB}(\lambda, T_{plume})\varepsilon_{plume}(\lambda). \quad (3)$$

It is important to realize that the emissivity of a gaseous volume, where it is assumed that the reflection against the volume is zero, is related to the transmittance through the volume by

$$\varepsilon_{plume}(\lambda) = 1 - \tau_{plume}(\lambda) \quad (4)$$

and that

$$\tau_{plume}(\lambda) = 1 - e^{-\kappa(\lambda)l}, \quad (5)$$



where  $\kappa(\lambda)$  [ $\text{m}^{-1}$ ] is the absorption coefficient of radiation at the wavelength  $\lambda$ , and  $l$  is the distance travelled through the absorbing medium, i.e. the plume. It should be clear from (4) and (5) that the path length of the LOS through the plume determines the value of the transmittance, which in turn determines the value of the emissivity – therefore the observed radiance is influenced by the angle of the LOS with the main axis of the plume, since this angle determines the path length of the LOS within the plume volume.

In order to obtain the internal structure of the plume, a variation of the ‘Finite Width Onion Peel Inversion’ can be used<sup>2</sup>. For this technique, measurements at an aspect angle of  $90^\circ$  of the plume are required (as were done in the recordings in Section 2) and an axisymmetric plume model, consisting of annular regions of one pixel thick and considered to be homogeneous in temperature, pressure and molecular species and their densities, is assumed. The plume is then ‘sliced’ in order to obtain cross sections like that shown in Figure 13 – these slices should be as thin as possible, i.e. one pixel wide.

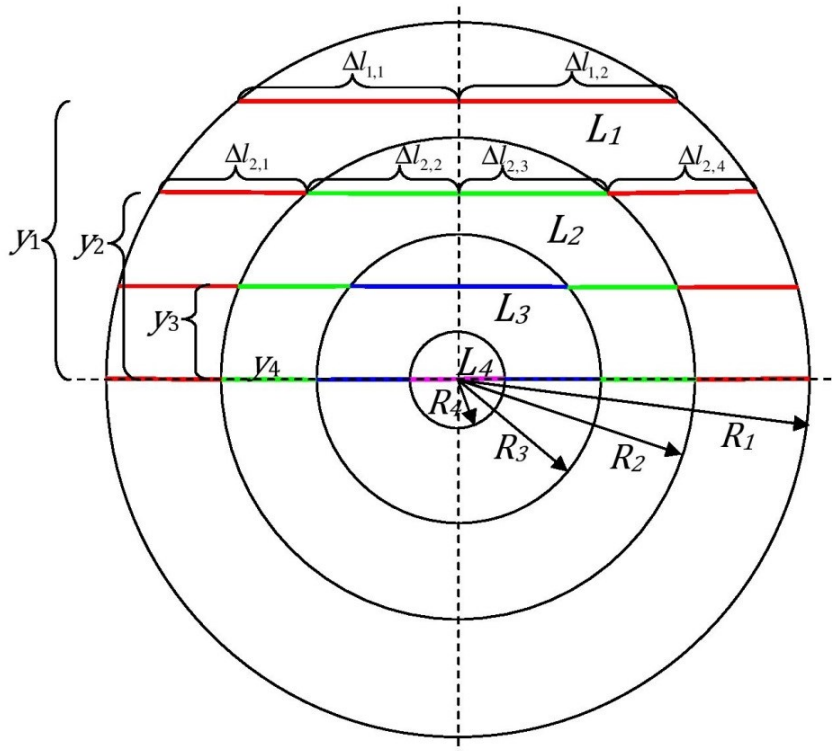


Figure 13. Schematic diagram representing a cross section (slice) through the plume of an annular plume model. The homogeneous, annular regions in the slice, marked with a specific radiance value  $L_i$ , are confined by the radii  $R_i$ , and the height of each LOS above the axis of the plume for an observer looking from the right side of the plume (at a  $90^\circ$  aspect angle) is indicated by  $y_i$ . The segments of each LOS within the different homogeneous regions of the plume are marked as  $\Delta l_{i,j}$ .

The following set of equations can now be obtained (in matrix form) for the case shown in Figure 13, i.e. where the number of annular regions is four:

$$\begin{bmatrix} \alpha_{1,1} & 0 & 0 & 0 \\ \alpha_{2,1} & \alpha_{2,2} & 0 & 0 \\ \alpha_{3,1} & \alpha_{3,2} & \alpha_{3,3} & 0 \\ \alpha_{4,1} & \alpha_{4,2} & \alpha_{4,3} & \alpha_{4,4} \end{bmatrix} \begin{bmatrix} L_{BB1} \\ L_{BB2} \\ L_{BB3} \\ L_{BB4} \end{bmatrix} = \begin{bmatrix} L_{proj1} \\ L_{proj2} \\ L_{proj3} \\ L_{proj4} \end{bmatrix} \quad (6)$$

In this representation

$$\alpha_{i,j} = \varepsilon_{i,j} (\prod_{h=j+1}^{2i} \tau_{i,h} + \prod_{h=1}^{j-1} \tau_{i,h}), \quad (7)$$

with  $\alpha_{i,j} \equiv 0$  for  $i < j$  and  $\tau_{i,h} = \exp(-\kappa_i \Delta l_{i,h})$  and  $\varepsilon_{i,h} = 1 - \tau_{i,h}$ . If no estimate of  $\kappa_i$  is known, it can be determined for each annular region from the plume transmission measurements with the procedure given in [2].

The above matrix equation can be written in bold symbols, representing matrices, as

$$\boldsymbol{\alpha} \mathbf{L}_{BB} = \mathbf{L}_{proj}, \quad (8)$$

and it can easily be solved for  $\mathbf{L}_{BB}$  at each value of  $\lambda$ , i.e

$$\mathbf{L}_{BB} = \boldsymbol{\alpha}^{-1} \mathbf{L}_{proj}. \quad (9)$$

It must be kept in mind that the above quantities are all spectral, i.e. the parameters in (6) - (9) are all three dimensional matrices.

During this radiance inversion, the LOSs were all perpendicular to the main axis of the plume. The radiance values should, however, be calculable for aspect angles other than  $90^\circ$  in a model that represents the plume radiance in a simulation environment. The first step in determining the radiance for an arbitrary aspect angle is to parameterize the LOS. Having a description in three-dimensional space of the LOS after parameterization, the second step is to calculate the intersections of this LOS with the boundaries of each annular region and boundary planes of each slice of the plume, so that the distances traversed in each annular region within each slice can be determined. With these new distances, the emissivity and transmission of each segment of the LOS in a specific annular region and plume slice can be calculated.

## 6. CONCLUSION

The usefulness of a cost effective micro turbine engine for concept plume studies related to full scale aircraft plumes, were demonstrated. This was made possible by the similarity in the combustion process of a small scale turbine vs. a full scale turbine engine.

It was also shown that the MWIR band is the most versatile regarding plume observations, although emission might be detected at other wavelengths outside this band. A method using subbands in the MWIR wavelength band was demonstrated to be able to differentiate between an aircraft plume and a decoy object with a blackbody like emission spectrum. This spectral based subband method have, however, to be used in conjunction with other non-spectral methods to differentiate between aircraft plumes and decoy objects emulating  $\text{CO}_2$  emitters.

The fuel consumption of an aircraft and the observation configuration were found to be the main influences on the detected emission of an aircraft plume. Measurements in which parameters related to these factors are studied contribute towards the characterization of the emission from an aircraft plume. These measurements, when recorded at an angle of  $90^\circ$  between the observer LOS and the main axis of the plume, can be processed to remove unwanted influences on the plume radiance values, followed by the application of a radiance inversion technique to obtain the plume inner structure. Once the plume inner structure is obtained, a model can be constructed for use in simulations of plume recordings in order to test algorithms related to plume recognition under conditions for which no recordings exist.

## REFERENCES

- [1] Retief, S. J. P., Smit, P., Dreyer, M. M., "Mid-Wave infrared characterization of an aircraft plume", Proc. IEEE Saudi International Electronics, Communications and Photonics Conference (SIEPCPC), 1-6, (2011)
- [2] Retief, S. J. P., "Aircraft plume infrared inversion and subsequent simulation model", Proc. SPIE 85430, 85430P-1 – 85430P-15 (2012).
- [3] Holst, G. C., [Electro-Optical imaging system performance, 3<sup>rd</sup> edition], SPIE Optical Engineering Press (2003).
- [4] Bathie, W.W., [Fundamentals of gas turbines], John Wiley & Sons, 63-64 (1984).
- [5] Hecht, E., [Optics – Second Edition], Addison-Wesley Publishing Company, 263-264 (1987).
- [6] Hudson, R. D., [Infrared System Engineering], John Wiley&Sons (1969).

- [7] Sircilli, F., Retief, S.J.P., Magalhães, L. C., Ribeiro, L. R., Zanandrea, A., Brink, C., Nascimento, M. and Dreyer, M. M., "Infrared characterization of a micro turbine engine plume", XV Symposium on Operational Applications in Defence Areas (XV EMIS), Brazil, 107-112 (09/2013)
- [8] Wormhoudt, J., [Infrared methods for gaseous measurements], Marcel Dekker, Inc. (1985)
- [9] Rudman, S., Hibbeln, B.A., "Scaling of optically thick plume signatures", Aerospace Conference Proceedings, IEEE, Vol. 3, 265-270 (2000).
- [10] Magalhães, L. B., Alves, F. D. P., "Estimation of radiant intensity and average emissivity of Magnesium/Teflon/Viton (MTV) flares", Infrared Imaging Systems: Design, Analysis, Modelling and Testing, Proc. SPIE 7662, 766218-1 – 766218-10 (2010).
- [11] Tremblay, P., Gross, K. C., Farley, V., Chamberland, M., Villemaire, A., Perram, G. P., "Understanding and overcoming scene-change artifacts in imaging Fourier-transform spectroscopy of turbulent jet engine exhaust", Proc. SPIE 7457, 74570F-1 – 74570F-13 (2009)

## **CHAPTER 4      MID-WAVE INFRARED CHARACTERIZATION OF AN AIRCRAFT PLUME**

### **4.1 INTRODUCTION**

With the relevance of the MWIR band in the detection of aircraft plumes indicated in Chapter 3, the method of MWIR characterization of an aircraft plume is now presented by the publications in Sections 4.2 [3] and 4.3 [4]. The bespoke software mentioned in Sections 1.4 and 2.3 (which is under continual development) was used in the data reduction of all the measurements referred to in these publications.

Great care was taken in the preparation of the measuring system described in Section 4.2, since this system (with the main components being the MWIR camera and its control PC) would be subjected to potentially large temperature variations and severe vibrations after installation inside an instrumentation pod suspended from an aircraft wing pylon. The MWIR camera had to be ruggedized after structural weaknesses were identified during a modal test on the camera. Furthermore, vibration mounts for the camera and its control PC were selected and tested in accordance with the known vibration spectrum to which the equipment in the pod would be subjected to during flight. Although the pod itself was not deliberately designed to thermally isolate the measuring system inside it from its outside environment, it offered enough protection to the camera so that the camera housing temperature (logged during recordings) never varied by more than 10 °C during each of the measuring sorties (having a typical duration of one hour) in which measurements were made at altitudes varying from 305 m to 4574 m. The influence of this variation in housing temperature on the camera output was estimated to be small enough so that it was considered acceptable to use the calibration tables created from laboratory measurements at constant camera housing temperatures during data reduction.

A high-level diagram of the measurement system used is shown in Figure 4-1. The recordings were controlled by the flight engineer in the rear seat of a dual-seater fighter aircraft while the live infrared image seen by him was also transmitted to the ground control station. Verbal instructions

regarding the initiation and termination of the recordings were given from the ground control station.

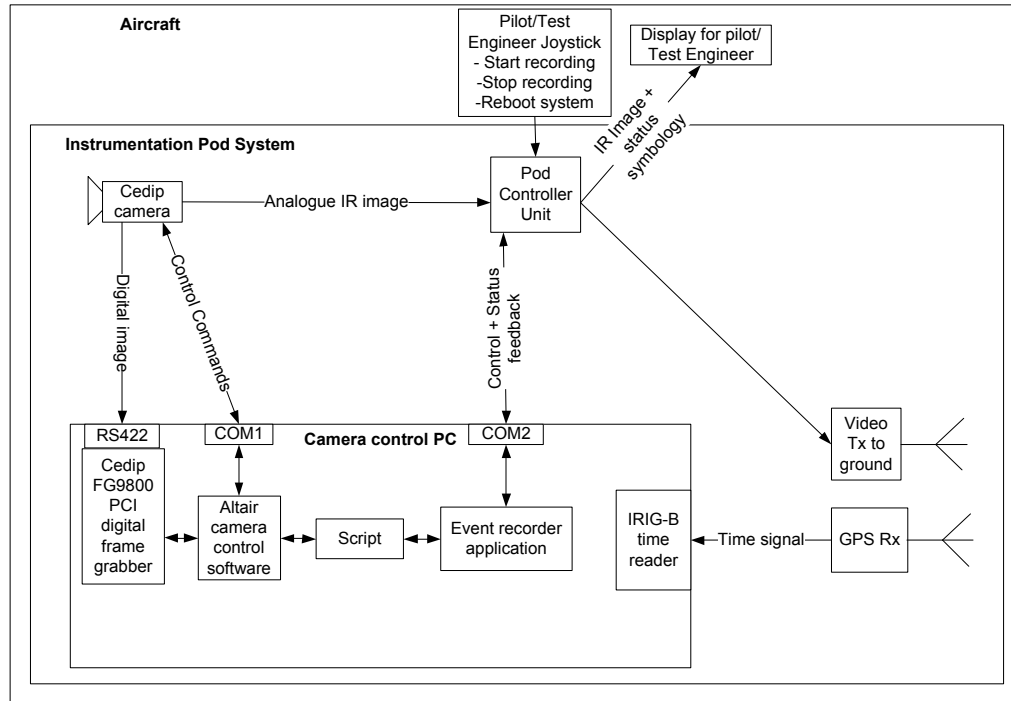


**Figure 4-1 The measurement system used in acquiring MWIR image sequences of an in-flight target aircraft.**

A MWIR radiance image recording of the target aircraft is shown in

Figure 4-2 for an off-nose aspect angle of approximately 10°. Before processing of the image can be done, it is first segmented into different parts of interest by means of, e.g., the application of a radiance threshold to the image as a whole, which then simplifies the manual selection of the region of interest. Each segmented part is treated differently during data reduction in the ways discussed in Section 4.2 in order to obtain the source radiance values – more focus is, however, placed on the treatment of the plume of the aircraft in this publication.

In Section 4.3, the measurements for the characterization of a turbine plume are repeated by using a micro turbine gas engine. This cheaper version of full-scale flight test measurements is done under almost-laboratory conditions, which allows for more measurement configurations resulting in a more complete characterization of the plume (although not *in situ*). It is argued in this publication that the similarity between a micro turbine engine plume and a large-scale aircraft turbine engine plume is sufficient for the purpose of concept infrared aircraft plume signature studies.



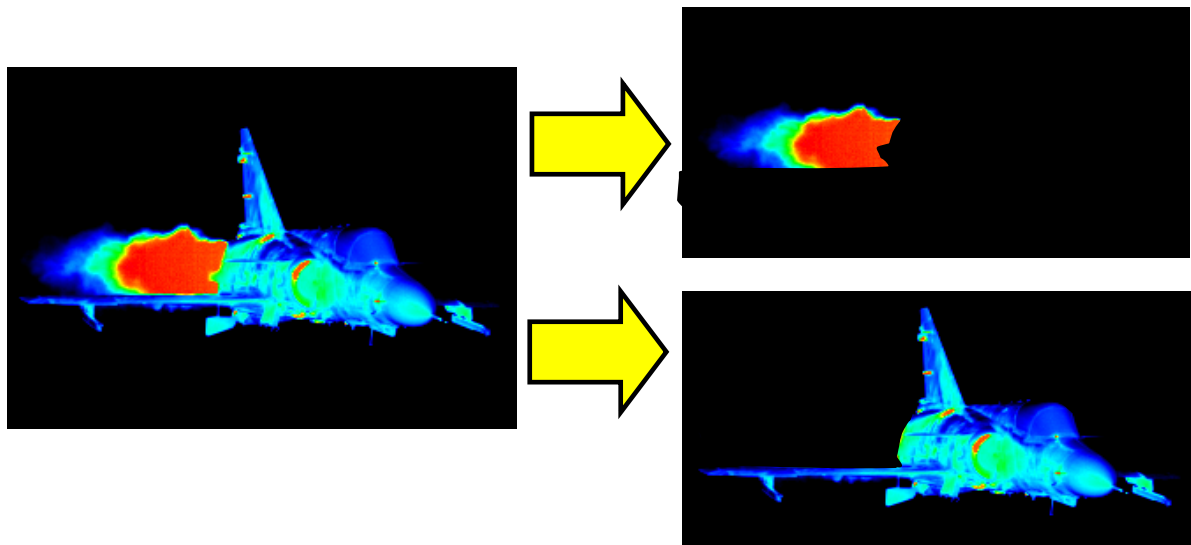


**Figure 4-2** Typical recording, shown in false colours, of the target aircraft. It is also shown how such an image is typically segmented into two images containing only plume pixels and fuselage pixels respectively. High to low radiance values are displayed in colours following the sequence of red (highest value), orange, green, light blue, dark blue and black (lowest value).

#### **4.2 PUBLICATION – MID-WAVE INFRARED CHARACTERIZATION OF AN AIRCRAFT PLUME**

The flight test during which the measurements were made consisted of a team effort in which the South African Air Force and personnel of Denel Dynamics took part. The present author contributed during the flight test towards:

- The planning of the flight configurations during the different sorties at various altitudes and target aircraft aspect angles with the associated, required instrument settings.
- Drawing up of the high-level functionality diagram for the measurement system (Figure 4-1).
- Ensuring the functionality of the measurement system by means of an acceptance test procedure (ATP) and operating procedures for use by the test flight engineer.
- Issuing instructions from the ground station during the flight test sorties regarding the operation of the measurement system and successful recordings.

The co-authors of this publication were involved in the organization of the flight test itself (M.M. Dreyer) and the processing of certain sorties (P. Smit). The remainder of the work, i.e. data processing, the publication itself and the results contained therein, was done by the present author.



The publication was reviewed by the conference chair/committee members of the conference where it was presented.

The article was published in the Proceedings of the Electronics, Communications and Photonics Conference (SIECPC) held in Riyadh, Saudi Arabia [3].

# Mid-Wave Infrared Characterization of an Aircraft Plume

SJP Retief\*, P Smit\*\*, MM Dreyer\*

Simulation and Design Department, Denel Dynamics  
Centurion, South Africa

\*paul.retief@deneldynamics.co.za, \*\*petrus.smit@deneldynamics.co.za, \*marlien.dreyer@deneldynamics.co.za

**Abstract**—Development of the tracking algorithms used in an infrared seekerhead missile requires the infrared characteristics of the target against which the missile will be directed. Mid-wave infrared recordings of such a target were made at altitude during a flight test. The measurement setup for this test is described, as well as the additional recordings required during data reduction afterwards. An exposition of the general theoretical approach used for the data reduction of infrared image recordings of targets is given and the minimum data required is inferred. The data reduction is then applied to the plume of the target aircraft. The results of the plume data reduction, consisting of mid-wave infrared radiance profiles at different altitudes and the effect of altitude as well as aircraft aspect angle on plume intensity are then presented.

**Keywords**- mid-wave infrared; aircraft plume; data reduction; intensity; radiance

## I. INTRODUCTION

In order to program infrared seekerhead missiles under development, the infrared properties of the intended targets against which the missiles will be directed need to be characterized. Such characteristics are usually not freely available in literature and typically need to be measured in-house. Having measured a specific target, a process of data reduction is applied in order to obtain the absolute target characteristics. During data reduction, unwanted influences on the target measurement, e.g. atmospheric attenuation of the target signal, path radiance of the atmosphere, background radiance transmitted through a partially transparent target, etc., are corrected for in order to obtain the absolute radiometric quantities. Having the absolute radiometric quantities, a computer model can now be constructed of the target. This target model is then used in a computer simulation together with a model of the infrared seekerhead missile. Tracking performance of the missile can now be tested under various simulated environmental conditions, providing opportunity for the development and improvement of the target tracking algorithms employed by the missile model.

In order to test the capabilities of infrared imager missiles under development at Denel Dynamics, an attempt was launched to characterize a turbojet fighter aircraft. A flight test was conducted with the main goal of recording the fighter

aircraft's plume shape, intensity and radiance profiles at different altitudes above sea level and at different aspect angles.

The setup used for these measurements is presented in Section II, with the theoretical approach used during data reduction being presented in Section III. The characteristic information of the target aircraft extracted from the data is presented in Section IV, with a conclusion given in Section V.

## II. FLIGHT TEST SETUP

For characterization of the target aircraft plume, measurements at different aspect angles of the aircraft, as well as at different altitudes, ranging from sea level up to about 4700 m (15 kft), were required. An infrared camera was installed in a pod (detachable container) attached to a carrier aircraft so that images of the target aircraft could be captured at altitude. The pod setup, the sorties flown and the complementary data recorded during the flight test are now described.

### A. Pod configuration

A Cedip Jade III Medium Wave Infrared (MWIR) camera [1], with sensitivity range covering 3.7 – 5.1  $\mu\text{m}$ , was installed into a pod hanging from the wing of a carrier aircraft as shown in Fig. 1. The camera could view the outside world through a Silicon (Si) window, which is transparent for electromagnetic waves within the MWIR band. The camera was controlled by the test flight engineer, sitting in the rear of this dual seat aircraft, allowing him to make recordings at altitude. A display in the cockpit enabled the flight engineer to view real-time images from the camera.

A more complete characterization of a target might require Short Wave Infrared (SWIR), Long Wave Infrared (LWIR) and spectral measurements in addition to the MWIR measurements. However, due to a limitation in the available physical space in the instrumental section of the pod, only the inclusion of a small visual band CCD camera was allowed.



Figure 1. The pod containing the backward facing MWIR camera. This camera is directed towards the target aircraft through the circular Si window. The rectangular perspex window above the Si window allows a visual camera to be installed for the purpose of reference recordings.

The MWIR camera could be mounted in one of the four predetermined backward facing yaw angles, i.e.  $0^\circ$ ,  $10^\circ$ ,  $20^\circ$  and  $90^\circ$ , with reference to the major axis of the pod. These different mounting angles allowed the target aircraft to be recorded at different aspect angles. The multi-integration time (multi-IT) setting of the camera was used in order to extend the dynamic range of the recordings. The extended range resulted in useable data of both the relatively hot plume and the relatively cold fuselage of the target aircraft being captured simultaneously. The additional fuselage data could then be processed as well, even though fuselage measurements were not the main objective of the test.

#### B. Flight Sortie configuration

Altogether four sorties were flown at a military power engine setting, i.e. at a maximum revolution rate setting of the turbojet engine of the target aircraft. For each sortie, the camera was mounted at a specific yaw angle (e.g.  $20^\circ$ ) and recordings were then performed at different altitudes, i.e. 305 m (1 kft), 915 m (3 kft), 3049 m (10 kft) and 4574 m (15 kft) respectively.

During a sortie, at each of the above mentioned altitudes, the target and pod-carrier aircraft flew a ‘racecourse’ track. During each leg of the course, a straight and level path was flown for approximately 30 – 40 s during which recordings were made. Fig. 2 shows a schematic diagram of the flight configuration.

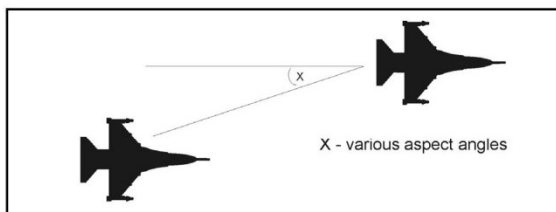


Figure 2. Flight configuration of the pod-carrier (right) and target (left) aircrafts. Different mounting angles of the camera,  $X = 0^\circ$ ,  $10^\circ$ ,  $20^\circ$  and  $90^\circ$ , allowed recordings of the Target aircraft at these aspect angles.

#### C. Complementary Data Recordings

In order to process MWIR recordings of the target aircraft, certain complementary data are required. These data were obtained from the Overberg Toetsbaan, where the test was carried out, in the form of time-stamped trajectories of both carrier and target aircraft, as well as meteorological parameters.

The trajectories permit, among other things, the calculation of separation distances between the two aircraft and exact altitudes during recordings. The meteorological data consisted of altitude profiles of atmospheric parameters like pressure, temperature, relative humidity, wind speed and wind direction. These recordings were obtained from a weather balloon released into the atmosphere shortly before or after each sortie. The profiles, characterizing the atmosphere, become relevant during data reduction when the influence of the atmosphere on the recordings needs to be compensated for.

### III. THEORETICAL APPROACH USED IN DATA REDUCTION

The general theory behind the method used to abstract useful information from the recorded infrared images will first be described, and then the application of this method to the partially transparent fighter aircraft plume will be explained.

#### A. Theory

Contributions to the infrared signal observed by the camera when directed towards a target situated at a distance  $r$  and elevation angle  $\theta$  with respect to the camera, will usually consist of, but are not necessarily limited to, the following spectral entities (wavelength represented by  $\lambda$ ):

- The absolute target radiance,  $L_{trg}(\lambda)$ , attenuated by the atmosphere.
- The background radiance,  $L_{bkg}(r, \theta, \lambda)$ , whenever the target is semi-transparent, attenuated by the target as well as the atmosphere.
- The environmental radiance,  $L_{env}(r, \theta, \lambda)$ , as reflected by the target and then attenuated by the atmosphere.
- The atmospheric path radiance,  $L_{p \rightarrow 0}(r, \theta, \lambda)$ , i.e. thermal emission of the air in the direction from the target towards the camera.

From a phenomenological view, which takes cognizance of the above mentioned contributions, the following measurement equation can be constructed for broadband infrared camera recordings at a specific altitude:



$$\begin{aligned}
 L_{irg}^{meas}(r, \theta) = & \underbrace{\int_{\lambda_1}^{\lambda_2} L_{irg}(\lambda) \tau_{atm}(r, \theta, \lambda) \tau_{sens}(\lambda) d\lambda}_{T_1: \text{Target thermal emission}} \\
 & + \underbrace{\int_{\lambda_1}^{\lambda_2} L_{bkg}(r, \theta, \lambda) \tau_{irg}(\lambda) \tau_{atm}(r, \theta, \lambda) \tau_{sens}(\lambda) d\lambda}_{T_2: \text{Background emission through target}} \\
 & + \underbrace{\int_{\lambda_1}^{\lambda_2} L_{env}(r, \theta, \lambda) \rho_{irg}(\lambda) \tau_{atm}(r, \theta, \lambda) \tau_{sens}(\lambda) d\lambda}_{T_3: \text{Environmental emission reflected from target}} \\
 & + \underbrace{\int_{\lambda_1}^{\lambda_2} L_{p_{r \rightarrow 0}}(r, \theta, \lambda) \tau_{sens}(\lambda) d\lambda}_{T_4: \text{Atmospheric path radiance}}
 \end{aligned} \quad (1)$$

where  $L_{irg}^{meas}(r, \theta)$  [ $\text{W} \cdot \text{m}^{-2} \cdot \text{sr}^{-1}$ ] is the measured radiance as observed by a single detector element (pixel) within a staring array camera like the Cedip, of a target at a distance  $r$  and elevation angle  $\theta$ . If the target dimensions are small in comparison with  $r$ , the same values of  $r$  and  $\theta$  can be associated with each pixel of the target for a specific recorded image. The spectral transmittance of the atmosphere is represented by  $\tau_{atm}(r, \theta, \lambda)$ ; the camera sensor's spectral response normalized with respect to the maximum response value within the infrared band of concern is represented by  $\tau_{sens}(\lambda)$ ; the spectral transmittance through the target is given by  $\tau_{irg}(\lambda)$ ; and the spectral reflectivity of the target is noted by  $\rho_{irg}(\lambda)$ . The functional dependence of the measured radiance on  $r$  and  $\theta$  arises due to the atmospheric transmission and emission, which changes as a function of these two parameters. For different altitudes of the observing camera, this dependence will differ.

The environmental radiance,  $L_{env}(r, \theta, \lambda)$ , includes the spectral radiance from every object that emits energy in such a manner that it is reflected by the target towards the camera. Included in  $L_{env}(r, \theta, \lambda)$  is the atmospheric (path) radiance of the target's surrounding atmosphere,  $L_{p_{\infty \rightarrow r}}(\lambda)$ , i.e.

$$L_{env}(r, \theta, \lambda) = L_{p_{\infty \rightarrow r}}(\lambda) + L_{env}^{other}(\lambda), \quad (2)$$

where  $L_{env}^{other}$  represents all environmental sources except  $L_{p_{\infty \rightarrow r}}(\lambda)$ . If it is assumed that the atmospheric path radiance incident on the target surface is isotropic, then the irradiance on the target can be calculated as  $E_{irg} = L_{p_{\infty \rightarrow r}} \Omega_p = L_{p_{\infty \rightarrow r}} \pi$ , where  $\Omega_p$  is the projected solid angle subtended by the environmental radiance. The reflected radiance would then be  $\frac{E_{irg} \rho}{\pi} = L_{p_{\infty \rightarrow r}} \rho$  if the target surface is Lambertian. The specifics of (2), however, depends on the specific measuring setup – for an aircraft, for example, a terrain model should

ideally be included in the determination of  $L_{env}$  under the  $L_{env}^{other}$  term in order to determine the earthshine reflections. This is, however, seldom done due to the enormous complexity involved.

The desired parameter in (1) is the absolute target radiance,  $L_{irg}(\lambda)$ , which can only be obtained if at least the following parameters are known:  $\tau_{irg}(\lambda)$ ,  $\rho_{irg}(\lambda)$ ,  $\tau_{atm}(r, \theta, \lambda)$ ,  $\tau_{sens}(\lambda)$ ,  $L_{env}(r, \theta, \lambda)$ ,  $L_{p_{r \rightarrow 0}}(r, \theta, \lambda)$ ,  $L_{bkg}(r, \theta, \lambda)$  and the measured value  $L_{irg}^{meas}(r, \theta)$  itself. Fortunately, the existence of advanced software for atmospheric remote sensing like PeModWin©, which uses the program Modtran, enables the computation of atmospheric transmission and path radiance from the ultraviolet into the infrared and microwave regions of the electromagnetic spectrum [2]. Thus, if no measurements are available of  $L_{bkg}(r, \theta, \lambda)$  for the case of a clear sky background, or of  $L_{p_{r \rightarrow 0}}(r, \theta, \lambda)$ ,  $L_{p_{\infty \rightarrow r}}(\lambda)$ , or  $\tau_{atm}(r, \theta, \lambda)$ , then this software can be used to compute reasonable estimates of these parameters.

The parameter  $\tau_{sens}(\lambda)$  is calculable from the spectral properties of all elements in the camera's optical path, typically being the lens transmittance taking into account any anti-reflection coating, any filter put in the optical path, the detector dewar window transmittance and the spectral response of the specific detector used. The spectral response can however also be measured with the aid of, for example, a blackbody and a continuous variable filter (cvf), which is an optical disk of which the passband is adjusted by the disk rotation angle [3].

The target property  $\tau_{irg}(\lambda)$  is applicable to a target, which is partially transparent, e.g. a gas or plasma volume like an aircraft plume or a specific type of window. The target property  $\rho_{irg}(\lambda)$  is typically applicable to a non-gaseous object, e.g. an aircraft fuselage painted with a certain type of paint associated with specific reflective properties. The reflectivity can be refined to include both specular and diffuse reflectivity. These target properties need to be known through measurements or through published literature.

Knowing the above mentioned parameters is however not enough to obtain a unique solution for  $L_{irg}(\lambda)$ , since various shapes of the target radiance spectrum can lead to an agreement between the left and right hand sides of (1). In the pursuit of a distinctive  $L_{irg}(\lambda)$  spectrum, the definition of emissivity can be employed so that the target radiance spectrum can be rewritten as

$$L_{irg}(\lambda) = L_{BB}(\lambda, T_{irg}) \cdot \epsilon_{irg}(\lambda), \quad (3)$$

where  $L_{BB}(\lambda, T)$  is the spectral radiance from a blackbody (Planck) radiator at temperature  $T_{irg}$  and  $\epsilon_{irg}(\lambda)$  is the emissivity of the target. If  $\epsilon_{irg}(\lambda)$  is known, then  $T_{irg}$  for the target can be calculated by means of a numerical method so that (1) is satisfied. The numerical method employed can be very simple since the value of term  $T_1$  on the right hand side

of (1) increases monotonically as the value of  $T_{irg}$  increases, thus also leading to a unique solution of  $T_{irg}$ .

The unfortunate reality surrounding the prerequisite of knowledge about  $\varepsilon_{irg}(\lambda)$ ,  $\tau_{irg}(\lambda)$  and  $\rho_{irg}(\lambda)$ , is that *partial information about the target is required in order to obtain the absolute target radiance*. Although inconvenient, there is no way around this – at least two of these three target parameters need to be known as implied by the principle of conservation of energy which relate these three quantities by

$$\varepsilon_{irg}(\lambda) + \tau_{irg}(\lambda) + \rho_{irg}(\lambda) = 1. \quad (4)$$

Another method, other than using a numerical scheme to solve the target radiance spectrum in (1), is to isolate  $L_{irg}(\lambda)$  in term  $T_1$  by replacing this term with

$$\langle \tau_{sens}(\lambda) \tau_{atm}(r, \theta, \lambda) \rangle \cdot \int_{\lambda_1}^{\lambda_2} L_{irg}(\lambda) d\lambda, \quad (5)$$

where

$$\begin{aligned} \langle \tau_{sens}(\lambda) \tau_{atm}(r, \theta, \lambda) \rangle &\equiv \frac{\int_{\lambda_1}^{\lambda_2} L_{irg}(\lambda) \tau_{atm}(r, \theta, \lambda) \tau_{sens}(\lambda) d\lambda}{\int_{\lambda_1}^{\lambda_2} L_{irg}(\lambda) d\lambda} \\ &= \frac{\int_{\lambda_1}^{\lambda_2} l_{irg}(\lambda) \tau_{atm}(r, \theta, \lambda) \tau_{sens}(\lambda) d\lambda}{\int_{\lambda_1}^{\lambda_2} l_{irg}(\lambda) d\lambda} \end{aligned} \quad (6)$$

is the average of the product  $\tau_{sens}(\lambda) \tau_{atm}(r, \theta, \lambda)$  weighted by the target radiance spectrum<sup>1</sup>. The normalized target spectrum is

$$l_{irg}(\lambda) \equiv \frac{L_{irg}(\lambda)}{L_{irg}(\lambda_m)}, \quad (7)$$

where  $\lambda_m$  is the value of  $\lambda$  for which  $L_{irg}(\lambda)$  is a maximum. Equation (6) is mathematically still identical to the original term  $T_1$  in (1).

Equation (1) can now be rewritten as

$$L_{\lambda_1 \rightarrow \lambda_2} \equiv \int_{\lambda_1}^{\lambda_2} L_{irg}(\lambda) d\lambda = \frac{L_{irg}^{meas} - T_2 - T_3 - T_4}{\langle \tau_{sens}(\lambda) \tau_{atm}(r, \theta, \lambda) \rangle}, \quad (8)$$

where shorthand notation is used in referring to the terms in (1). This equation can be called the data reduction equation.

<sup>1</sup> Use is made of definition and notation of weighted mean as described by Terr, David, “Weighted Mean”, from *Mathworld* – A Wolfram Web Resource, created by Eric W. Weisstein, <http://mathworld.wolfram.com/WeightedMean.html>

The required target information that enables data reduction of the target object as modelled by the influences stated in (1), either by a numerical scheme or by the procedure leading to (8), is labelled as subsets A – D in Table I. If the information regarding the target is insufficient, i.e. the information falls into subsets E – H of Table I, then assumptions regarding  $\tau_{irg}(\lambda)$ ,  $\rho_{irg}(\lambda)$  and  $\varepsilon_{irg}(\lambda)$  need to be made in order to obtain absolute target radiance values.

For the trivial case of subsets A, B and C of known target parameters, no data reduction is necessary since the required parameters are known and  $L_{irg}(\lambda)$  can be calculated from (3). For subset C, the value of  $T_{irg}$  can be obtained by inferring the peak value of the normalized blackbody spectrum  $l_{irg}(\lambda)/\varepsilon_{irg}(\lambda)$  and relating that to the target temperature according to the Wien displacement law (consult e.g. [4]).

For subset D, the numerical solution scheme can be employed in order to obtain a unique  $T_{irg}$ , which then also enables  $L_{irg}(\lambda)$  to be calculated according to (3).

TABLE I. TARGET INFORMATION REQUIRED FOR DATA REDUCTION

Parameter	Sufficient				Insufficient			
	✓	✗	✓	✗	✓	✓	✗	✗
$l_{irg}(\lambda)$	✓	✗	✓	✗	✓	✓	✗	✗
$T_{irg}$	✓	✓	✗	✗	✓	✗	✓	✗
$\tau_{irg}(\lambda)$ & $\rho_{irg}(\lambda)$ & $\varepsilon_{irg}(\lambda)$	✓	✓	✓	✓	✗	✗	✗	✗
Subset of target parameters	A	B	C	D*	E	F	G	H

\*Only sufficient in the case of a numerical solution scheme.

In (8),  $L_{\lambda_1 \rightarrow \lambda_2}$  refers to the radiance of only the part of the target object as could be observed in the field of view (FOV) of a pixel of the infrared camera. The intensity takes the whole target object, when resolved in the infrared image, into account according to

$$\begin{aligned} I_{irg} &= \sum_{pixels} A_{irg}^{FOV} \cdot L_{\lambda_1 \rightarrow \lambda_2}(pixel) \\ &= A_{irg}^{FOV} \sum_{pixels} L_{\lambda_1 \rightarrow \lambda_2}(pixel) \quad . \quad (9) \\ &= A_{irg}^{total} \cdot \bar{L}_{\lambda_1 \rightarrow \lambda_2}(pixel) \end{aligned}$$

In this equation,  $I_{irg}$  [W.sr<sup>-1</sup>] is the intensity of the target object as a whole at the aspect angle as observed from the position of the camera;  $A_{irg}^{FOV}$  is the projected area of the target object filling the pixel FOV;  $A_{irg}^{total}$  is the total projected area of the target object;  $L_{\lambda_1 \rightarrow \lambda_2}(pixel)$  is the radiance as defined in (8), but with explicit reference to the fact that it is pixel dependent; and  $\bar{L}_{\lambda_1 \rightarrow \lambda_2}(pixel)$  is the average radiance of all the pixels covering the target object.



### B. Application of Theory to Aircraft Plume

In applying the data reduction technique to the aircraft plume recorded during the mentioned flight test, term  $T_3$  in (1) and (8) was set to zero, since it can be assumed that no environmental reflection from a plume occurs. Information regarding the atmospheric parameters, i.e.  $\tau_{atm}(r, \theta, \lambda)$ ,  $L_{p_{r \rightarrow 0}}(r, \theta, \lambda)$  and a clear sky background  $L_{bkg}(r, \theta, \lambda)$ , was obtained by using the Modtran 4.0 software. The recorded meteorological profiles were compared to the generic model atmospheres of Modtran and a sufficient agreement was observed with the Mid-Latitude Summer (MLS) atmosphere, which was subsequently used.

A response measurement of the Cedip camera was used in the specification of the camera response spectrum,  $\tau_{sens}(\lambda)$ . The target emissivity spectrum,  $\epsilon_{irg}(\lambda)$ , as measured at a specific position in the plume during a previous ground test was used. From this, the plume transmittance could also be obtained through  $\tau_{irg}(\lambda) = 1 - \epsilon_{irg}(\lambda)$ .

This target emissivity spectrum will differ from in situ measurements, as well from one position to another in the plume (i.e. from pixel to pixel in the image). For a turbojet engine at a fixed engine setting, the plume intensity is proportional to the fuel consumption of the aircraft, which in turn decreases with increasing altitude. The denser plume at lower altitudes is expected to have higher emissivity values. Also, when observing at a specific aspect angle (at any altitude), the thicker middle part of the plume (i.e. for sight line going through plume centerline) is expected to have a higher emissivity than the thinner outer layer observed near the plume's edge. This spatial dependence of  $\epsilon_{irg}(\lambda)$  is not taken into account during data reduction, and therefore the value of  $T_{irg}$  that will be obtained during a numerical solution of (1) will not be equally accurate at all spatial positions. It was therefore decided to follow the simpler data reduction procedure as prescribed by (8) and (3), using the mentioned emissivity spectrum, but also using an estimated single value of  $T_{irg}$  for all plume pixels. It fortunately so happens that

$$\langle \tau_{sens}(\lambda) \tau_{atm}(r, \theta, \lambda) \rangle = \frac{\int_{\lambda_1}^{\lambda_2} L_{BB}(\lambda, T_{irg}) \epsilon_{irg}(\lambda) \tau_{atm}(r, \theta, \lambda) \tau_{sens}(\lambda) d\lambda}{\int_{\lambda_1}^{\lambda_2} L_{BB}(\lambda, T_{irg}) \epsilon_{irg}(\lambda) d\lambda}, \quad (10)$$

as it is now used in (8), is not strongly dependent on the value of  $T_{irg}$ . As an example – for a MLS atmosphere, at an altitude of 3049 m and an elevation angle of  $0^\circ$  over the typical camera-target aircraft distance of 100 m, the quantity in (10) varies only from 0.317 to 0.347 when calculated for temperatures covering a span of  $500^\circ\text{C}$ , i.e. with  $T_{irg}$  ranging from  $300^\circ\text{C}$  to  $800^\circ\text{C}$ . A guesstimate of  $T_{irg}$  in the order of  $100^\circ\text{C}$  from the correct value should probably suffice. For the data reduction, a value of  $530^\circ\text{C}$  was used as this is the typical value of the Jet Pipe Temperature (JPT) measured inside the jet pipe of the turbine engine, where the plume originates, while in flight at a 100% dry engine setting.

In the practical execution of the data reduction, lookup tables were created in which the required atmospheric properties could be obtained for a given camera-target distance and elevation angle. This resulted in speedier processing of each of the set of frames recorded during each leg of the racecourse track flow.

After the absolute radiance plume images were obtained, further analyses related to the plume characteristics were possible as described in Section IV.

### IV. MEASUREMENTS AND DATA REDUCTION RESULTS

Fig. 3 shows examples of the unprocessed image recordings made at 3049 m (10 kft) at the aspect angles of  $20^\circ$  and  $90^\circ$  respectively. In these grey scale images, the lighter shades represent relatively high radiance values, while the darker shades represent lower radiance values. It can clearly be seen how the plume becomes increasingly obscured by the aircraft's cooler fuselage as the aspect angle decreases.

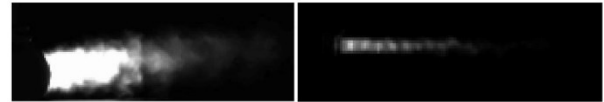


Figure 3. Example recordings from the MWIR camera of the target aircraft at  $20^\circ$  and  $90^\circ$  aspect angles respectively.

Fig. 4 is another captured image of the target aircraft in false colours, where the colours are, in order of increasing absolute radiance values as obtained through the data reduction procedure – black, blue, green, orange and red/pink.

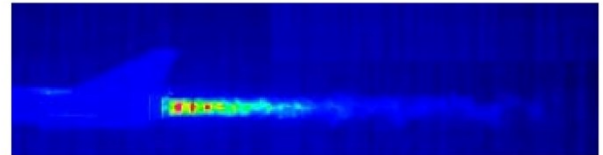


Figure 4. Recording of the MWIR camera at 3049 (10 kft) of the target aircraft at a  $90^\circ$  aspect angle. The Mach discs are clearly visible as high radiance areas in the plume.

Further analysis of this plume included the determination of the radiance length profiles at the positions along the horizontal black line in the image, and of the radiance width profiles at the positions indicated by the black vertical lines, similar to that indicated in Figure 5.

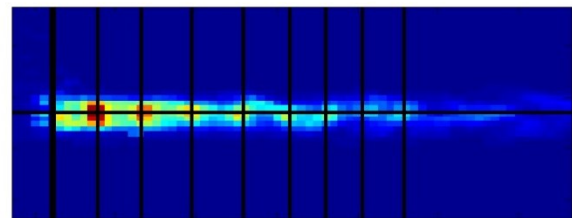


Figure 5. Positions of length and width radiance profiles through the plume are indicated by the black lines.



The average length and width profiles of the plume at a 90° aspect angle were determined from a number of recordings over different altitudes. The average length profiles are shown in Fig. 6. It can be seen that these plume profiles decrease over their entire length as the altitude increases. The difference in the width profiles of the plume was also determined as a function of altitude as well as position in the plume behind the start of the plume. As an example, Fig. 7 shows normalized plume width profiles at an altitude of 900 m (3 kft). It can be seen that the peak value of these profiles decrease as the distance between the start of the plume and the vertical profile position increase. These profiles capture the shape and radiance distribution of the plume as a function of altitude.

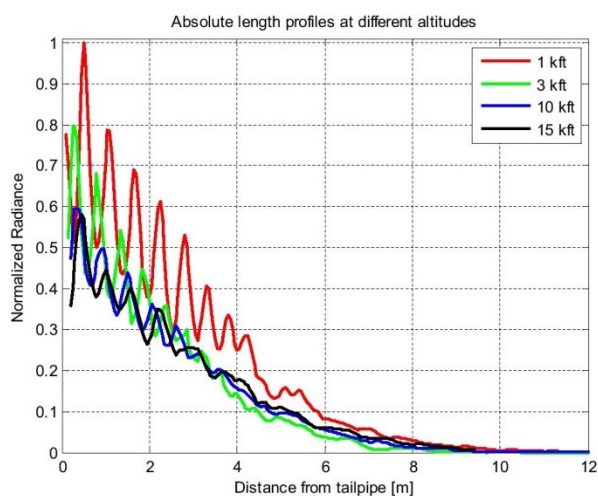


Figure 6. Average length profiles through the plume of absolute radiance as determined at different altitudes.

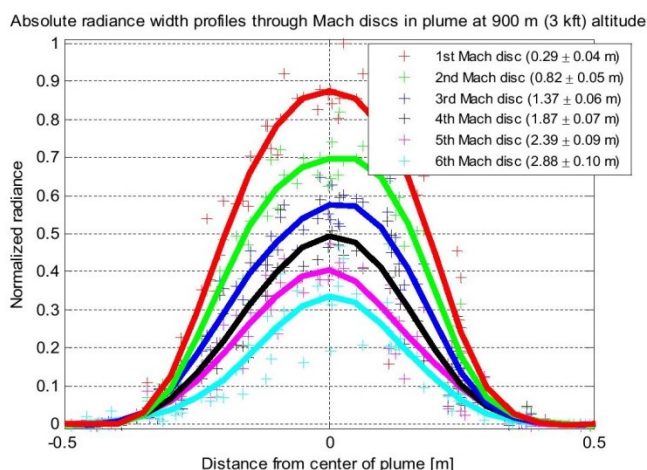


Figure 7. Average width profiles through the plume of absolute radiance at an altitude of 900 m at positions situated at different distances from the start of the plume.

In Fig. 8 the plume intensity at is shown as a function of the aspect angle from which the aircraft is observed. The shape of the intensity curve at small aspect angles depends on the specific geometry of the aircraft obscuring the plume. At a 90° aspect angle, no obscuration takes place.

Besides the above illustrated results, the absolute plume radiances and intensities were also used in determining other characteristics of concern, e.g. the dependence of the plume's intensity and area on altitude.

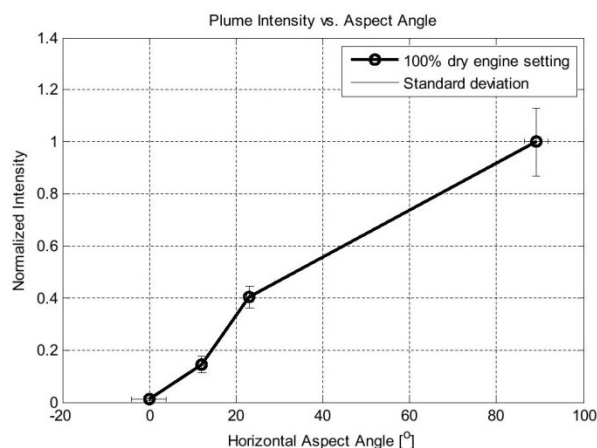


Figure 8. Plume intensity as a function of aspect angle. At bigger angles, the plume obscuration by the fuselage is less and the plume intensity therefore larger.

## V. CONCLUSION

The MWIR data acquired during the flight test using the pod, processed in the manner outlined in this article, allows one to construct a relatively accurate characterization of an aircraft plume. Although a complete set of spatially dependent emissivity data was lacking, useable radiance and intensity values could nevertheless still be obtained. This characterization of the aircraft plume allows the construction of a radiometrically accurate computer model, which can be used in simulation for the programming of infrared seekerhead missiles [5].

## REFERENCES

- [1] Alacron, [Web site accessed on 2011-02-21], <http://alacron.com/clientuploads/directory/Cameras/CEDIP/jadealtair.pdf>
- [2] K. Tang, C. Tibaudo, J. Schroeder, "Advanced software products for atmospheric remote sensing", Targets and Backgrounds IX: Characterization and Representation, Proceedings of SPIE Vol. 5075, 2003, p. 293–299.
- [3] M. D. Mermelstein, K.A. Snail, R. G. Priest, "Spectral and Radiometric calibration of midwave and longwave infrared cameras", Optical Engineering Vol. 39 No. 2, February 2000, p. 347-352.
- [4] J. M. Palmer, B. G. Grant, The art of radiometry, SPIE Press, Bellingham, Washington USA, 2010, pp.86–87.
- [5] M. S. Willers, J. S. H. van den Bergh, "Optronics sensor development using an imaging simulation system", as submitted to: Saudi International Electronics, Communications and Photonics Conference (SIEPC), 2011.

### **4.3 PUBLICATION – MEASUREMENTS OF A MICRO GAS TURBINE PLUME AND DATA REDUCTION FOR THE PURPOSE OF INFRARED SIGNATURE MODELING**

The set-up of the measurements and the data reduction thereof, as reported in this publication, were planned, coordinated and supervised by the present author. This work formed part of an almost one-year infrared radiometry course presented at Denel Dynamics to a contingent of Brazilian scientists and engineers in the missile development industry. It was estimated by the principal author (F. Sircilli) of the publication that the present author's contribution to the article was at least 40%. This publication was preceded by a conference proceedings publication [18], after which this more detailed version was published in a peer-reviewed journal. Relevance of the publication to other researchers can be deduced from a reference made to [18] in a peer-reviewed journal article [16], which followed a similar experiment.

The article was published in the journal IEEE Transactions on Aerospace and Electronic Systems [4].

# Measurements of a Micro Gas Turbine Plume and Data Reduction for the Purpose of Infrared Signature Modeling

**FRANCISCO SIRCILLI**, Member, IEEE  
Institute for Advanced Studies (IEAv)  
São Paulo, Brazil

**STEPHANUS J. P. RETIEF**  
University of Pretoria  
Hatfield, South Africa  
and  
Denel Dynamics  
Centurion, South Africa

**LUCIANO B. MAGALHÃES**  
Comando Geral de Operações Aéreas (COMGAR)  
Brasília-DF, Brazil

**LUTY R. RIBEIRO**  
Aeronautics and Space Institute (IAE)  
São José dos Campos-SP, Brazil

**ADEMILSON ZANANDREA**  
Avibrás S.A.  
São José dos Campos, Brazil

**CORNELIS BRINK**  
Denel Dynamics  
Pretoria, South Africa

**MAIKON NASCIMENTO**  
Edmonton, Canada

**MARIA M. DREYER**  
Denel Dynamics  
Pretoria, South Africa

Manuscript received May 21, 2014; revised December 12, 2014; released for publication March 23, 2015.

DOI: No. 10.1109/TAES.2015.140392.

Refereeing of this contribution was handled by H. Kwon.

Authors' addresses: F. Sircilli, Institute for Advanced Studies (IEAv), EFA-E, Trevo Cel A. Amarante n.1, São José dos Campos, São Paulo 12228-001, Brazil, E-mail: (sircilli@ieav.cta.br); S. J. P. Retief, the Department of Physics, University of Pretoria, and also Denel Dynamics, P.O. Box 7412, Centurion, 0046 Gauteng, South Africa; L. B. Magalhães, Comando Geral de Operações Aéreas (COMGAR), SHIS QI 5-Área Especial 12, Lago Sul, 71615-600, Brasília-DF, Brazil; L. R. Ribeiro, Aeronautics and Space Institute (IAE), Praça Mal. Eduardo Gomes, 50 - Vila das Acácias, 12.228-904, São José dos Campos-SP, Brazil; A. Zanandrea, Avibrás S.A., Estrada Varadouro, 1200, 12315-020, Jacareí-SP, Brazil; C. Brink, M. M. Dreyer, Denel Dynamics, P.O. Box 7412, Centurion, 0046 Gauteng, Pretoria, South Africa; M. Nascimento, 11447-79 Ave, Edmonton, T6G 0P5 Canada.

0018-9251/15/\$26.00 © 2015 IEEE

An important issue concerning numerical simulation of gas turbine-propelled aircraft in infrared scenarios (usually in military applications) is the radiometric emission properties of the aircraft exhaust plume. In this paper, a detailed description of the experimental setup and the measurement results of the infrared signature properties of a micro turbine engine plume at ground level (with an altitude of approximately 1500 m above sea level) are presented. The main instruments used were a midwave (3–6  $\mu\text{m}$ ) infrared camera and a spectroradiometer (0.8–5.5  $\mu\text{m}$ ). The wideband emission properties were investigated with the camera as a function of the aspect angle between the camera's field of view and the plume's longitudinal axis, while maintaining a fixed engine rotational speed, as well as a function of the engine rotational speed for a fixed aspect angle of 90°. The spectral emission was investigated with the spectroradiometer as a function of three regions along the plume for a small instrument field of view and fixed engine setting. These measurements comprise the radiometric characterization of a micro gas turbine exhaust plume that, after data reduction, allows numerical modeling of this type of plume in a computer simulation. Such measurements, or the model based on it, are useful in conceptual studies regarding the infrared signatures of a turbine gas plume. It is in principle also possible to construct an infrared radiometric model of a larger-scale turbine engine's plume based on these characteristics.

## I. INTRODUCTION

Field experiments are expensive and provide limited information against the numerous possible scenarios in which an infrared (IR) system, like an IR missile, must operate [1]. The use of simulation software allows for virtual experimentation, while probably reducing safety risks, lowering financial costs, and shortening the timescales of system development [2]. During virtual experimentation, an almost limitless number of system configurations and scenario setups can be simulated so that a thorough statistical picture of expected system performance can be provided. Moreover, a modeling and simulation approach requires a deep understanding of the physics and engineering phenomena involved, which result in a solid opportunity of both refinement and improvement of the IR device.

Input data for this kind of software includes the IR device model, as well as the geometric and IR radiometric properties of all scene elements involved, such as their shapes, sizes, distances, radiances, and intensities, including a sufficiently accurate terrain background. Important contributors toward the IR signature of a gas turbine-propelled aircraft, like a typical fighter aircraft, are its exhaust plume and engine tailpipe (nozzle) radiances; these sources are important in the aircraft's side and rear aspect signatures, respectively [3, 4].

This work presents the measured radiometric plume properties of a commercial micro turbine engine's exhaust plume at ground level (with an altitude of approximately 1500 m above sea level). These properties are necessary for plume characterization, which is required for IR signature modeling. This work complements the evaluated radiometric properties published elsewhere [5, 6].

Although this engine is normally intended to thrust radio-controlled airplane models and not for use in full-scale manned aircraft, the goal of this paper is to show



the methods required for IR plume signature measurements and the data reduction thereof, which can similarly be applied to a larger-scale aircraft plume. However, much can be learned from these measurements, because the plume temperatures of a larger-scale aircraft or unmanned aerial vehicle (UAV) cover the same range as that of a micro turbine's plume, as can be gathered from [7] and the measured values stated later in this article. Moreover, the fuel (Jet A-1) used by real aircraft is the same fuel used by this micro turbine, and the basic combustion process is the same [6]. It is therefore of value to take the radiometric characteristics obtained from the micro turbine plume into account when constructing a larger-scale aircraft or UAV plume model, because a basic gas turbine plume must qualitatively adhere to these characteristics.

One big advantage is that an elaborate set of measurements is orders of magnitude more cost effective and easier to achieve for a micro turbine plume than for a real aircraft plume. This makes various conceptual studies related to IR signatures of plumes possible—e.g., in the development of autonomous plume identification and tracking algorithms applied to IR measurements [6].

The midwavelength infrared (MWIR) band is considered the most prominent wavelength band regarding plume observations [6, 8], and the measurements were done within this band as described in Section II of this paper. All radiometric data so obtained was submitted to a data reduction process, described in Section III, and the results after data reduction, with a discussion thereof, are given in Section IV. These results are to be used to create a computerized mathematical model, which will be implemented in existing in-house IR scenario simulation software. Conclusions, related to the previously mentioned goals, are supplied in Section V.

## II. EXPERIMENTAL SETUP

The basic instrumentation available and appropriated for the plume measurements was as follows: 1) a Cedip Jade III MWIR camera with a resolution of  $320 \times 240$  pixels and operating in the  $3.6\text{-}5.1\text{-}\mu\text{m}$  spectral range, and 2) a Fourier transform infrared (FTIR) Bomem MR 200 spectroradiometer (SR) used at a spectral resolution of  $4\text{ cm}^{-1}$  and operating in the  $0.8\text{-}5.5\text{-}\mu\text{m}$  spectral range. Complementary instrumentation, such as a portable weather station, an extended area blackbody, an Inter-Range Instrumentation Group B time synchronizer, and a global positioning system (GPS) antenna, were also deployed.

The radiometric properties of the micro turbine plume were evaluated by means of three measurement sessions during which a specific parameter of interest was adjusted: 1) the turbine rotational speed, expressed as the number of rotations per minute (RPM), was varied for a fixed aspect angle (AA) of  $90^\circ$  between the MWIR camera's field of view (FOV) and the longitudinal axis of the turbine plume (called the RPM scan session in this paper); 2) the AA was

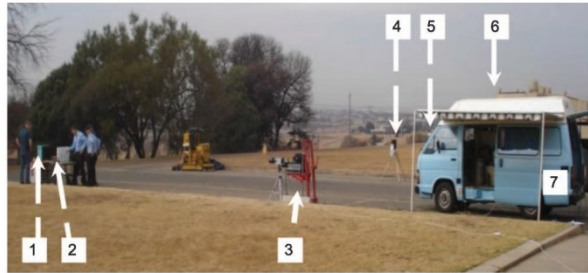


Fig. 1. Side view of measurement setup for small FOV session, where 1 refers to blackbody, 2 refers to engine, 3 refers to position of both MWIR camera and SR for small FOV sessions of measurements, 4 refers to weather station, 5 refers to GPS, 6 refers to mobile lab, and 7 refers to MWIR camera position for both RPM and AA sessions.

varied for a fixed turbine RPM (called the AA scan session in this paper); and, 3) three positions along the plume were observed within a small SR FOV for a fixed RPM at a full thrust engine setting and  $90^\circ$  AA (called the small FOV session in this paper). The goals of these measurement sets were to determine 1) the effect of engine speed on plume intensity, 2) the effect of AA on plume intensity, 3) the spectral radiance content of the plume, and 4) an emissivity function, representative of the whole plume, from the spectral radiance.

The engine was mounted on a bench, which allowed the adjustment of the AA in the AA scan session of measurements, as well as the secure control of the engine rotational speed during the measurements. Fig. 1 is a photo of the setup used to measure the engine plume for the specific case of the small FOV session. Indicated from the left to right are the blackbody and table with the turbine engine, the positions of MWIR camera and SR, the portable weather station, the GPS antenna used to synchronize the instrument control computers' time, and the mobile lab, which accommodates the computers and other accessories. The distance between the devices of measurement and the turbine was 20 m in the case of both RPM and AA sessions and 11 m in the case of the small FOV measurements.

The MWIR camera and SR were calibrated before the start of the measurements using the blackbody. This was done in the standard fashion, as prescribed by the manufacturers, by sweeping the blackbody through a range of temperatures and recording its radiance at each temperature as soon as it stabilized. The camera was switched on for approximately 1 h before measurements were done for its internal temperature to stabilize.

The engine used in all three measurement sessions was a commercial Kingtech K80 micro turbine engine (with a thrust of 80 N) mounted on a wooden board, with all components needed to start and control the performance of the turbine, as shown in Fig. 2. Sensor feedback obtained from the display unit of the turbine control system included the turbine RPM, an indication of fuel consumption (relative pump power in digital levels), and



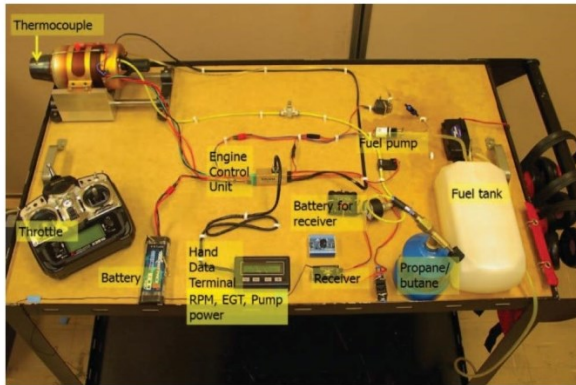


Fig. 2. Engine setup: fuel tank, propane/butane gas cylinder, turbine (upper-left side), thermocouple measuring EGT through hole in nozzle, data terminal, FADEC auto starter (engine control unit), solenoid valves, batteries, actuators, etc.

the exhaust gas temperature (EGT) measured by the factory-mounted thermocouple inside the tailpipe.

The engine was started by an injection of a butane/propane gas mixture (typically 40/60) into the turbine until a stable flame was obtained, followed by the injection of liquid fuel (Jet A-1 with 5% of lubricant additive). When the rotation speed reached about 25 000 RPM, the injection of gas was interchanged with that of the Jet A-1 fuel; the rotation speed was then further increased until the desired rotation speed was obtained. The control of the turbine RPM could be done by two means—a radio remote control, the option used in all measurements, or manually by varying the electrical signal to be sent to the Full Authority Digital Engine Control (FADEC) auto starter.

Because the plume signal is prominent only in the MWIR band [8], a camera sensitive in the short wavelength infrared (SWIR) range was not deployed. The SWIR signal only overcomes the atmospheric attenuation when the plume gas density is so high that the transmittance goes to zero and the emissivity ( $\epsilon = 1 - \tau$ ) tends to one—then the plume acts like a blackbody. This occurs in the thrust afterburner stage of an aircraft engine [6, 7].

The SR has two channels—channel A (Ge detector), operating in the 0.91- to 1.72- $\mu\text{m}$  spectral range, and channel B (InSb detector), operating in the 0.83- to 5.5- $\mu\text{m}$  range. For the same reason that the SWIR camera was not used, only the InSb detector was used in SR measurements. To synchronize all instrument recordings, a Masterclock TCR1000 connected to the GPS external antenna was connected to all instrument control computers.

For the RPM scan session, only the MWIR camera (InSb detector) was used to determine the IR emission of the micro turbine plume at different engine settings. Preparatory measurements with the SR indicated that the intensity at engine settings lower than the maximum RPM

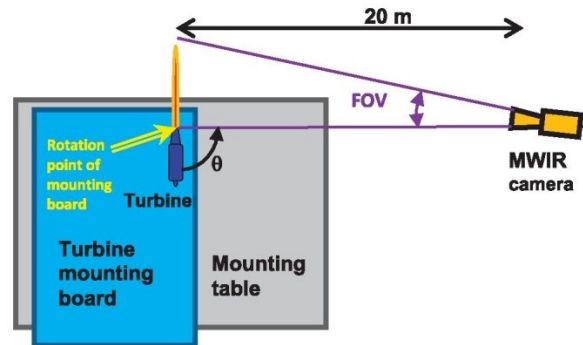


Fig. 3. Plan view diagram of RPM scan and AA scan measurement sessions.



Fig. 4. View from MWIR camera position for AAs of 135° (left) and 180° (right) as used in AA scan session.

setting resulted in poor, noisy recordings; therefore, this instrument was not used during the RPM session. Fig. 3 represents the setup for this session in which the turbine was maintained at  $\theta = 90^\circ$  AA (the angle between the MWIR camera line of sight and the plume longitudinal axis). The distance between the MWIR camera and the engine was 20 m, and it was used without any filter and with a 200-mm ( $f$ -number of 2) lens for the plume to fill the MWIR FOV of  $2.8^\circ \times 2.1^\circ$ . The measurements were done for 30-, 240-, and 2800- $\mu\text{s}$  integration times. Besides the MWIR images, notes of the actual RPM, relative pump power, and temperature values of the engine during the recordings were also taken. The initially intended engine rotation values in RPM units were 45 000, 60 000, 80 000, 100 000, 110 000, 120 000, 125 000, 130 000, 135 000, 140 000, and 145 000.

In the AA scan session, only the MWIR camera was used to determine the IR emission of the micro turbine plume at different aspects angles, as showed in Fig. 3. The AA  $\theta$  was varied for angles of  $0^\circ$ ,  $30^\circ$ ,  $45^\circ$ ,  $60^\circ$ ,  $70^\circ$ ,  $90^\circ$ ,  $110^\circ$ ,  $120^\circ$ ,  $135^\circ$ ,  $150^\circ$ , and  $180^\circ$ . Measurement of the plume at most of these angles with the SR proved impractical because of the relatively small size of the projected plume areas—a larger turbine engine would be more appropriate for such measurements. In Fig. 4, it is possible to see close-up photos of the MWIR camera view for two AAs. The measurements were done without any neutral density filter (NDF), with the intention of obtaining the plume radiation. For measurements of the



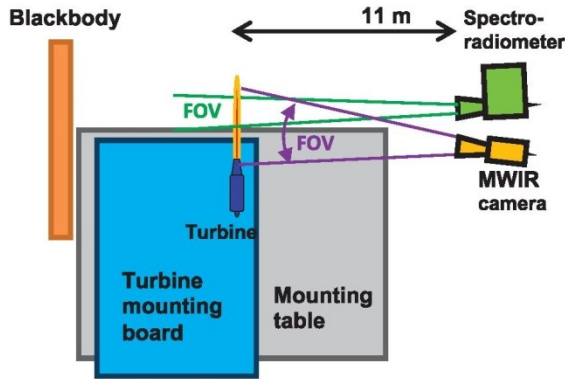


Fig. 5. Plan view diagram of small FOV setup.

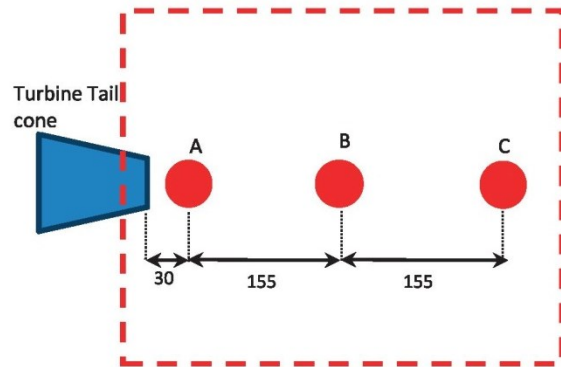


Fig. 6. Diagram used to adjust SR FOV. Red circular regions A, B, and C and red dashed rectangular region correspond approximately to SR and MWIR FOV footprint, respectively. Dimensions are in millimeters.

tailpipe, a NDF must be added to avoid saturation of the pixel detectors.

For the small FOV session, the MWIR camera and the SR were positioned as close as possible to each other, as showed in Fig. 5. The goal of this session was to measure the radiance and transmission of the plume and therewith determine the emissivity at three positions of the plume. To have a source for the transmission measurements, the extended area (30 × 30 cm) blackbody at 300°C and a polystyrene board were used, always alternating one of these as the background of the plume. Two additional measurements were also made of only the blackbody and only the polystyrene, i.e., with no plume in front (turbine not running). The plume was measured with each type of background for a duration of 5 s. The blackbody was positioned at a shorter distance of 11 m from the MWIR camera and SR to obtain a sufficiently strong signal from the SR (average of 10 scans per measurement), while the polystyrene was temporarily inserted halfway between the blackbody and the turbine (at a safe distance from the turbine and the blackbody to avoid melting the polystyrene). In this session, the MWIR camera was again configured with a 200-mm lens, while the SR was configured with a 3.5-mrad (0.2°) FOV.

Figs. 6 and 7 show a side-view diagram and a close-up picture of the mounted table, respectively, indicating the three positions where radiometric parameters were measured: the central points are 30, 185, and 340 mm from the border of the tailpipe for the named points A, B, and C, respectively. The SR's projected FOV diameter at the plume position was 35 mm for the three cases. The measurements were processed to remove unwanted influences of the atmosphere and instrument on the recorded values. This data reduction process is described in the next section.

### III. DATA REDUCTION

Contributions to the IR signal observed by instrumentation when horizontally directed toward a target



Fig. 7. Close-up of mask used as reference to adjust three FOV positions of SR in small FOV session.

situated at a distance  $r$  usually consist of the following spectral sources (wavelength represented by  $\lambda$ ) [9]:

- The absolute target radiance  $L_{trg}(\lambda)$ , which can be represented by a blackbody radiator  $L_{BB}(\lambda, T)$ , which is the well-known Planck function at a specific temperature  $T$  and a specific emissivity associated with the target  $\varepsilon_{trg}(\lambda)$ , i.e.,  $L_{trg}(\lambda, T) = L_{BB}(\lambda, T) \cdot \varepsilon_{trg}(\lambda)$
- The background radiance  $L_{bkg}(r, \lambda)$  whenever the target is semitransparent
- The environmental foreground radiance  $L_{frg}(r, \lambda)$  as reflected against the target
- The atmospheric path radiance  $L_p(r, \lambda)$  for  $r \rightarrow 0$ , i.e., the thermal emission of the atmosphere (air) in the direction from the target toward the instrument

The radiance originating from the first three sources are attenuated by the atmosphere as it travels to the instruments. From a phenomenological point of view, taking cognizance of the previously mentioned contributions for the case of horizontal measurement through the atmosphere (i.e., homogeneous atmospheric attenuation and emission along the atmospheric path), the

following measurement equation can be constructed:

$$\begin{aligned}
 L^{meas}(r) = & \int_{\lambda_1}^{\lambda_2} L_{BB}(\lambda, T) \cdot \varepsilon_{IRg}(\lambda) \cdot \tau_{atm}(r, \lambda) \cdot \tau_{instr}(\lambda) d\lambda \\
 & + \int_{\lambda_1}^{\lambda_2} L_{bkg}(r, \lambda) \cdot \tau_{IRg}(\lambda) \cdot \tau_{atm}(r, \lambda) \cdot \tau_{instr}(\lambda) d\lambda \\
 & + \int_{\lambda_1}^{\lambda_2} L_{frrg}(r, \lambda) \cdot \rho_{IRg}(\lambda) \cdot \tau_{atm}(r, \lambda) \cdot \tau_{instr}(\lambda) d\lambda \\
 & + \int_{\lambda_1}^{\lambda_2} L_{Pr \rightarrow 0}(r, \lambda) \cdot \tau_{instr}(\lambda) d\lambda, \quad (1)
 \end{aligned}$$

where  $L^{meas}(r)$  is the measured radiance (in watts per steradian per square meter) of the target at a distance  $r$  as observed by a single detector element (pixel) within a staring array camera. Although the radiance of a given object at a given temperature stays constant over distance in vacuum, the functional dependence of the measured radiance on  $r$  arises because of the atmospheric transmission and emission, which change as a function of this parameter.

The terms on the right in (1) refer to the previously mentioned radiance of the target, the background emission through the target, the environmental emission reflected from the target, and the atmospheric path radiance, respectively. In these terms:

- The spectral transmittance of the atmosphere is represented by  $\tau_{atm}(r, \lambda)$ .
- The instrument's spectral response, normalized with respect to the maximum response value within the IR band of concern, is represented by  $\tau_{instr}(\lambda)$ . In a general form, considering the optical path through the instrument,

$$\tau_{instr}(\lambda) = \tau_{det}(\lambda) \cdot \tau_{ar}(\lambda) \cdot \tau_{lens}(\lambda) \cdot \tau_{dewar}(\lambda) \quad (2)$$

where  $\tau_{det}(\lambda)$  refers to the detector's spectral response and the remaining parameters refer to the spectral transmittances through the antireflection coating  $\tau_{ar}$ , through the lens  $\tau_{lens}$ , and through the dewar window of the detector  $\tau_{dewar}$ . This spectrum of  $\tau_{instr}(\lambda)$  is also used during calibration to calculate a radiance value

$\int_{\lambda_1}^{\lambda_2} L_{BB}(\lambda, T) \cdot \tau_{instr}(\lambda) d\lambda$  associated with each calibration temperature value of the blackbody.

- $\rho_{IRg}(\lambda)$  is the spectral reflectivity of the target.
- $\tau_{IRg}(\lambda)$  is the spectral transmittance through the target, which according to the principle of conservation of energy is equal to  $\tau_{IRg}(\lambda) = 1 - \varepsilon_{IRg}(\lambda) - \rho_{IRg}(\lambda)$ .

The evaluation of (1) in this work is facilitated by using a MatLab script [10]. Fig. 8 shows a region of the graphical interface generated by this script for a typical image recording of the micro turbine plume. The polygon defined by the red lines is conveniently chosen by the user to isolate the plume and to avoid the contribution of

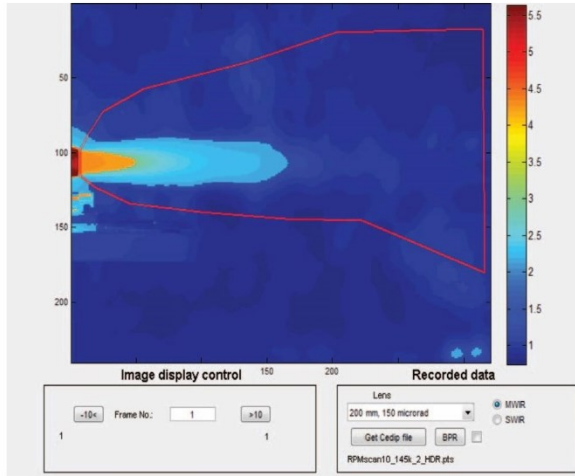


Fig. 8. Region of script's graphical interface showing typical image taken with MWIR camera. Tailpipe and support structure of turbine can be seen in left of image.

objects not of immediate concern, such as the tailpipe, support structure of the turbine, or undesired environmental IR sources, such as the two regions at the bottom right of Fig. 8. An additional threshold level is applied to the image to discard background pixels that are within the demarcated polygon area but do not contain information about the plume.

Depending on the target to be measured, some terms of (1) do not need to be considered. In the case of the micro turbine plume measurements, the third term on the right (environmental reflection) is not applicable, because it can be assumed that there is no IR reflection from any gaseous volume like a plume [11]; also, the fourth term (path radiance) was found to be negligible in the MWIR band with the plume being measured over a relatively small distance from the camera. The latter was easily confirmed by using the (Moderate Resolution Transmission) Modtran atmospheric transmittance modeling program [12]. In this way, the resultant plume measurement equation applicable to this study contains only the terms related to the target and background, i.e., the first and second terms on the right-hand side of (1).

Equation (1) can now be solved for  $L_{IRg}(\lambda)$  by means of a numerical technique if the spectral atmospheric transmittance, spectral instrument response, spectral background radiance, and plume spectral transmittance are known. Equation (1) can be rewritten in terms of the effective transmittance and effective response values, defined as the weighted averages over a specified spectral band of the spectral parameter.

The effective wideband transmittance of the background radiance through the plume is given by

$$\tau_{IRg.bkg}(r) = \frac{\int_{\lambda_1}^{\lambda_2} L_{bkg}(r, \lambda) \cdot \tau_{IRg}(\lambda) \cdot \tau_{instr}(\lambda) d\lambda}{\int_{\lambda_1}^{\lambda_2} L_{bkg}(r, \lambda) \cdot \tau_{instr}(\lambda) d\lambda} \quad (3)$$



The full effective wideband transmittance of the background radiance through the plume, as well as the atmosphere, toward the measuring instrument is described by

$$\tau_{atm.trg.bkg}(r) = \frac{\int_{\lambda_1}^{\lambda_2} L_{bkg}(r, \lambda) \cdot \tau_{trg}(\lambda) \cdot \tau_{atm}(r, \lambda) \cdot \tau_{instr}(\lambda) d\lambda}{\int_{\lambda_1}^{\lambda_2} L_{bkg}(r, \lambda) \cdot \tau_{trg}(\lambda) \cdot \tau_{instr}(\lambda) d\lambda}. \quad (4)$$

The effective transmittance of the target radiance through the atmosphere is

$$\tau_{atm.trg}(r, T) = \frac{\int_{\lambda_1}^{\lambda_2} L_{BB}(\lambda, T) \cdot \varepsilon_{trg}(\lambda) \cdot \tau_{atm}(r, \lambda) \cdot \tau_{instr}(\lambda) d\lambda}{\int_{\lambda_1}^{\lambda_2} L_{BB}(\lambda, T) \cdot \varepsilon_{trg}(\lambda) \cdot \tau_{instr}(\lambda) d\lambda}, \quad (5)$$

while the effective response of the instrument to the plume spectrum is given by

$$\tau_{instr.trg}(T) = \frac{\int_{\lambda_1}^{\lambda_2} L_{BB}(\lambda, T) \cdot \varepsilon_{trg}(\lambda) \cdot \tau_{instr}(\lambda) d\lambda}{\int_{\lambda_1}^{\lambda_2} L_{BB}(\lambda, T) \cdot \varepsilon_{trg}(\lambda) d\lambda}. \quad (6)$$

The MWIR data reduction equation in (1) for plume wideband radiance  $L_{trg}$  can now be written as

$$L_{trg}(r) = \frac{L^{meas} - L_{bkg}(r) \cdot \tau_{trg.bkg}(r) \cdot \tau_{atm.trg.bkg}(r)}{\tau_{atm.trg}(r, T) \cdot \tau_{instr.trg}(T)}, \quad (7)$$

where

$$L_{trg}(r) = \int_{\lambda_1}^{\lambda_2} L_{BB}(\lambda, T) \cdot \varepsilon_{trg}(\lambda) d\lambda \quad (8)$$

and

$$L_{bkg}(r) = \int_{\lambda_1}^{\lambda_2} L_{bkg}(r, \lambda) \cdot \tau_{instr}(\lambda) d\lambda, \quad (9)$$

i.e., the plume (target) radiance is obtained by first subtracting the contribution of the background radiance (as transmitted through the plume and atmosphere) from the measured plume radiance and then by correcting for the attenuating effect of the atmosphere and the instrument response on the plume radiance.

Other definitions for effective wideband parameters can also be used, as long as the data reduction equation in (7) remains mathematically identical to that in (1), albeit in a rearranged form. The target blackbody temperature  $T$  and the target emissivity  $\varepsilon_{trg}$  appear on the left and right sides of (1) and (7). Should these two parameters be

known, then  $L_{trg}$  could be calculated from (8) alone and no measurements are required. However, on a per-pixel basis, the values of  $T$  and  $\varepsilon_{trg}$  are generally different from pixel to pixel—the temperature inside the plume and the emissivity of the plume vary spatially. The inner part of the plume closest to the tailpipe typically has the highest blackbody temperature; this temperature lowers toward the edges of the plume, where it goes over to the ambient temperature of the surrounding atmosphere. The emissivity changes as a function of the thickness of the plume according to

$$\varepsilon_{trg}(\lambda) = 1 - \tau_{trg}(\lambda) = 1 - e^{-\int_0^L \kappa(\lambda, l) dl}, \quad (10)$$

where  $\kappa(\lambda, l)$  is the absorption coefficient of radiation at wavelengths  $\lambda$  at the position  $l$  along a specific line of sight path traversing a length  $L$  (representing thickness) through the plume [11, 13].

With the goal of mathematically modeling the plume, one temperature value and one emissivity spectrum representative of the plume as a whole prove to be sufficient, as shown in [13], where variations in temperature and emissivity are treated by scaling the value of  $L_{trg}$  per pixel according to the values of  $L^{meas}$  by using (7). Equation (7) is, however, also useful if the values of the spectral parameters are not exactly known—an approximate solution of  $L_{trg}$  can be obtained if only wideband estimates of these spectral parameters are known. Also, using the preceding effective parameter definitions, the resulting (7) is easier than (1) to interpret in terms of the relative contributions of the different influences of the atmosphere, background, and measuring instrument on the measured target radiance.

It can be seen that the parameters required to calculate  $L_{trg}(\lambda)$  from (7) are  $\tau_{instr}(\lambda)$ ,  $\tau_{atm}(\lambda)$ , and  $L_{bkg}(r, \lambda)$ , as well as the representative target temperature  $T$  and representative emissivity  $\varepsilon_{trg}(\lambda)$ , with the accompanying  $\tau_{trg}(\lambda) = 1 - \varepsilon_{trg}(\lambda)$ . For the small FOV measurements with the SR, following measurement equations describe the measurements made over the distance  $r$ :

$$L_{trg.BB}(\lambda) = [L_{BB}(\lambda, T) \cdot \tau_{trg}(\lambda) + L_{trg}(\lambda)] \cdot \tau_{atm}(\lambda) \quad (11)$$

and

$$L_{trg.pol}(\lambda) = [L_{pol}(\lambda) \cdot \tau_{trg}(\lambda) + L_{trg}(\lambda)] \cdot \tau_{atm}(\lambda), \quad (12)$$

where  $L_{trg.BB}$  is the measured radiance from the plume with the blackbody behind it and  $L_{trg.pol}(\lambda)$  is the measured radiance of the plume with the polystyrene board behind it. After subtracting (12) from (11), the plume transmittance is obtained as

$$\tau_{trg}(\lambda) = \frac{L_{trg.BB}(\lambda) - L_{trg.pol}(\lambda)}{[L_{BB}(\lambda) - L_{pol}(\lambda)] \cdot \tau_{atm}(r, \lambda)}. \quad (13)$$

#### IV. RESULTS AND DISCUSSIONS

The required parameters mentioned at the end of the previous section can usually be obtained by in the following ways:

- $\tau_{instr}(\lambda)$  can be obtained by the following:
  - Spectral response characterization measurements of the instrument [e.g., 14], as was done for the MWIR camera earlier
  - Calculation according to (2) if all required spectral parameters are known
- $\tau_{atm}(\lambda)$  can be obtained by the following:
  - Modtran calculations using the meteorological parameters recorded during the plume measurements as input, as was done in this work
  - Transmission measurements, which are typically quite difficult in practice over relatively long distances where large and high temperature sources are required to be observable by a SR

- $L_{bkg}(r, \lambda)$  can be approximated by the Planck function, using a temperature representative of the environment. A more correct value for the background radiance would involve a model of the background scene, which might be complex and elaborate. However, if the background behind the plume contains only objects at more or less ambient temperature, the contributions of these objects, after transmittance through the hotter plume, is negligible.

- Representative  $\varepsilon_{irg}(\lambda)$  can be obtained by the following:
  - The measurement of the radiance spectrum of the plume, using this with an estimate of the plume temperature at that position
  - Calculations using, e.g., the HITRAN2012 molecular spectroscopic database [15, 16]
  - The measurement of transmission through the plume by using a large-area blackbody behind the plume, as was done in this work, and then calculating  $\varepsilon_{irg}(\lambda)$  from this
- Representative target temperature  $T$  can be obtained by using a scaled-down value of EGT as an estimate of the plume temperature, as was done in this work (e.g., 15% lower than EGT [7])

Because of the difficulty in setting the turbine velocities to the exact intended values indicated in Section III of this work, the experimental values obtained during the RPM scan session differed slightly—e.g., the closest matches to the intended RPM values were 44 800, 58 700, 80 300, 98 800, 110 900, 119 900, 125 800, 130 100, 136 500, 142 300, and 144 100. In the following discussions, the intended nominal values are used to refer to the actual experimental values.

A direct thermocouple measurement in the RPM scan session was taken of the EGT and the engine pump power, as shown in Fig. 9. In this figure, the EGT covers the interval from 450°C to 650°C for the evaluated range of engine rotational speed, and this interval contains EGT values known to occur for full-scale aircraft [7]. The EGT

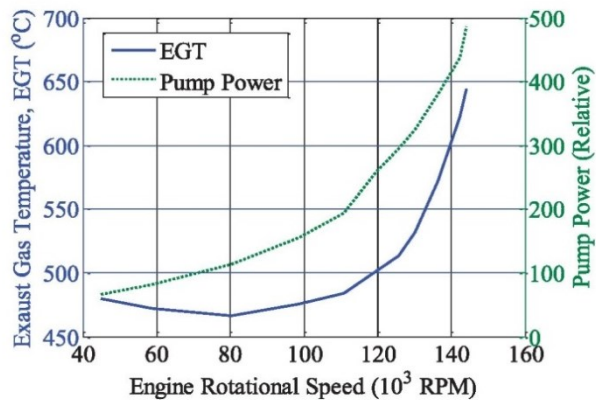


Fig. 9. EGT and pump power as function of engine rotational speed.

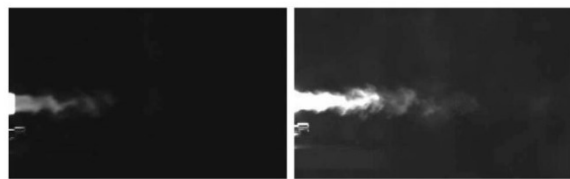


Fig. 10. Plume recordings in MWIR band at two RPM engine measurements: 45 000 RPM (left) and 145 000 RPM (right), both for 90° AA.

decreases from a maximum value at 100% of the maximum engine speed (145 000 RPM) toward lower engine settings, but it starts increasing again for RPM values decreasing below 55% of maximum engine speed (i.e., 80 000 RPM). Similar behavior has been reported in the literature [17] for a full-scale F109 turbofan engine, and it was attributed to the notion that the turbine is not running ideally, i.e., efficiently, until it is approaching approximately 70% of its maximum RPM. A similar view is presented as an explanation of the EGT behavior displayed in Fig. 9. The fuel consumption of the turbine also increases linearly with the potential difference applied to the fuel pump [18], indicated as relative engine pump power in this article.

Fig. 10 shows MWIR camera images taken during the RPM scan session for two engine rotational speeds: 45 000 and 145 000 RPM. The plume at 145 000 RPM is more intense than at 45 000 RPM, as expected.

To obtain the intensity (in watts per steradian) of the plume for the various cases of the RPM and AA scan sessions, shown in Figs. 11 and 12, respectively, the first step was to create an average radiance image using sequential MWIR images taken during a specific measurement point setting (of approximately 5 s). Such an average image effectively smoothes the frame-to-frame turbulent behavior seen on the edges of the plume. Two other images consisting of this average image ( $\pm 1$  standard deviation) were also created.

From the plume radiance and the area filled in an image by the plume, the intensity (product of mean radiance and area) can be calculated. The intensities obtained from the mean and mean  $\pm 1$  standard deviation



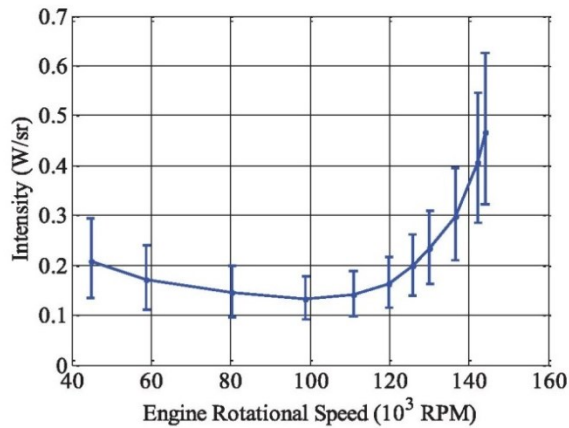


Fig. 11. Plume intensity (in watts per steradian) in MWIR (3–6  $\mu\text{m}$ ) band as function of engine rotational speed (RPM session) after data reduction.

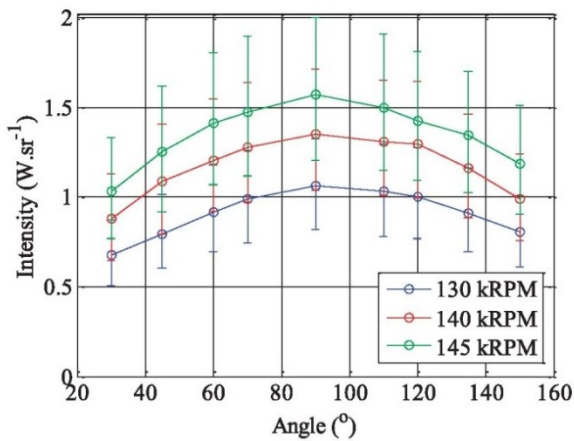


Fig. 12. Plume intensity (in watts per steradian) in MWIR band as function of engine rotational speed (RPM) for various AAs and three engine velocities.

plume images were calculated in the 3- to 6- $\mu\text{m}$  band, i.e., for  $\lambda_1 = 3 \mu\text{m}$  and  $\lambda_2 = 6 \mu\text{m}$  in (2), which resulted in the average intensity (blue curve) and its variation (error bars) as shown in Fig. 11. The intensity decreases gradually from  $\sim 0.2 \text{ W/sr}$  at 45 000 RPM to  $\sim 0.14 \text{ W/sr}$  around 100 000 RPM, which is a minimum value of the curve, and then increases rapidly as the design speed of the turbine is approached.

It is insightful when attempting to relate the plume intensity behavior exhibited in Fig. 11 with the EGT and pump power behavior presented in Fig. 9. The plume intensity would normally be proportional to the fuel consumption (i.e., pump power) [6, 9], because the fuel forms the source of the radiated energy of the plume—this would usually result in a monotonically increasing plume intensity as RPM increases according to the pump power curve in Fig. 9. However, the plume intensity is also a function of the EGT—if the plume intensity only followed the EGT behavior, it would result in decreasing and then increasing plume intensity behavior with increasing RPM according to the EGT curve in Fig. 9.



Fig. 13. Plume recording in MWIR band for  $90^\circ$  (left) and for  $135^\circ$  (right) AAs, both for 145 000 RPM, where no filter was used to have plume radiance well above detector noise level.

Because the plume intensity is, as can be seen in (8), a function of both 1) the fuel consumption, which manifests in  $\varepsilon_{\text{trg}}(\lambda)$  by means of a larger value of the plume thickness  $L$  and molecular density (reflected in  $\kappa$ ) shown in (10), and 2) the EGT, the intensity behavior shown in Fig. 11 should not come as a surprise. Observing Fig. 11, it is possible to infer the possible existence of a specified engine rotational speed to which a tracked aircraft’s pilot could set the aircraft’s engine to diminish the medium-wave IR engine signature. One must, however, be careful in affirming the exact engine rotational speed, because the result showed in Fig. 11 was obtained at ground level and with zero flying velocity, which is different from a real scenario.

Fig. 12 presents some results obtained from the AA scan session. The values refer only to the intensities of the plume—care was taken not to include the contribution of the tailpipe in the calculations. It can be seen that the curves are almost symmetric relative to an AA equal to  $90^\circ$ , with the intensities at larger angles (toward  $180^\circ$ ) slightly greater than those at smaller angles (toward  $0^\circ$ ). For example, the intensity for a 130 000 RPM engine setting is about  $1 \text{ W/sr}$  for  $120^\circ$  and about  $0.9 \text{ W/sr}$  for  $60^\circ$ , a difference of 10%. This indicates that it is not necessary to measure all angles covered in Fig. 12, which can be useful when the measurements present some difficulties, such as high costs incurred during a real-scale aircraft flight test. This comment is not valid for angles near  $0^\circ$  and  $180^\circ$ , which implies that the measurements need to be explicitly done around these angles.

The occurrence of the peak intensities for all engine settings at an angle of  $90^\circ$  is related to the larger projected area of the plume at this angle. This projected area is used in the calculation of plume intensity. Although the value of  $\varepsilon_{\text{trg}}(\lambda)$  is larger with respect to an observer at angles closer to  $0^\circ$  and  $180^\circ$  because of an effectively thicker plume, it is apparent from the intensity curves that the plume area is of more importance than the increased emissivity for the resultant intensity.

Figs. 13 and 14 show MWIR camera images for two AAs taken to evaluate the plume and tailpipe. The difference between these figures is the filter choice in each situation; in the first setup, no filter was used, while in the second setup, a 4% NDF filter was used to avoid saturation of the MWIR camera in the geometrical “hotter” region of the engine tailpipe. This twofold procedure allows operating in the desired linear region of the MWIR camera



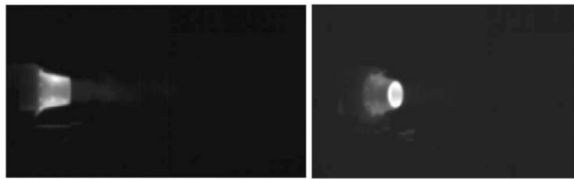


Fig. 14. Tailpipe recordings in MWIR band for 90° (left) and at 135° (right) AAs, both for 145 000 RPM, where 4% NDF filter was used to have no saturation in tailpipe pixels.

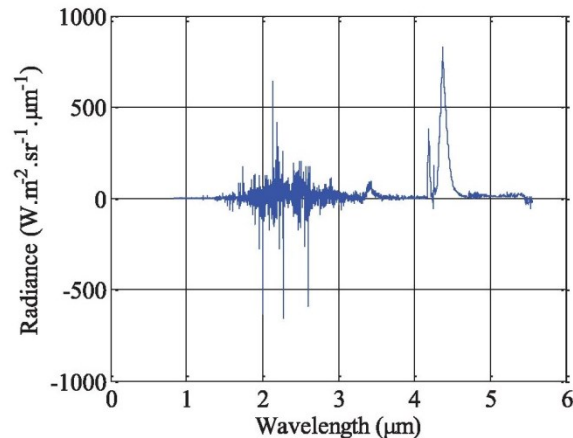


Fig. 15. Measured spectral radiance with SR for 145 000 RPM and 90° AA in small FOV session.

detector, without detector saturation in the tailpipe recording or a low signal-to-noise ratio for the plume recording. Data reduction of the tailpipe is not considered in this article, but it is deemed necessary to indicate the relative strength of this component of the aircraft with respect to the plume, because the tailpipe and the plume are usually inseparable for large AAs (especially larger than 90°) in the modeling and simulation of an aircraft.

Fig. 15 shows an SR curve obtained for a given measurement in the small FOV session. This curve was derived from an interferogram measured by the FTIR SR, obtained by converting it to a raw spectra followed by calibration (using prerecorded blackbody spectra) to obtain radiance values. In this figure, there is mostly instrumentation noise in the region from about 1 to 3 μm (SWIR region) because of limited sensitivity of the InSb detector in this wavelength region, as well as a weak source signal from the plume in this region (Kingtech emission similar to the 100% dry setting of an aircraft engine as oppose to an afterburner setting); a significant portion of the measured spectra is in the MWIR region, as mentioned earlier in this paper. The spectrally selective emission (in the region of 4.2 μm) exhibited in Fig. 15 is found in the plume of a full-scale aircraft, in which identical combustion processes take place [1, 6, 11]. This emission is the result of a transition between different energy levels of the carbon dioxide (CO<sub>2</sub>) molecule.

From the small FOV transmittance and radiance measurements, the emissivities of the three points

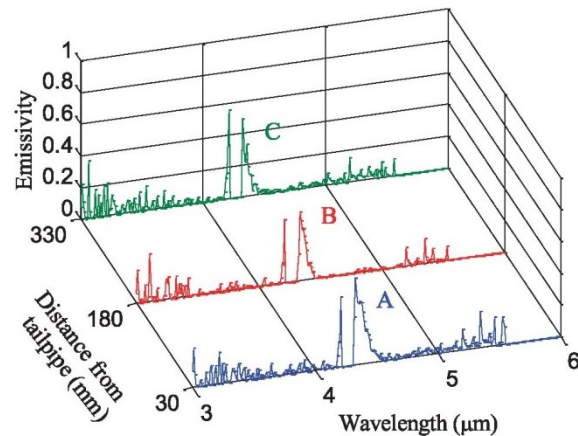


Fig. 16. Calculated apparent emissivity in points A, B, and C showed in Fig. 7 for 145 000 RPM and 90° AA.

referenced in Figs. 7 and 8 could be determined as showed in Fig. 16. The values shown are that of the “apparent” spectral emissivity, i.e.,  $\epsilon_{irg}(\lambda) \cdot \tau_{atm}(r, \lambda)$ , because for wavelengths where  $\tau_{atm}(r, \lambda)$  is close to zero, it is usually problematic to calculate the value of  $\epsilon_{irg}(\lambda)$  from (13). At these wavelengths, the value of  $\epsilon_{irg}(\lambda)$  can be obtained by one of the alternative methods mentioned earlier in this section. However, for measurements over relatively close distances, the apparent emissivity can be used in subsequent data processing and modeling work.

The strong effect of atmospheric CO<sub>2</sub> absorption around 4.2 μm is clear. The emissivity band, flanking the atmospheric CO<sub>2</sub> absorption band, broadened as the position of the FOV changed from C (far from the tailpipe) to A (close to the tailpipe). This can be attributed to a raised level of random thermal motions (Doppler broadening) and collisions (Lorentz broadening) of the radiating molecules at the higher temperatures and molecular densities [19] in the area closer to the tailpipe. However, it can be seen that the differences in the three spectra are relatively small, so the notion of using one of these spectra (or, e.g., an average of them) as a representative spectrum of the plume during data reduction, and later during modeling, is plausible. Scaling of these spectra to the spectrum expected from a larger-scale plume should be done with care, because some unusual scaling possibilities might exist, especially when working with optically thick plumes [20].

Finally, Fig. 17 presents the MWIR band radiance profile along the longitudinal axis of the plume, consisting of the curves obtained from the mean radiance images and mean  $\pm 1$  standard deviation images. The longitudinal axis is the axis that crosses the points A, B, and C referenced in Fig. 7. The sharp step around 0.5 m is a chosen end of radiance calculations.

The qualitative behavior of the radiance profile is as expected, with the highest radiance values closest to the tailpipe, where the highest plume temperature and molecular densities are found.

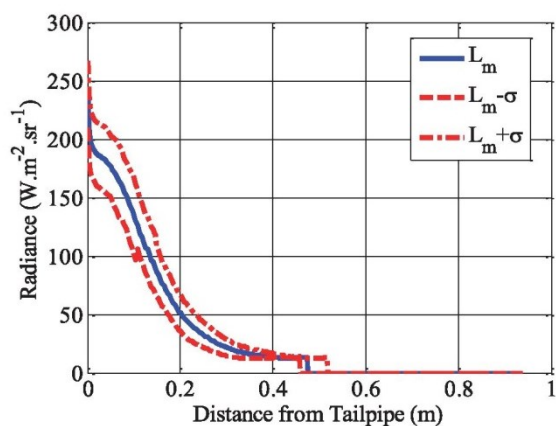


Fig. 17. Radiance profile along longitudinal axis of tailpipe-plume geometry, for case of 145 000 RPM and 90° AA.

## V. CONCLUSIONS

This paper presents a detailed description of the setup and instrumentation parameters used to measure radiometric properties of a micro turbine engine exhaust plume. Although this kind of engine is not used in real aircraft, the methods of measurement and data reduction presented can be applied similarly to larger-scale plumes of full-scale aircraft.

The micro turbine plume measurements present a cost-effective alternative to full-scale aircraft flight tests for obtaining insights into certain aspects of IR signature behavior. In general, experience in the successful IR signature measurement of gaseous types of objects and the data reduction thereof can be obtained by using a micro turbine engine as a target source.

The measured parameters presented in this work, such as EGT, plume emissivity, and radiance (e.g., along a plume's longitudinal axis), can, with proper scaling, be used in the numerical modeling of a larger-scale turbine engine's IR signature. Such a model is to be inserted into IR scenario simulation software, with the performed method to be presented in a future paper.

## ACKNOWLEDGMENT

The authors thank Denel Dynamics for the use of the equipment in their IR facility during this collaboration effort between Denel and the institutions with which the authors are associated.

## REFERENCES

- [1] Zissis, G. J., Ed. *The Infrared and Electro-Optical Systems Handbook: Sources of Radiation*, 2nd (revised) printing, Vol. 1. Bellingham, WA: ERIM and SPIE Press, 1996.
- [2] Willers, C. J. *Electro-Optical System Analysis and Design: A Radiometry Perspective*. Bellingham, WA USA: SPIE Press, 2013, p. 385.
- [3] Rao, G. A., and Mahulikar, S. P. New criterion for aircraft susceptibility to infrared guided missiles.

- Aerospace Science and Technology*, **9** (2005), 701–712.
- [4] Mahulikar, S. P., Sonawane, H. R., and Rao, G. A. Infrared signature studies of aerospace vehicles. *Progress in Aerospace Sciences*, **43** (2007), 218–245.
- [5] Sircilli, F., Retief, S. J. P., Magalhães, L. B., Ribeiro, L. R., Zanandrea, A., Brink, C., Nascimento, M., and Dreyer, M. M. Infrared characterization of a micro turbine engine plume. In *Proceedings of the 15th Simpósio de Aplicações Operacionais em Área de Defesa*, São José dos Campos, São Paulo, Brazil, 2013, 107–112.
- [6] Retief, S. J. P., Dreyer, M. M., and Brink, C. Infrared recordings for characterizing an aircraft plume. In *Proceedings of the SPIE: Sensors, MEMS and Electro-Optical Systems*, Vol. 9257, Skukuza, Kruger National Park, South Africa, 2014.
- [7] Hudson, R. D. *Infrared System Engineering*. New York: John Wiley & Sons, 1969.
- [8] Mahulikar, S. P., Rao, G. A., Sane, S. K., and Marathe, A. G. Aircraft plume infrared signature in nonafterburning mode: Technical notes. *Journal of Thermophysics and Heat Transfer*, **19**, 3 (2005), 413–415.
- [9] Retief, S. J. P., Smit, P., and Dreyer, M. M. Mid-wave infrared characterization of an aircraft plume. In *Proceedings of the IEEE Saudi International Electronics, Communications and Photonics Conference*, Riyadh, Saudi Arabia, 2011.
- [10] Retief, S. J. P. Cedip\_dr.m version 2012-09-11, unpublished.
- [11] Wormhoudt, J. (Ed.) *Infrared Methods for Gaseous Measurements—Theory and Practice*. New York, NY USA: Marcel Dekker, 1985.
- [12] Modtran software, <http://www.modtran5.com/>.
- [13] Retief, S. J. P. Aircraft plume infrared radiance inversion and subsequent simulation model. In *Proceedings of the SPIE: Technologies for Optical Countermeasures IX*, Vol. 8543, Edinburgh, United Kingdom, 2012.
- [14] Mermelstein, M. D., Snail, K. A., and Priest, R. G. Spectral and radiometric calibration of midwave and longwave infrared cameras. *Optical Engineering* **39**, 2 (Feb. 2000), 347–352.
- [15] Rothman, L. S., Gordon, I. E., Babikov, Y., Barbe, A., Benner, D. C., et al. The HITRAN2012 molecular spectroscopic database. *Journal of Quantitative Spectroscopy & Radiative Transfer*, **130** (2013), 4–50.
- [16] Heland, J., Schäfer, K., and Haus, R. FTIR emission spectroscopy and modeling of radiative transfer through a layered plume: Analysis of aircraft engine exhausts. In *Proceedings of the SPIE: Optical Sensing for Environmental and Process Monitoring*, Vol. 2365(117), McLean, VA, 1995, 117–125.
- [17] Harley, J. L., Rolling, A. J., Wisniewski, C. F., and Gross, K. C. Spatially resolved infrared spectra of F109 turbofan exhaust. In *Proceedings of the SPIE: Thermosense: Thermal Infrared Applications XXXIV*, Vol. 8354, Baltimore, MA, 2012, 83540H-1–83540H-10.
- [18] Flight Works. Fuel pump model 100-C, specification sheet. Orange County, CA, <http://www.flightworksinc.com>.
- [19] Hecht, E. *Optics*, 2nd ed. Reading, MA USA: Addison-Wesley, 1987, pp. 263–264.
- [20] Rudman, S., and Hibbeln, B. A. Scaling of optically thick plume signatures. *IEEE Aerospace Conference Proceedings*, **3** (2000), 265–270.





**Francisco Sircilli** was born in Paraná State, Brazil. He received his B.Sc. degree in physics in 1981 at São Paulo University (USP), Brazil, and his M.Sc. degree in 1986 at the National Institute for Space Research (INPE), Brazil, in the area of nuclear geophysics. In 1998, he received his Ph.D. degree at the Polytechnic Institute of USP in an area related to electrical power system.

He has been with the Institute for Advanced Studies, Aerospace Technology and Science Department, Brazil, since 1985, where he initially was joined with a team dedicated to developing a linear electron accelerator, specifically in its systems of refrigeration and electromagnetic components such as lens and solenoids. After that, he was involved in numerical simulation of optical fibers looking for its application as sensors. A few years ago, he started working in the IR field, especially in the evaluation of IR signatures and numerical simulation of IR scenarios.



**Ademilson Zanandrea** was born in Sananduva, Brazil. He received his B.Sc. degree in physics in 1991 from Santa Maria Federal University, his M.Sc. degree in space geophysics from INPE in 1998, and his Ph.D. degree in space geophysics from INPE in 1998.

From 1999 to 2007, he worked in signal and image processing/applied mathematics at the ITA, São José dos Campos, São Paulo, Brazil. In 2008, he changed his focus, dedicating his work toward IR measurements and modeling, when he signed on at Mecatron, an aerospace and defense manufacturing company in São José dos Campos, Brazil.



**Stephanus J. P. (Paul) Retief** was born in Rustenburg, South Africa. He received his B.Sc. degree in physics and mathematics/applied mathematics in 1993 and his M.Sc. degree in physics in 1995 from Potchefstroom (nowadays North-West) University in Potchefstroom, South Africa.

From 1995 to 2001, he worked in the field of seismology for local and international mining groups, as well as for the Council for Geoscience in Pretoria. He changed his focus in 2001 toward the field of IR measurements, modeling, and simulation when he signed on at Denel Dynamics, a missile and UAV manufacturing company. His main interest is IR modeling of gaseous volumes, especially aircraft plumes.



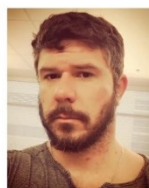
**Cornelis (Neels) Brink** was born in Bloemfontein, South Africa. He received his Ph.D. degree in physics from Potchefstroom University in 1993.

Between 1993 and 1996, he was involved in remote sensing for agricultural applications at the Institute for Soil, Climate and Water. Since 1996, he has been involved in modeling, measurement, and simulation of IR sources and backgrounds at Denel Dynamics. His work also includes evaluation of IR sensor systems, specification of sensor system performance, and general IR radiometry.



**Luciano B. Magalhães** was born in Teresina, Brazil. He received his B.Sc. degree in aeronautical sciences from the Air Force Academy, Pirassununga, São Paulo, Brazil, in 1996 and his M.Sc. degree in electronics and computer engineering from Aeronautical Institute of Technology, São José dos Campos, São Paulo, Brazil, in 2009.

From 1997 to 2007, he worked as a fighter pilot. Since 2000, he has been working as an electronic warfare officer of two squadrons and the Brazilian Air Force headquarters. His main research interests are IR modeling and measurements of aircrafts and flares, as well as self-defense systems.



**Maikon Nascimento** was born in Joinville, Brazil. He received his B. degree in Electrical Engineering in 2008 and he is currently a PhD candidate in electronic image processing at the University of Alberta, Canada. From 2009 until 2014 he worked with image processing and infra-red simulations at Denel Dynamics, A-Darter project.



**Luty R. Ribeiro** was born in Fortaleza, Ceará, Brazil, in 1988. He received his B.S. degree in computer engineering from the Aeronautical Institute of Technology (ITA), São José dos Campos, São Paulo, Brazil, in 2010. He successfully completed the aircraft weapon engineering extension course in 2011 at ITA and the infrared measurements and modeling training at Denel Dynamics, South Africa, in 2012.



**Maria M. Dreyer** was born in Warmbad, South Africa. She received her B.Sc. degree in physics and chemistry in 1982 and her M.Sc. degree in physics in 1986 from Potchefstroom University in Potchefstroom, South Africa.

During 1989, she started working at Kentron (now Denel Dynamics) in the IR field, with specific focus on measurements and modeling. Since 2004, she has been the manager of the radiometry department, which specializes in IR measurements, modeling, and simulation.

## CHAPTER 5      OBTAINING THE AIRCRAFT PLUME INNER STRUCTURE

### 5.1 INTRODUCTION

The radiance emanating from a gaseous medium is the resultant balance of the attenuation of the radiation propagating through it and the intensification of this radiation by the addition of newly generated radiation, as described by the basic equation of radiative transfer in Section 5.2. In order to model the observed radiance at any observation position outside the emitting volume, the inner structure of the volume is required, i.e. the (spectral) absorption coefficient and the (spectral) emission coefficient of each volume element inside the volume must be known. Once this information is available, modelling of radiative transfer inside the plume can be done by utilizing the formal solution of the radiative transfer equation.

Upon completion of the aircraft plume data reduction process described in Chapter 4, the source radiance profiles (also called the ‘absolute’ radiance profiles) of the aircraft plume are obtained. These plume profiles are two-dimensional cross sections, also called projections or attenuated Radon transforms, of a three-dimensional object (the plume), as is studied in the field of tomography. The main goal of the publication in Section 5.2 [5] is to devise an appropriate radiance reconstruction/inversion technique, i.e. to devise an algorithm for the reconstructive tomography of obtaining the required parameters of each volume element inside the plume.

The available algorithms in reconstructive tomography can broadly be classified into two types – analytical and iterative [19]. Analytical solutions exist for the first term in Equation (2) of Section 5.2, i.e. when the medium under study only exhibits attenuation and does not emit radiation itself, and for the second term in Equation (2) when the medium under consideration is self-emitting but with no self-attenuation (i.e.  $\kappa = 0$ ). Cases with self-emission but where self-attenuation also exists, such as inside an aircraft plume, cannot be handled easily by analytical methods, and the iterative methods are employed. An iterative technique usually divides the source region into discrete elements so that any observer’s line of sight (LOS) through the source is

divided into segments equal to the lengths contained in each discrete element. An iterative scheme is then applied during which weights are assigned to the contribution of each element towards the observed radiance, with the weights being tweaked during each iteration until the calculated projections agree with the measured ones.

Various articles report on the iterative methods to reconstruct the attenuated Radon transform from a gaseous object, with some requirements or assumptions related to each of them. The following are typical examples:

- The absorption coefficient must be known or determined separately from the process of reconstructing the measured Radon transform [20].
- The absorption coefficient must be small and constant throughout the gaseous volume, with the temperature at some positions in the flame known [21].
- The absorption coefficient must be constant [22,23].
- The basic form of the attenuation must be known beforehand in order to constrain the final attenuation and emission distribution obtained by an iterative procedure [24].
- Measurements in two different wavelength bands must be known with no attenuation [25–27].

The main challenge for an *in situ* aircraft plume is the simultaneous determination of the source function of the plume and the attenuation coefficient, which is addressed in Section 5.2.

For the case of no attenuation and axi-symmetrical radiance, the projected radiance is called an Abel transform, which is a special case of the Radon transform. Although the attenuation in the plume cannot outright be assumed to be negligible, the technique presented in Section 5.2 was initially tested by means of a simplified, synthetic axi-symmetric ‘observed’ profile. This profile is shown as the black curve, denoted as ‘Real profile used as input’, in the bottom graph of Figure 5-1. For the case of no attenuation, the inverse Radon transform function `iradon.m` of the Matlab<sup>®</sup> software package was used to reconstruct the cross section profile, shown in the top graph of Figure 5-1. In order to compare the proposed reconstruction technique of Section 5.2 with this inverse Radon transform, the attenuation coefficient was set to  $\kappa = 0.001$  so that the attenuation through the medium was negligible. The results of the two reconstructed profiles were in good agreement. Further testing was done by calculating the observed profiles given in the two reconstructed profiles with the results being shown in the bottom graph. It can be seen in Figure 5-1 that the observed profile obtained from the proposed reconstruction technique profile is in exact



agreement with the input profile, while that is not the case for the inverse Radon transform. This then confirmed that the proposed technique should perform well.

Another goal of the publication in Section 5.2 was to provide a method of modelling an aircraft plume once the inner radiance structure of the plume has been determined.

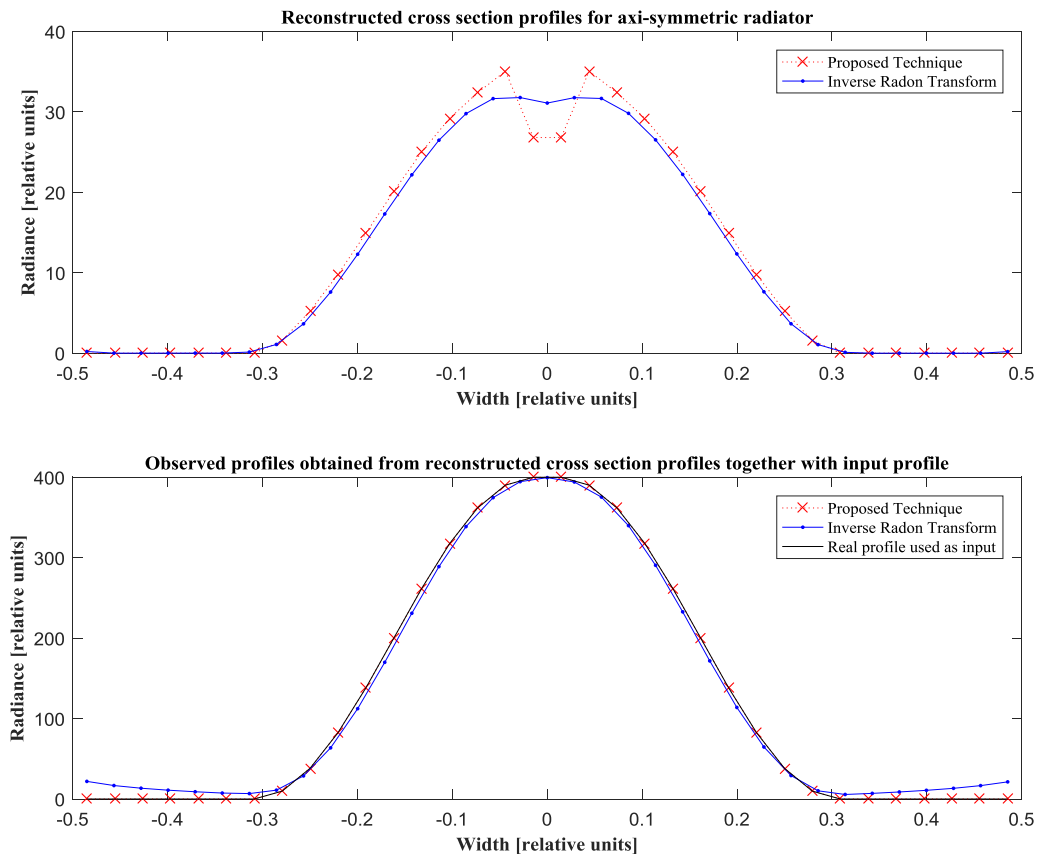


**Figure 5-1** The ‘observed’ profile (black curve bottom graph) is used as input to the reconstruction techniques indicated in the figure.

## 5.2 PUBLICATION – AIRCRAFT PLUME INFRARED RADIANCE INVERSION AND SUBSEQUENT SIMULATION MODEL

This publication, with the developed technique reported therein, was the sole work of the present author. The publication was reviewed by the conference chair/committee members of the conference where it was presented.

The article was published in the Proceedings of the SPIE (The International Society for Optical Engineering) Technologies for Optical Countermeasures IX conference held in Edinburgh, Scotland [5].

# Aircraft plume infrared radiance inversion and subsequent simulation model

S. J. P. Retief\*,

Simulation and Design Department, Denel Dynamics, P.O. Box 7412, Centurion, 0046, South Africa

## ABSTRACT

A radiance inversion technique, in which in-flight aircraft plume radiance recordings are exploited to construct a three-dimensional (3D) radiance model of the plume, is presented. The recordings were done with a mid-wave infrared (3 – 6  $\mu\text{m}$ ) camera at different altitudes.

The algebraic formulation of this inversion technique, also known as an emission-absorption technique, is stated for the ideal case of spectral radiance measurements of a high spatial sampling resolution over the plume area, as would be obtained from a hyperspectral imager. The non-ideal case of having only broad-band (mid-wave) image measurements and only one spectral measurement of the plume, is then investigated. It is shown that from this incomplete information set, an effective spectral absorption coefficient can be calculated for which the associated plume spectral transmittance and spectral emissivity calculations exhibit the correct qualitative behaviour. It is also shown that, by using this effective absorption coefficient, an optimization procedure can be used to determine the temperatures and/or spectral radiance values within the plume. This optimization procedure consists of minimizing the difference between the observed line-of-sight (LOS) radiance in the image (i.e. a pixel radiance value in the image) and its theoretical projected radiance.

After the temperature values within the plume were determined, the observer LOS radiance is parameterized so that it can be described for an arbitrary angle with respect to the main axis of the plume. The inferred temperature, spectral transmittance and spectral emissivity are then used in calculating the expected spectral radiance at this arbitrary angle. The spectrally integrated/mid-wave broad-band radiances and intensities for aspect angles other than those used during the inversion process, are then calculated and compared with actual measurements in order to determine the adequacy of this model for incorporation into existing infrared imaging system simulation software used in the training of infrared seekerhead missiles.

**Keywords:** Radiance inversion, 3D radiance model, aircraft plume, mid-wave infrared, hyperspectral

## 1. INTRODUCTION

When the effectiveness of a decoy countermeasure against a missile attack is evaluated within a simulation environment, both the countermeasure and the platform protected by the countermeasure have to be represented in the simulation. Furthermore, the simulation should accurately reflect not only the decoy properties and behaviour, which usually mimics that of the platform, but also that of the platform.

Some of the key considerations in an imaging infrared simulation of a missile-aircraft engagement are the radiometric accuracy and fidelity of the geometrical and spatial texture of the aircraft or countermeasure being simulated<sup>1</sup>. The key objective in the target identification process of a missile is to classify objects into targets and non-targets. If either the countermeasure or the target aircraft is not simulated to a sufficient level of accuracy, it will not be possible to evaluate the countermeasure efficiency. Therefore, the successful evaluation of a countermeasure in a simulation environment depends just as much on the correct simulation of the platform it protects as on the correct simulation of the countermeasure itself – any subtle property and behaviour differences between the decoy and the aircraft should manifest in the simulation. This paper will concentrate on the modelling of the infrared signature of an aircraft plume, which is an important consideration in missile seeker algorithms for discriminating between an aircraft and a countermeasure. Use was made of infrared measurements in deriving the plume model.

\*paul.retief@deneldynamics.co.za; phone +27 12 671 1817; fax +27 12 671 1616; www.deneldynamics.co.za

The radiance inversion technique presented in this paper is a variation of the ‘Finite Width Onion Peel Inversion’<sup>7</sup> and was built around available infrared measurements of an aircraft plume at a 100% dry engine setting (maximum turbine revolutions). These measurements comprised 3 – 6  $\mu\text{m}$  mid-wave infrared images (MWIR), which were recorded in-flight during a flight test, and one spectral recording of the plume recorded during a static ground test<sup>2</sup>. Although current missiles operate in wide spectral bands, typically 3 – 6  $\mu\text{m}$  and in short wave bands covering wavelengths shorter than 3  $\mu\text{m}$ , it is of importance to have a spectral model of the plume. The spectral content of the plume signature is influenced, amongst other influences, by the observation angle of the plume, and this variation reflects in the integrated wide-band radiometric quantities.

The data reduction of the mid-wave images is reported on in [2]. During this data reduction process, corrections of unwanted influences on the plume measurements, i.e. atmospheric attenuation of the plume radiance, background radiance emission through the plume and atmospheric path radiance of the atmosphere, were made in order to obtain the ‘absolute’ values of the plume radiance. However, these absolute radiances represent the projected radiance values, i.e. the values observed at a specific viewing/aspect angle of the plume. Since the plume is a partially transparent gaseous radiator, the projected radiance values will change with changing viewing angles. Of importance here are the recordings at an aspect angle of  $90^\circ$  – a radiance inversion technique can be applied to the absolute radiance values recorded at the  $90^\circ$  aspect angle in order to obtain the internal three-dimensional radiance structure of the plume.

In the following sections this radiance inversion technique, as applied to the absolute radiance values of the plume, will be presented. At first, the ideal case is stated for which spectral radiance measurements of a high spatial sampling resolution over the plume is available. Then, the non-ideal case, of which the available measurements form an instance, is treated. Having obtained the internal plume radiance structure, a more generalized model than the one used during the inversion process can be used in calculating the radiance and intensity values at an arbitrary aspect angle. The model is also compared with measured intensities available at aspect angles of  $10^\circ$  and  $20^\circ$ , which serves as a verification of the adequacy of the radiance inversion technique applied. The generalized model can then be used in a simulation to simulate an aircraft plume.

## 2. RADIANCE INVERSION FOR THE IDEAL CASE

The variation in radiance along a certain LOS path in a gaseous volume can be described by the radiative transfer equation (see e.g. [3] for a comprehensive treatment of radiative transfer):

$$\frac{dL_\lambda(l)}{dl} = -\kappa(\lambda, l)L_\lambda(l) + J_\lambda(l) \quad (1)$$

where  $l$  is the length along the path which the radiation travel,  $\kappa(\lambda, l)$  is the spectral absorption coefficient [ $\text{m}^{-1}$ ] of the medium at position  $l$ ,  $L_\lambda(l)$  is the spectral radiance [ $\text{W} \cdot \text{m}^{-2} \cdot \text{sr}^{-1} \cdot \mu\text{m}^{-1}$ ] at wavelength  $\lambda$  of the propagating radiation at position  $l$  and  $J_\lambda(l)$  is the spectral emission coefficient [ $\text{W} \cdot \text{m}^{-2} \cdot \text{sr} \cdot \mu\text{m}^{-1} \cdot \text{m}^{-1}$ ], representing the radiation originating along the path of the gaseous medium. The  $\lambda$  suffixes will however be suppressed in the rest of the discussion in order not to bestow clutter on the radiometric symbols used. If non-spectral quantities are used, it will be clearly indicated.

The formal solution to the radiative transfer equation is given by the line integral

$$L_{proj} = L(0)\exp\left(-\int_0^l \kappa(l)dl\right) + \int_0^l J(l)\exp\left(-\int_l^l k(l')dl'\right)dl', \quad (2)$$

where  $L_{proj}$  is the projected radiance, i.e. the radiance as observed at the end of the path at position  $l$  and  $L(0)$  is the background radiance, i.e. any existing radiance behind the gaseous volume.

The exponential function in this equation represents the transmittance through the medium, i.e.

$$\tau(l, l') = \exp\left(-\int_{l'}^l \kappa(l')dl'\right). \quad (3)$$

In order to apply the radiative transfer equation to the plume model geometry to be described shortly, Equation 2 is discretized so that

$$L_{proj} = L(0)\exp\left(-\sum_{j=1}^n \kappa(l_j)\Delta l_j\right) + \sum_{j=1}^n \Delta L(l_j)\exp\left(-\sum_{h=j+1}^n \kappa(l_h)\Delta l_h\right),$$

i.e.



$$L_{proj} = L(0)\exp(-\sum_{j=1}^n \kappa(l_j)\Delta l_j) + \sum_{j=1}^n \Delta L(l_j) \prod_{h=j+1}^n \tau_h, \quad (4)$$

with  $l_1$  representing the first path segment of the radiance propagation path and  $l_n$  the last segment in this path ( $n \geq 2$ ), and  $\Delta l_j$  representing the length of a path segment  $j$  and  $\Delta L(l_j)/\Delta l_j \equiv J(l_j)$  the change in radiance after traversing the path segment length  $\Delta l_j$  at position  $l_j$ . For the special case, where  $n = 1$ , i.e. a homogenous medium of width  $\Delta l$  with a constant absorption coefficient,  $\kappa$ ,

$$L_{proj} = L(0) \exp(-\kappa\Delta l) + \Delta L(l). \quad (5)$$

When no background radiance exists, as is the case for the absolute radiance values of the plume, the first term in Equation 4 and 5 is set to zero. For the situation of local thermal equilibrium in a gaseous radiator, the absorption at each point along the propagation path is equal to the medium's emission at that point so that the source function,  $\mathfrak{S}_\lambda = \frac{J_\lambda}{\kappa_\lambda}$ , can be described in terms of the well-known Planck (blackbody) function<sup>3</sup>. Equation (4) then becomes

$$L_{proj} = \sum_{j=1}^n L_{BB}(T_j) \varepsilon(\Delta l_j) \prod_{h=j+1}^n \tau_h, \quad (6)$$

where  $L_{BB}(T_j)$  is the Planck function at a local temperature  $T_j$  in the plume and  $\varepsilon(\Delta l_j)$  is the emissivity of segment  $\Delta l_j$ .

Figure 1 shows a diagram representing a cross section of a plume. The horizontal lines through the cross section represent the paths followed by the plume radiation towards an observer at the right end of the lines, i.e. a horizontal line represents a Line Of Sight (LOS) of an observer. The cross section is divided into annular regions, with each region being considered to be homogeneous in temperature, pressure and molecular species and their density. The outer region is designated as having a temperature  $T_1$ , absorption coefficient  $\kappa_1$ , radiance  $L_1$ , etc., resulting in a projected radiance  $L_{proj_1}$  for the associated LOS; the second outermost region has a temperature  $T_2$ , absorption coefficient  $\kappa_2$ , radiance  $L_2$ , etc., resulting in a projected radiance  $L_{proj_2}$ , and so on. It can be seen from the figure that the annular regions divide each LOS into segments, each segment identifiable by indices  $(i, j)$ , with index  $i$  numbering the LOS starting at 1 for the top LOS, i.e.  $LOS_1$ , and ending at  $m$  at the middle of the plume,  $LOS_m$ . Index  $j$  numbers the segments, starting from left and increasing towards the right hand side. The length of any segment can easily be referred to as  $\Delta l_{ij}$ . In terms of the symmetrical geometry of this plume cross section, Equation 6 can be used to describe the projected radiance for each LOS:

$$L_{proj_i} = \sum_{j=1}^i L_{BB_j} \varepsilon_{i,j} (\prod_{h=j+1}^i \tau_{i,h} + \prod_{h=1}^{j-1} \tau_{i,h}), \quad (7)$$

with  $\prod_{h=1}^m \tau_{i,h} \equiv 1$  for  $m = 0$ ; the meanings of the symbols are the same as mentioned earlier, except that a reference to a specific LOS is now made with index  $i$ .

The transmittance and emissivity in Equation (3) for a specific LOS segment is

$$\tau_{i,h} = \exp(-\kappa_i \Delta l_{i,h}), \quad (8)$$

and

$$\varepsilon_{i,h} = 1 - \tau_{i,h} \quad (9)$$

respectively, with  $\Delta l_{i,j} = \left| \sqrt{R_j^2 - y_i^2} \right| - \left| \sqrt{R_{j+1}^2 - y_i^2} \right|$  for all  $i > j$ , and  $\Delta l_{i,j} = \Delta l_{i,2i+1-j}$  for all  $i < j$ , and  $\Delta l_{i,i} = \left| \sqrt{R_i^2 - y_i^2} \right|$ . The values of  $y_i$  is calculated in terms of the radii of the annular regions as  $y_i = \frac{R_i + R_{i+1}}{2}$  with  $y_n = 0$  for the innermost segment.

The absorption coefficient  $\kappa_i$  is the product of the mass absorption coefficient,  $k_i$ , and the density of a chemical species,  $\rho_i$ . Since the plume consists of more than one chemical species, notably  $CO_2$  and  $H_2O$  at least, the spectral absorption coefficient is in fact the summation of all the different species, i.e.  $\kappa_i = \sum_{m=1}^q \kappa_{i,m}$ , with  $q$  the number of species present in annular region  $i$  and  $\kappa_{i,m}$  the absorption coefficient of a specific species (cf. [4]).

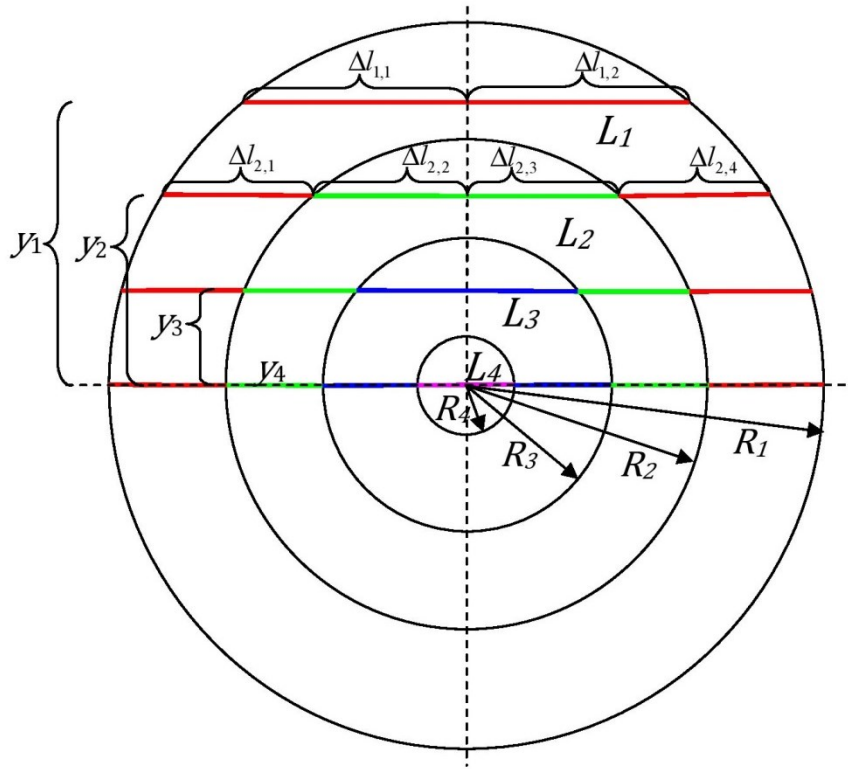


Figure 1. Schematic diagram representing a cross section through the plume of an annular plume model.

The set of equations in Equation 7 can be presented in matrix form as

$$\begin{bmatrix} \alpha_{1,1} & 0 & 0 & 0 \\ \alpha_{2,1} & \alpha_{2,2} & 0 & 0 \\ \alpha_{3,1} & \alpha_{3,2} & \alpha_{3,3} & 0 \\ \alpha_{4,1} & \alpha_{4,2} & \alpha_{4,3} & \alpha_{4,4} \end{bmatrix} \begin{bmatrix} L_{BB1} \\ L_{BB2} \\ L_{BB3} \\ L_{BB4} \end{bmatrix} = \begin{bmatrix} L_{proj1} \\ L_{proj2} \\ L_{proj3} \\ L_{proj4} \end{bmatrix} \quad (10)$$

for the case shown in Figure 1, i.e. where the number of annular regions  $m = 4$ . In this representation

$$\alpha_{i,j} = \varepsilon_{i,j} (\prod_{h=j+1}^{2i} \tau_{i,h} + \prod_{h=1}^{j-1} \tau_{i,h}) \quad (11)$$

with  $\alpha_{i,j} \equiv 0$  for  $i < j$ . The above matrix equation can be written in bold symbols representing matrices as

$$\mathbf{\alpha L_{BB}} = \mathbf{L_{proj}} \quad (12)$$

and it can easily be solved for  $L$  at each value of  $\lambda$ , i.e

$$\mathbf{L_{BB}} = \mathbf{\alpha}^{-1} \mathbf{L_{proj}} \quad (13)$$

It can be seen from these equations that in order to obtain the radiance structure inside the plume, the information required is

1. The projected spectral radiance profile,  $L_{proj}$
- AND
2. The profile of the absorption coefficient,  $\kappa_i$ , for  $i = 1, \dots, m$
- OR



2. The total transmittance profile,  $\tau_{tot_i} \equiv \prod_{j=1}^{2i} \tau_{i,j}$  from which  $\tau_{i,j}$  or  $\kappa_i$  for  $i = 1, \dots, m$  and  $j = 1, \dots, 2i$  can be determined.

The instrument needed to determine this information is a spectroradiometer, or, more ideally, a hyperspectral imager, together with a blackbody source behind the aircraft plume in order to obtain spectral measurements sampled over the length and width of the plume. The calculations of Equation 13 are repeated for each  $\lambda$  sampled during the measurement and for all vertical arrays of measurements through the width of the plume, i.e. projected radiance profiles, at different distances behind the aircraft tailpipe.

For an optically thin plume, i.e. for a relatively small value of the optical depth  $\kappa \Delta l$  resulting in values of  $\tau_{tot}$  being close to one, the radiance can be inverted having only the observed radiance profile  $L_{proj}$ . In [5], a method is described of obtaining the temperatures of each zone, as well as the Abel integral inversion method, which can be applied to radially symmetric profiles (like an aircraft plume) in order to obtain the radiance distribution inside the plume (also cf. [6]).

When self-absorption is non-negligible (plume is not optically thin), measurements of the transmittance profiles mentioned in point 2 above are obligatory to enable radiance inversion<sup>5</sup>. A setup for the measurement of transmittance profiles through a plume, described in [7], consists of a graybody/blackbody (heat source having constant emissivity) on one side of the plume with a detector optically aligned on the other side. Use is then made of mechanical choppers at the detector and source and phase-locked amplifiers, which allows the recording of plume radiation alone as well as plume and grey body radiation.

The values of the transmittance of each annular region over the traversing length of the LOS can be obtained from the measured total transmittance profile by first obtaining  $\tau_{i,j}$  for  $i = 1$ , i.e. from

$$\tau_{tot_1} = \prod_{j=1}^2 \tau_{1,j} = \tau_{1,1} \tau_{1,2} = \tau_{1,1}^2, \quad (14)$$

one obtains the transmittance of the first segment of LOS<sub>1</sub>,  $\tau_{1,1} = \sqrt{\tau_{tot_1}}$ . Knowing the value of  $\tau_{1,1}$ , the value of  $\kappa_1$  can be determined from  $\kappa_1 = -\frac{\ln(\tau_{1,1})}{\Delta l_{1,1}}$ .

For LOS<sub>2</sub>,  $\tau_{tot_2} = \prod_{j=1}^4 \tau_{2,j} = \tau_{2,1} \tau_{2,2} \tau_{2,3} \tau_{2,4} = \tau_{2,1}^2 \tau_{2,2}^2$ , and therefore  $\tau_{2,2} = \sqrt{\frac{\tau_{tot_2}}{\tau_{2,1}^2}} = \sqrt{\frac{\tau_{tot_2}}{(\exp(-\kappa_1 \Delta l_{2,1}))^2}}$ .

The above procedure can repeatedly be applied to obtain the transmittance for each annular segment in each LOS. The general form of the algorithm applied during each increment of  $i$  is shown in Figure 2.

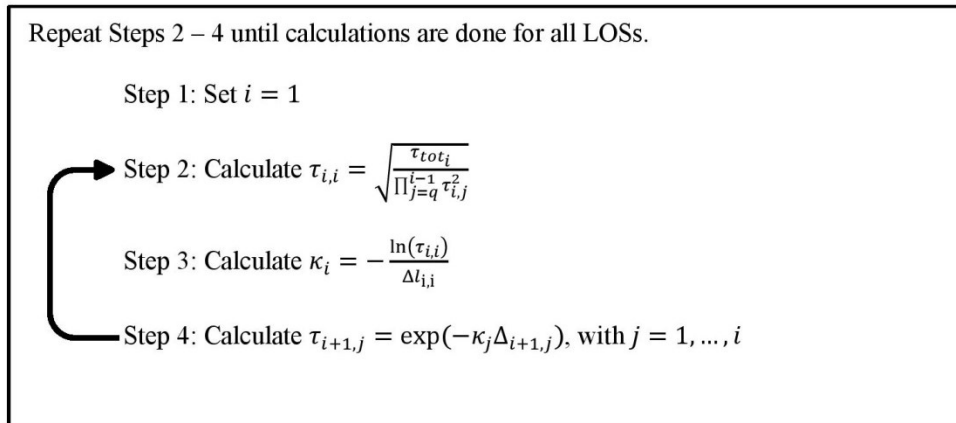


Figure 2. Algorithm for calculating the transmittance of each segment of each LOS of the annular plume model.

### 3. RADIANCE INVERSION FOR THE NON-IDEAL CASE

Obtaining ideal measurements for radiance inversion of an aircraft plume is difficult, especially when it is attempted to make recordings of an *in situ* jet fighter aircraft plume. It is not a trivial task to configure a blackbody source of radiation behind the aircraft plume while in flight (if at all possible), nor is a hyperspectral imager always available for these kinds of measurements. It is, however, of importance to carry out in-flight measurements in order to characterize the plume shape, radiance distribution and intensity as a function of altitude<sup>2</sup>, speed and engine setting. Having only mid-wave infrared images in the 3 – 6  $\mu m$  band available from in-flight recordings, and a spectral radiance measurement recorded during a static ground test, the technique described in Section 2 was adapted to make use of these available plume recordings. To summarize – the first inadequacy of the available data is that there are no spectral transmission measurements; the second inadequacy of the data is that there are not sufficient spectral radiance measurements. The first inadequacy is dealt with first.

The spectral emissivity, shown in Figure 3, was taken from available historical recordings of an aircraft plume at an aspect angle of 90° as measured from the nose of the aircraft at a position of 0.5 m behind the tailpipe (similar to [8]). The field of view (FOV) of the spectroradiometer covered a circular area within the plume with diameter of approximately 60% of the plume width. Since the temperature, transmittance and emittance varies throughout the plume as a function of position in the plume (in a manner indicated by the plume model of the previous section), the emissivity spectrum obtained from the static ground test is at best an average or effective emissivity of the different regions in the FOV having different local temperature and emissivity values. From this effective emissivity, representing the emissivity of the plume in the FOV of the spectroradiometer, an effective absorption coefficient can be calculated:

$$\begin{aligned}\varepsilon_{eff} &= 1 - \tau_{eff} \\ &= 1 - \exp(-\kappa_{eff}\Delta l)\end{aligned}\quad (15)$$

i.e.

$$\kappa_{eff} = -\frac{\ln(1-\varepsilon_{eff})}{\Delta l}.\quad (16)$$

If the value of  $\Delta l$  is set equal to the actual physical width of the plume, i.e.  $\Delta l = 2R_1$  with  $R_1$  referring to the outermost annular region in the cross section of the plume as shown in Figure 1, then the effective spectral absorption coefficient shown in Figure 3 is obtained. Although it is known that the absorption coefficient spectrum is not constant throughout the plume, the spectrum shown in Figure 3 can be used to calculate the values of  $\tau_{i,j}$ , which are required for the radiance inversion. A check on the realism of the calculated effective absorption coefficient was done by calculating the total transmittance,  $\tau_{tot}$ , for various LOSs at different distance from the plume centre using this value. The results, shown in the right hand side plot of Figure 3, are realistic in the sense that the transmittance increases as the distance between the centre of the plume and the LOS increases.

By obtaining the required  $\tau_{i,k}$  values from  $\kappa_{eff}$ , and from that the values of  $\varepsilon_{i,k}$ , the values of  $\alpha_{i,h}$  can now be obtained as prescribed by Equation 11. In such a manner the inadequacy of the recorded data, which lacks transmittance measurements, can be overcome.

The second inadequacy of the recorded data, that of the radiance measurements not being spectral but only broad-band images as shown in Figure 4, is now dealt with.

Equation 10 can be rewritten as

$$L_{proj_i} = \sum_{j=1}^i \alpha_{i,j} L_{BB}(T_j),\quad (17)$$

with  $i = 1, \dots$ , number of annular regions. However, the infrared images are non-spectral and is therefore described by

$$L_{proj_i}^{wb} = \int_{3\mu m}^{6\mu m} \sum_{j=1}^i \alpha_{i,j} L_{BB}(T_j) d\lambda,\quad (18)$$

where  $L_{proj_i}^{wb}$  refers to the wide-band (wb) measurement over 3 – 6  $\mu m$ . On discretization, this equation becomes

$$L_{proj_i}^{wb} = \sum_{k=0}^n \sum_{j=1}^i \alpha_{i,j} L_{BB}(T_j) \Delta\lambda,\quad (19)$$

where  $\lambda_k = \lambda_0 + k\Delta\lambda$ , with  $\lambda_0 = 3 \mu m$ , and  $\lambda_n = 6 \mu m$ .

After the values of  $L_{proj_i}^{wb}$  and the spectral values of  $\alpha_{i,j}$  were calculated by the means explained, the values of  $T_j$  can be obtained from the solution of

$$\sum_{k=0}^n \sum_{j=1}^i \alpha_{i,j} L_{BB}(T_j) \Delta\lambda - L_{proj_i}^{wb} = 0 \quad (20)$$

for each value of  $i$ . At first, the value of  $T_1$  is obtained for  $i = 1$ . Having the value of  $T_1$ ,  $T_2$  can be obtained for  $i = 2$ , etc. The value of  $L_{BB}(T_j)$  increases monotonically with an increasing value of  $T_j$ , so that a very simple numerical method can be used to determine the correct value of  $T_j$  for which the left side of Equation 20 is sufficiently close to zero. In such a manner the inadequacy of the recorded data, which lacks spectral radiance measurements, can be compensated for.

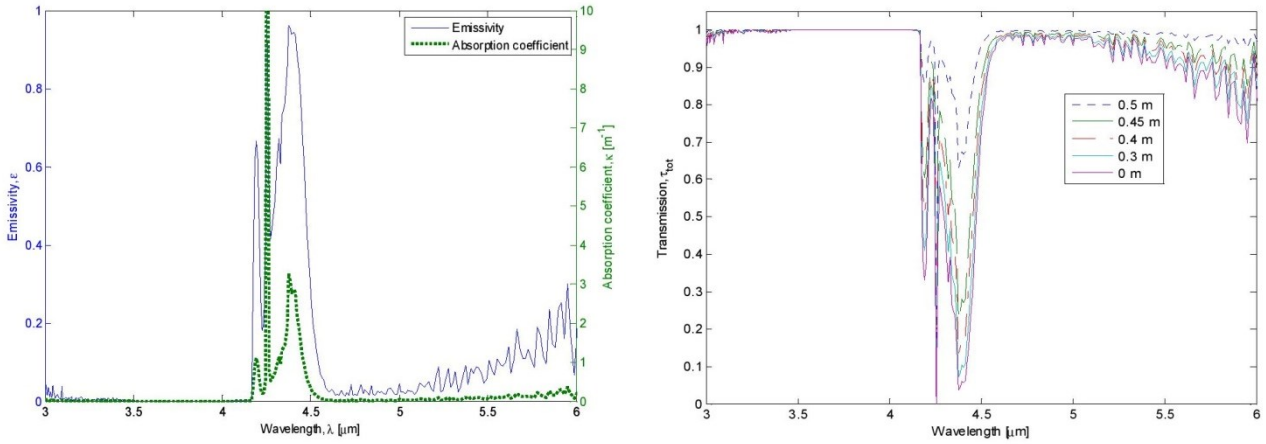


Figure 3. The effective emissivity spectrum of the plume and the absorption coefficient derived from this spectrum is shown in the left figure; the total transmittance of the plume at various distances from the plume centre is shown in the right figure.

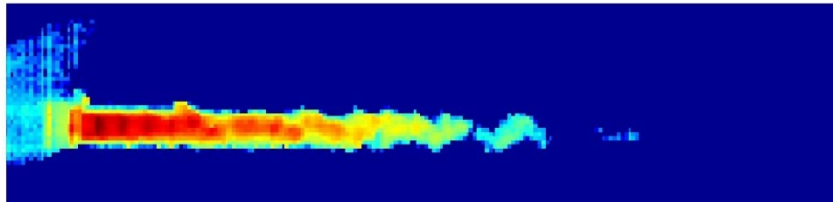


Figure 4. Example of recorded mid-wave infrared image of plume in false colours. Note the Mach discs in the plume.

## 4. RADIANCE INVERSION RESULTS

The available emissivity data was used in the manner described in Section 3. However, the image data had to be prepared in order to be consistent with the symmetry assumptions of the geometrical model used during the radiance inversion. This data treatment will be discussed in Section 4.1, after which some of the results will be shown in Section 4.2.

### 4.1 Input data

The image data processed by means of the radiance inversion technique described in the previous section, consisted of mid-wave aircraft images recorded at an aspect angle of  $90^\circ$  at four different altitudes, ranging from sea level up to 15 kft. For each altitude, absolute radiance vertical profiles for each resolvable distance behind the aircraft tailpipe were determined, i.e. a vertical profile was determined for each pixel column of an image, as shown in Figure 5. After obtaining these profiles, their maxima were shifted to the centreline of the plume. All profiles were processed in this way in order to obtain average profiles for each distance behind the aircraft tailpipe at each altitude. Figure 6 shows the average, shifted-maximum vertical profiles for the recordings done at sea level. Although it can be seen that the profiles



are relatively symmetrical with respect to their maximum values, the last step in the data smoothing process was to impose symmetry on them by ‘flipping’ the average profiles (inverting the x-axis), and taking the average of these flipped profiles and the original (un-flipped) ones in order to obtain new perfectly symmetrical profiles. These symmetrical profiles are also shown in Figure 6. The averaging of the flipped and un-flipped profiles ensures that the integrated radiance below the profile line remains unchanged. These profiles define four new smoothed, symmetrical radiance images of the plume for each altitude.

Radiance inversion can be applied to each of the four symmetrical profile plumes respectively. For altitudes between measurement altitudes, an interpolation of the symmetrical profiles was done before inversion. Only half a profile was used in the radiance inversion process, due to its symmetry.

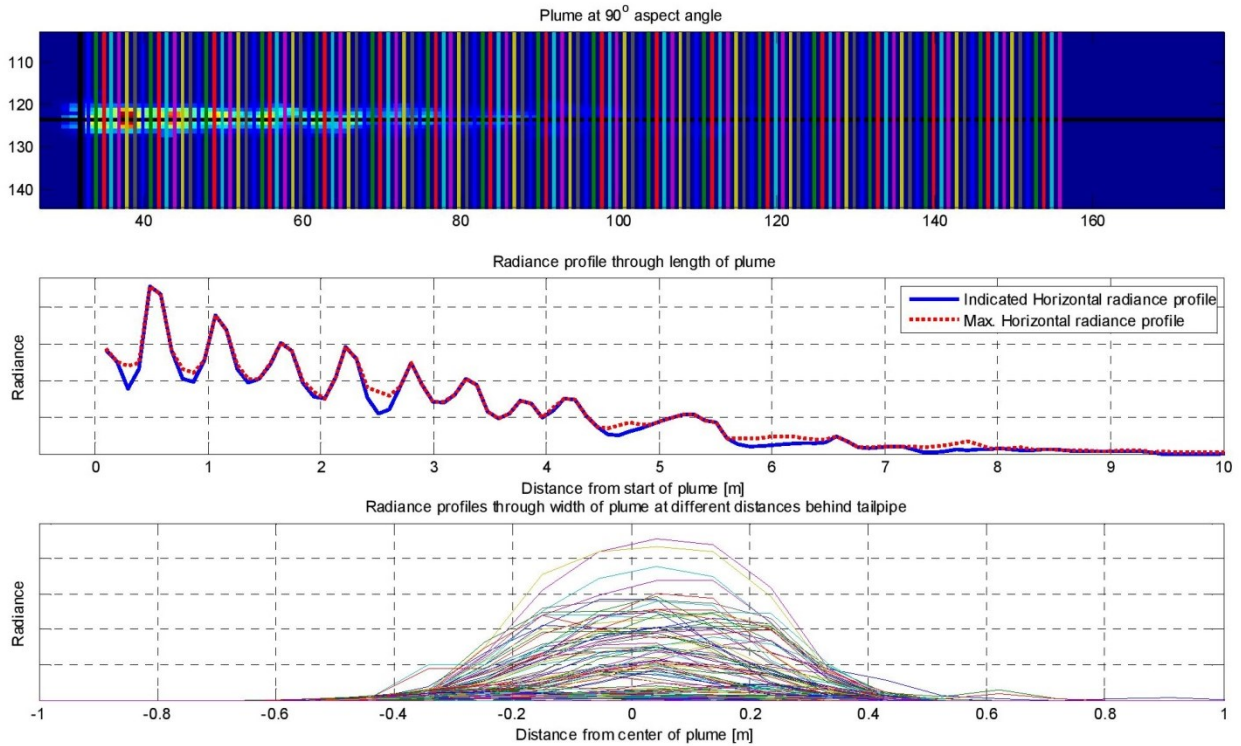


Figure 5. Top Figure: In-flight sea level recording of plume at a 90° aspect angle. The position of a horizontal profile is indicated with a horizontal black line, with its values shown in the Middle Figure. The end of the aircraft tailpipe (aircraft to the left) is indicated with a vertical black line, and the positions of the vertical coloured lines, with their values shown in the Bottom Figure. The spacing between the vertical profiles is exactly one pixel (pixels numbered in Top Figure). Also indicated in the Middle Figure are the maximum radiance values for each vertical profile.

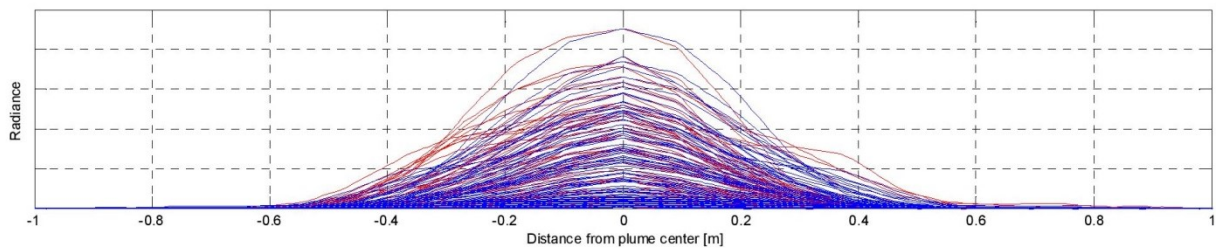


Figure 6. The average vertical profiles at sea level, with their maxima shifted to the zero position, at different distances behind the aircraft tailpipe (red curves). These averages were obtained from all profiles measured at sea level at a 90° aspect angle. Also shown are these average profiles after symmetry was imposed on them (blue curves).



### 4.2 Inverted radiance and temperature

Application of the radiance inversion technique described in Section 3 resulted in the internal blackbody temperatures shown in Figure 7 for the sea level plume. In Figure 8, the temperatures of selected vertical profiles and a horizontal profile through the plume are shown. These internal values can now be used in the generalized model in Section 5.

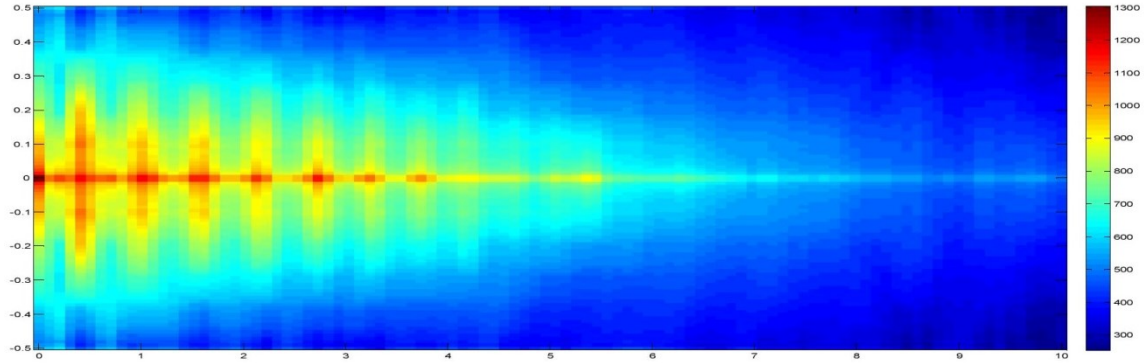


Figure 7. The internal plume temperatures obtained from the radiance inversion process. The x- and y-labels indicate the actual distances [m] but an exaggerated y-axis scale. The temperatures are in units of [K].

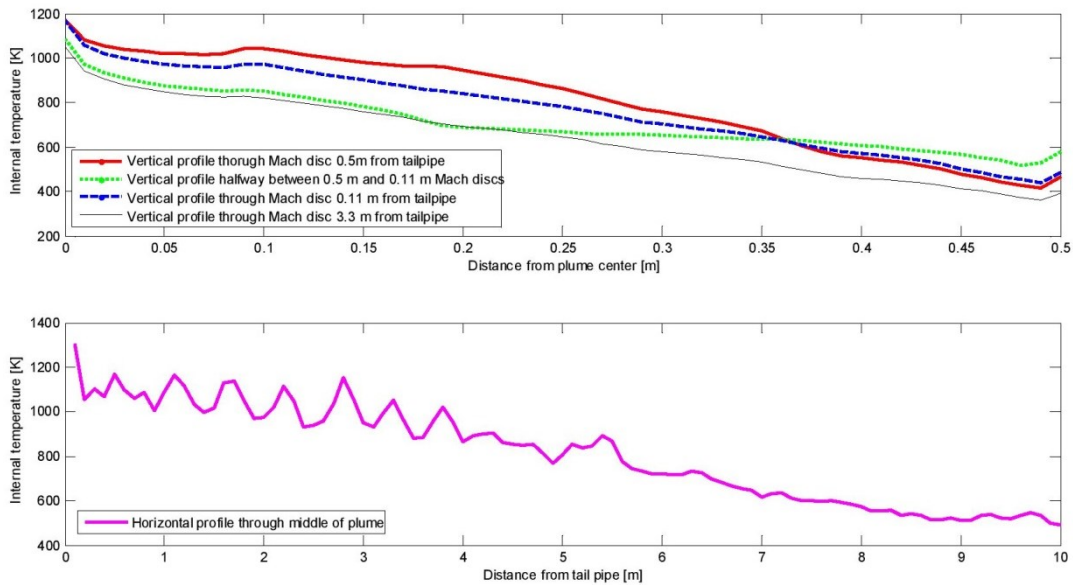


Figure 8. Selected internal plume temperature profiles obtained through radiance inversion.

## 5. GENERALIZED PLUME MODEL

During radiance inversion, the LOSs were all perpendicular with the main axis of the plume. The radiance values should, however, be calculable for aspect angles other than  $90^\circ$  in a model that represents the plume radiance in a simulation environment. The first step in determining the radiance for an arbitrary aspect angle is to parameterize the LOS. Having a description in three-dimensional space of the LOS after parameterization, the second step is to calculate the intersections of this LOS with the boundaries of each annular region and boundary planes of each slice of the plume, so that the distances traversed in each annular region within each slice can be determined. With these new distances, the emissivity and transmission of each segment of the LOS in a specific annular region and plume slice can be calculated.

### 5.1 Parameterization of the LOS

Figure 9a shows the shell of the outer annular region of the geometrical model of the plume with a LOS of arbitrary direction passing through it. The LOS can be parameterized in terms of the parameter  $t$  according to

$$\bar{r}(t) = \bar{a} + t\bar{b}, \quad (21a)$$

i.e.

$$\bar{r}(t) = (a_1 + tb_1, a_2 + tb_2, a_3 + tb_3), \quad (21b)$$

where vector  $\bar{a}$  points to the intersection of vector  $\bar{r}$  with the  $x$ - $z$  plane and vector  $\bar{b}$  is specified by

$$\bar{b} = \|\bar{b}\|(\sin\phi\cos\theta, \sin\phi\sin\theta, \cos\phi), \quad (22)$$

with  $\theta$  being the angle with the  $x$ - $z$  plane and  $\phi$  the angle with the  $z$ -axis as indicated in Figure 9b. Combining Equations 21 and 22 results in

$$\bar{r}(t) = (a_1 + t\sin\phi\cos\theta, a_2 + t\sin\phi\sin\theta, a_3 + t\cos\phi), \quad (23)$$

where  $\|\bar{b}\| = 1$  and from which follows that

$$x(t) = a_1 + t\sin\phi\cos\theta, \quad (23a)$$

$$y(t) = a_2 + t\sin\phi\sin\theta, \quad (23b)$$

$$z(t) = a_3 + t\cos\phi. \quad (23c)$$

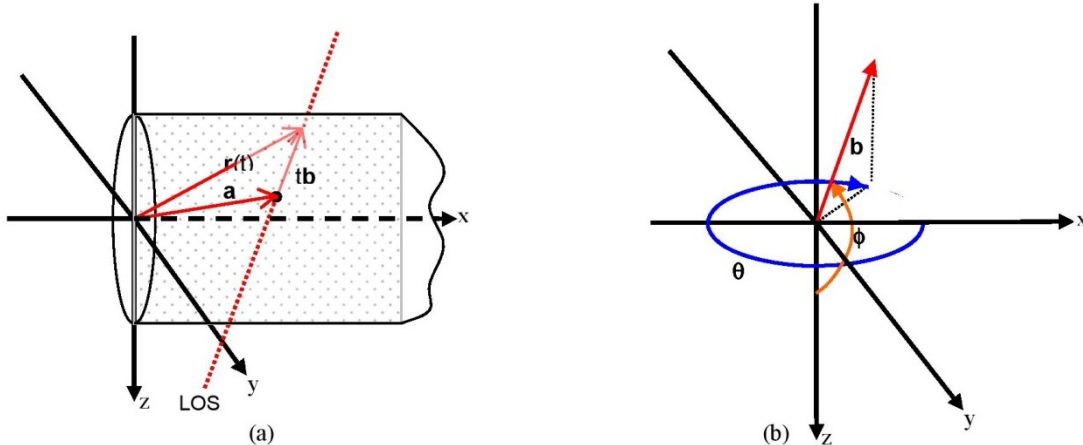


Figure 9. (a) The LOS, presented by vector  $\bar{r}(t)$ , traversing the outer shell of the plume model and intersecting the  $x$ - $z$  plane at position  $\bar{a}$ ; (b) The defining angles of vector  $\bar{b}$ .

### 5.2 Intersection of LOS with annular and slice boundaries

During the radiance inversion when the LOSs were all perpendicular to the main axis of the plume, distances of the LOSs as they traversed each annular region were calculated using the equations given in Section 2 for  $\Delta l_{i,j}$ . However, with a LOS at any different angle, the distances traversed in each annular region will be different as shown in Figure 10.

For a point  $(x(t), y(t), z(t))$  on  $\bar{r}$  to intersect with the surface of a cylinder with radius  $r_c$ , the following conditions must be met:

$$r_c^2 = y(t)^2 + z(t)^2, \quad (24)$$

$$0 \leq x(t) \leq L, \quad (25)$$

where  $L$  is the length of the cylinder. On substitution of Equations 23b and 23c into Equation 24, one obtains

$$r_c^2 = a_2^2 + a_3^2 + 2t(a_2 \sin\phi \sin\theta + a_3 \cos\phi) + t^2(\sin^2\phi \sin^2\theta + \cos^2\phi). \quad (26)$$

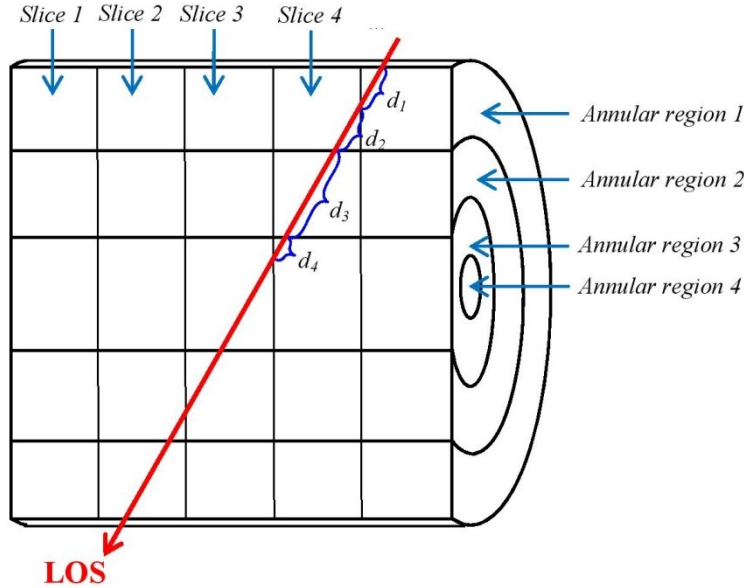


Figure 10. Cross section through geometrical plume model. The LOS of the observer is shown, with the distances that it traverses through each annular region within each slice.

This equation is of the form  $at^2 + \beta t + \gamma = 0$ , with  $\alpha = \sin^2\phi \sin^2\theta + \cos^2\phi$ ,  $\beta = 2(a_2 \sin\phi \sin\theta + a_3 \cos\phi)$  and  $\gamma = a_2^2 + a_3^2 - r_c^2$ . The solution to Equation 26 is therefore

$$t^* = \frac{-\beta \pm \sqrt{\beta^2 - 4\alpha\gamma}}{2\alpha}. \quad (27)$$

Replacement of  $t$  in Equation 23 with the calculated values of  $t^*$  yields the points of intersection of the LOS with the cylinder of radius  $r_c$ . These intersection points must be calculated for all the radii of the different annular regions.

The points of intersection of the LOS with the boundary planes of the plume slices are situated at

$$t^* = \frac{\bar{x} - a_1}{\sin\phi \cos\theta}, \quad (28)$$

where  $\bar{x}$  is the array of the  $x$ -values of the slice boundary planes, which are all parallel to the  $y$ - $z$  plane. Replacement of  $t$  in Equation 23 yields the intersection points of the LOS with the slice boundary planes.

After calculating the values of  $t^*$  according to Equations 27 and 28 and ordering in increasing order, i.e.  $t^* = [t_1^*, t_2^*, \dots, t_n^*]$  with  $t_1^* < t_2^* < \dots < t_n^*$ , all intersection points of the LOS with the boundaries of the annular regions and slices, i.e.  $\{x(t_1^*), y(t_1^*), z(t_1^*)\}, \dots, \{x(t_n^*), y(t_n^*), z(t_n^*)\}$  can be calculated. The distances between the intersection points,  $d_1, \dots, d_n$ , can be directly calculated from this and be used in the calculation of the transmittance and emissivity values associated with them.



## 6. GENERALIZED PLUME MODEL RESULTS

The plume model was implemented in the Matlab<sup>9</sup> programming language and could successfully be run for arbitrary aspect angles. Figure 11 shows the modelled plume in the spectrally integrated MWIR band at sea level for various aspect angles. The upper part of each of the subfigures shows the image of the modelled plume, while the lower part shows the radiance profile going horizontally through the middle of the plume. As the aspect angle increases, the intensity increases as well as the radiance profile. At an aspect angle of 40° the Mach discs start appearing; at larger angles the Mach discs become clearly visible. The obscuration of the tail pipe exit plane formed part of the plume modelling.

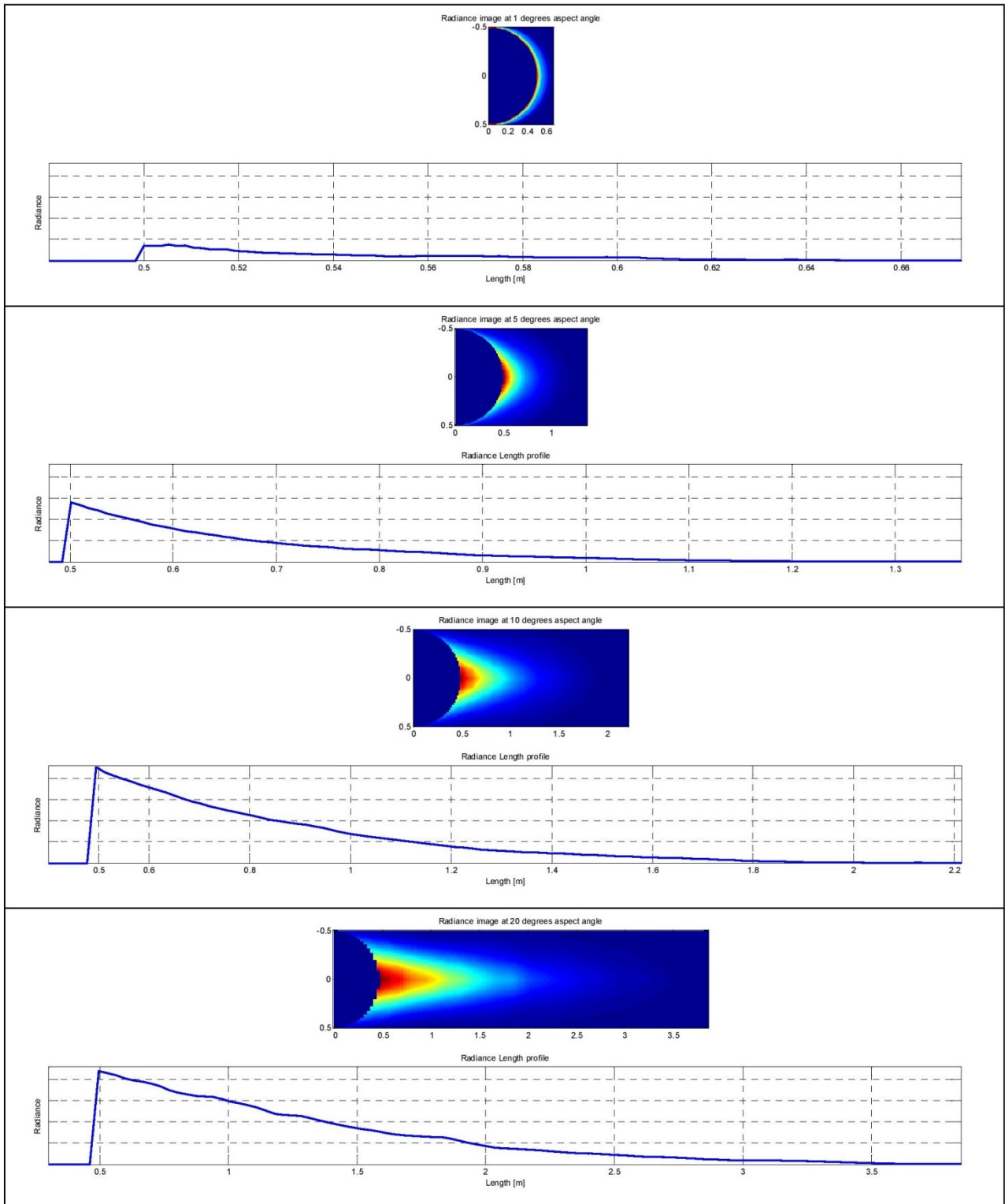
In Figure 12 the absolute intensities in the MWIR band obtained from the flight test measurements are compared to the modelled plume intensities. Unfortunately, no measurements are available for aspect angles between 20° and 90°. At an aspect angle of 10°, the measured intensities do not follow the same clear decreasing trend as a function of altitude than at the rest of the aspect angles. This is likely due to measurement inaccuracies at this aspect angle, and it is difficult to make any statement with regards to the difference between the modelled and measured values.

At 90°, a substantial difference between the measured and modelled intensities at 3 kft exists. However, at this angle, the model only gives back exactly the input data that were supplied during the radiance inversion process. This intensity difference must therefore, in part, be attributed to the manipulation of the measured plume input data that was done to prepare the data for the inversion process. Another explanation can be related to the fact that not exactly the same recorded data frames were used in the radiance inversion input as in the determination of the measure intensity.

## 7. CONCLUSION

The goal with the radiance inversion technique presented in this paper is to enable the creation of an infrared aircraft plume model, which is adequate for use in simulations of a missile-aircraft engagement. Although the inversion does not involve an in-depth physics study of the radiation processes within a plume, it is nonetheless considered to be based on a reasonable scientific method moulded around the available data. The model created was verified against measurements and it appears to be reasonable.





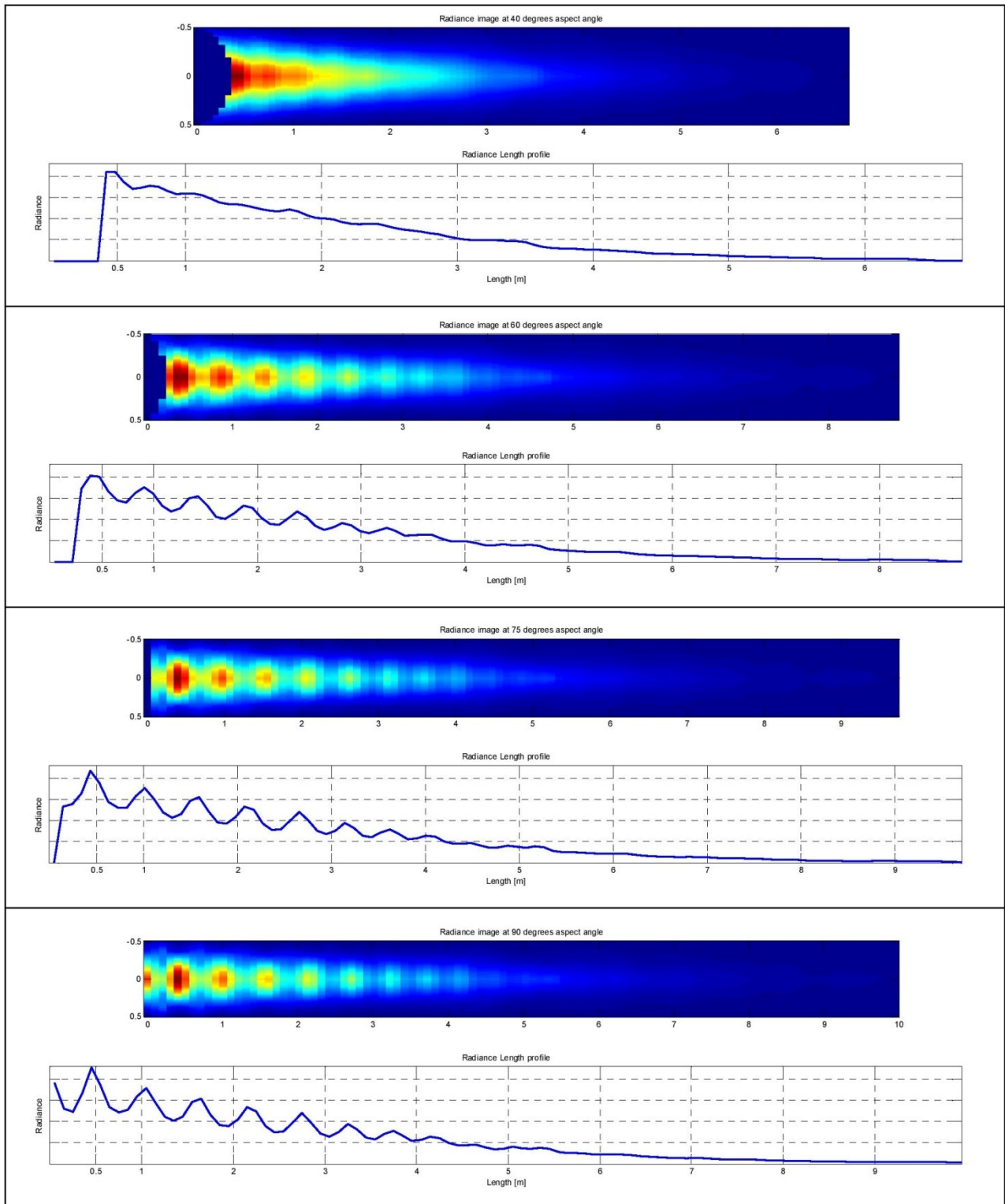


Figure 11. Modelled MWIR plume radiance images and length profiles for sea level altitude.

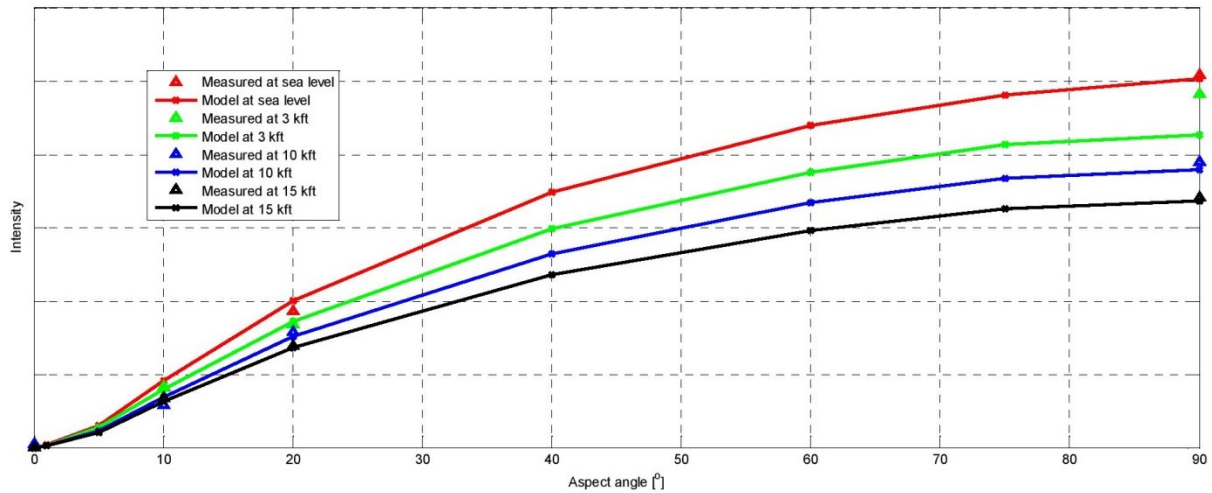


Figure 12. Comparison of the MWIR plume intensities ( $[W.sr^{-1}]$ ) at different altitudes as a function of aspect angle of the aircraft.

### ACKNOWLEDGEMENTS

The author wishes to express his sincere appreciation towards the Denel Dynamics management for making this work possible.

### REFERENCES

- [1] Willers, M. S., "Key considerations in infrared simulations of the missile-aircraft engagement", Proc SPIE 8543 (2012).
- [2] Retief, S. J. P., Smit, P., Dreyer, M. M., "Mid-Wave infrared characterization of an aircraft plume", Proc IEEE Saudi International Electronics, Communications and Photonics Conference (SIEPC) (2011).
- [3] Chandrasekhar, S., [Radiative Transfer], Dover Publications, Inc., New York, 5-10 (1960).
- [4] Qing, Y. E., Xiaoquan, *et al.*, "An Inversion of Plume Gas Concentration Distribution Based on Multivariate Regression Analysis", Proc. SPIE 7511 (2009).
- [5] Tourin, R. H., [Spectroscopic Gas Temperature Measurement – Pyrometry of Hot Gases and Plasmas], Elsevier Publishing Company, Chapter 5 (1966).
- [6] Griem, H. R., [Plasma Spectroscopy], McGraw-Hill Book Company, Chapter 7 (1964).
- [7] Wormhoudt, J., [Infrared Methods for Gaseous Measurements – Theory and Practice], Marcel Dekker, Inc., Chapter 5 (1985).
- [8] Harley, J. L., Rolling, A. J., Wisniewski, C. F. and Gross, K. C., "Spatially resolved infrared spectra of F109 turbofan exhaust", Proc. SPIE 8354, 83540H-1 – 83540H-10 (2012).
- [9] The Mathworks, Matlab Release 2011b (2011).

## CHAPTER 6      OBTAINING THE MEASURING INSTRUMENT'S SPECTRAL RESPONSE

### 6.1 INTRODUCTION

The measurement equation, as supplied in the sections of Chapter 4, forms the starting point of the work presented in this chapter. The emphasis now is, however, not on obtaining the source radiance of the object being observed by the instrument, but on obtaining the information required by the measurement equation of the instrument itself. The main goal of the article in Section 6.2 [6] is to show that the spectral response of a wide-band infrared measuring instrument, as required in the infrared measurement equation, can be determined from measurements of a source with known emission spectra by means of the devised inversion technique. A second goal is to illustrate the requirements for successfully applying the technique in practice. Although this work points towards some strict requirements in terms of measurement accuracy, which might not always be possible in practice, the present author believes that an avenue is opened with this research towards the investigation of more techniques and methods for adequately addressing the successful retrieval of the spectral response of real instruments.

The measurements in this work are made of a blackbody over the shortest possible distance so that for the measurement equation, i.e. Equation (1) in either Sections 4.2 or 4.3, the following assumptions can be made:

- There are no losses in the blackbody radiation when propagating through the atmosphere over the short distance between the blackbody and instrument, i.e.  $\tau_{atm} = 1$ , so that the first term contains only the instrument spectral response and the blackbody radiance.
- The blackbody is not transparent, i.e.  $\tau_{trg} = 0$ , so that the second term can be set to zero.
- The target area of the blackbody has no reflectivity, i.e.  $\rho_{trg} = 0$ , so that the third term can be set to zero.



- The atmospheric path radiance resulting from the short distance of atmosphere between the blackbody and instrument is negligible, i.e.  $L_{p_{r \rightarrow 0}} = 0$ , so that the fourth term can be set to zero.

The resultant measurement equation, given by Equation (1) in Section 6.2, forms the basis upon which the technique for resolving the spectral response of a wide-band infrared instrument rests. The initial motivation for investigating the possibility of such an inversion technique was born from the frustration of the frequent struggles in obtaining the spectral response of wide-band infrared cameras from their manufacturers.

## **6.2 PUBLICATION – A TECHNIQUE FOR RESOLVING THE SPECTRAL RESPONSE OF A WIDE-BAND INFRARED MEASURING INSTRUMENT FROM MEASUREMENTS WITHOUT THE NEED FOR A SPECTRALLY TUNEABLE RADIATION SOURCE**

This article, with the developed technique reported therein, was the sole work of the present author. The article was published in the peer reviewed journal *Infrared Physics and Technology* [6].



Contents lists available at ScienceDirect

## Infrared Physics & Technology

journal homepage: [www.elsevier.com/locate/infrared](http://www.elsevier.com/locate/infrared)



Regular article

### A technique for resolving the spectral response of a wide-band infrared measuring instrument from measurements without the need for a spectrally tuneable radiation source



Stephanus Johannes Paulus Retief

University of Pretoria, Hatfield, South Africa and Denel Dynamics, P.O. Box 7412, Centurion 0046, South Africa

#### ARTICLE INFO

##### Keywords:

Infrared measurements  
Spectral response  
Fredholm integral of the first kind  
Tikhonov regularization

#### ABSTRACT

A technique is presented in which the spectral response of a wide-band infrared measuring instrument is obtained by means of calibration type measurements of a blackbody at various temperature settings and the application of a mathematical technique to these measurements. Successful application of the developed technique is enabled by Tikhonov regularization, which ensures a stable solution to the ill-posed problem of the Fredholm integral equation of the first kind describing the blackbody measurements made by the instrument. The quality of the solution strongly depends, however, on the accuracy of the measurements and the accuracy of the modelled spectrum in describing the emission from the blackbody source.

The technique is studied by means of an application to modelled results of instrument measurements, and is then applied to actual measurements made with an infrared camera. It is shown that the technique can, in the absence of specific manufacturer supplied information of the instrument and specialized equipment, be an alternative to the theoretical calculation of the instrument response spectrum or to an experimental determination of the instrument spectral response during which measurements are made of a spectrally tuneable radiation source like a blackbody and monochromator.

#### 1. Introduction

In the field of radiometry, the infrared characteristics of an object of interest are inferred from radiation measurements done with calibrated instruments like cameras and spectrometers [1]. Such instruments, which are in common use in the military environment, usually function in one of the atmospheric windows in which attenuation by the atmospheric constituents allows a reasonable distance of propagation of the infrared radiation before total extinction. These windows, or spectral bands, are loosely defined as near-infrared (NIR, 0.75–1.4  $\mu\text{m}$ ), short-wave infrared (SWIR, 1.5–2.5  $\mu\text{m}$ ), medium-wave (or mid-wave) infrared (MWIR, 3–5  $\mu\text{m}$ ) and long-wave infrared (LWIR, 8–12  $\mu\text{m}$ ) [2]. The optical systems associated with these instruments, typically composed of lenses, reflective elements, windows, filters and anti-reflection coatings, need to be transparent (or fully reflective) to the infrared wavelengths within one (or several) of the mentioned spectral bands in order for the radiated energy from the object of interest to reach the detector. The detector itself needs to be designed and manufactured as to be sensitive in the required wavelength band.

In practice, no optical system is fully transparent at all wavelengths

[3] within a spectral band, and the sensitivity of the widely used infrared photon detectors can also be assumed to have a non-flat spectral response to incoming radiation [4]. The response of the other main type of detectors in common use, i.e. thermal detectors, is generally wavelength independent [4], but spectral selectivity is also introduced to this type of detector whenever a surface coating with selective spectral absorptivity properties is applied to the detector. The combined effects of spectral selectivity in the optical system transmission and detector response result in the instrument, as a whole, having a non-flat spectral response to any radiation measured by it.

The influence of a non-flat instrument spectral response can largely be factored out by a calibration procedure. During this procedure an infrared source, like a blackbody with known Planck distributions of radiated energy at different temperature settings, is used as the object of interest to be measured by the instrument. The output signals of the instrument can then be correlated with the known temperature or radiance values of the blackbody being measured, so that the non-flat spectral instrument response is compensated for. In such a way, the instrument signal obtained from measuring a blackbody of unknown temperature can be inferred from the calibration information. However,

E-mail address: [paul.retief@deneldynamics.co.za](mailto:paul.retief@deneldynamics.co.za).

URL: <https://www.deneldynamics.co.za>.

<https://doi.org/10.1016/j.infrared.2018.06.004>

Received 19 November 2017; Received in revised form 27 May 2018; Accepted 3 June 2018

Available online 06 June 2018

1350-4495/© 2018 Elsevier B.V. All rights reserved.



for objects with non-blackbody spectra, such as spectrally selective emitters like gases, or grey bodies with constant emissivities smaller than one, the inferred temperature will most probably not agree with the object's thermodynamic temperature and is called the radiometric temperature (see [5] for the definitions of several types of radiometric temperatures). Moreover, for measurements during which the infrared signature of an object must be determined over a distance for which the atmospheric and other environmental contributions to the observed radiation is non-negligible, the measured radiation (and associated radiometric temperature), digress even more from the true value of that of the object of interest. In order to correctly model the radiance measured by the instrument, or to attempt to infer the source radiance value of the object of interest during data reduction by correcting for exogenous influences on the measurement, the instrument spectral response is required [6].

In general, the instrument spectral response can be determined by one of two methods:

- Theoretically by having information from the manufacturer in hand, like the detector responsivity as calculated from the spectral quantum efficiency of a photon detector [7], the spectral absorption of the surface of a thermal detector and the spectral transmission of the optical system and any filter or coating forming part of it.
- Purely experimentally with the use of a spectrally tuneable radiation source, like an infrared source and monochromator of some sort, capable of generating infrared radiance within a narrow wavelength band of which the centre frequency can be swept through the spectral wide-band (NIR, SWIR, MWIR or LWIR) in which the instrument operates, e.g. [8].

The first method typically, in practice, suffers from incomplete or unavailable information. Furthermore, the spectral information supplied by a manufacturer most likely consists only of typical values of quantum efficiency and transmission for a batch of detectors and optical systems, instead of the exact values of the specific component purchased.

The second method can be considered as the preferred method, since any manufacturing deviation from the design norm is automatically apprehended in the measurements. The problem here might be the lack of the appropriate, specialized, and usually costly, equipment. Also, due to the nature of a narrow band radiation source, the amount of radiation energy decreases as the resolution (determined by the width of the tuneable narrow wavelength band) increases, which might present instrument dependent problems related to inadequate sensitivity.

The goal of the research reported on in this article is to present a promising alternative method to the two mentioned traditional methods for determining the spectral response of an infrared measuring instrument. The main idea behind this method is to use only a blackbody, which is a standard piece of equipment in any infrared laboratory, and a very low temperature object for calibration type measurements from which the instrument spectral response can be retrieved after applying an appropriate mathematical technique.

In Section 2.1 the mathematical technique is developed by starting from the basic measurement equation for calibration type measurements. The technique is considered novel in the sense that it demonstrates that it is in principle possible to obtain the instrument spectral response of a wide-band instrument from measurements of a blackbody without the use of a monochromator. However, although the spectral response recovery is in principle possible, it does come with complications arising from the instability of the solution. Fortunately, an attempt can be made to stabilize this type of unstable solution arising from the inversion of ill-conditioned matrices; to this effect, the regularization method of Tikhonov is introduced. After introduction of this stabilization method, the technique is applied in Section 2.2 to synthetically generated measurements, i.e. measurement results with no

measurement errors but with unstable solutions. The behaviour of the technique with the mentioned regularization method is then demonstrated by an investigation into its dependency on the controllable aspects, i.e. controllable parameters, used during the process of obtaining a solution, followed by a discussion of the findings in Section 2.3.

Section 3.1 presents the spectral response of a real instrument, a MWIR camera, as obtained from the two earlier mentioned traditional methods. In order to utilize the proposed technique for obtaining the camera spectral response, it is showed in Section 3.2 how a realistic model of the signal output from the instrument should be constructed before attempting to resolve its spectral responsivity. This model is considered sufficiently generic to be applicable to a wide range of infrared (IR) camera models. The measurement setup of the calibration type measurements is then also described in detail to enable any interested party to replicate these types of measurements. It is then shown that, although it is in principle possible to resolve the spectral response of an instrument by the proposed technique as illustrated in Section 2, a high degree of accuracy are required in the measurements and in the knowledge of the observed object radiance spectrum. The purely experimentally determined camera spectral response (second method described above), considered as an absolute reference, is then used to compare the solutions obtained from the proposed technique against and also to obtain an indication of the required degree of measurement accuracy for the technique to be applied successfully.

Section 4 summarizes the research done and the findings and limitations when applying the proposed technique, with some reflections on possible future research and other applications.

## 2. Technique for resolving the instrument spectral response

### 2.1. Theory

The measurement of an object by an ideal instrument, without any exogenous influences, can be described by the measurement equation (cf. [9])

$$s = \int_{\lambda_a}^{\lambda_b} L_{obj}(\lambda) \mathfrak{R}_L(\lambda) d\lambda, \quad (1)$$

where  $s$  (units of [V] or [A]) is the signal obtained from the instrument as a result of the observed object having a wavelength ( $\lambda$ ) dependent radiance  $L_{obj}(\lambda)$  [ $\text{W} \cdot \text{m}^{-2} \cdot \text{sr}^{-1} \cdot \mu\text{m}^{-1}$ ]. The wavelengths  $\lambda_a$  and  $\lambda_b$  demarcate the spectral band in which the instrument is sensitive to radiation, and  $\mathfrak{R}_L(\lambda)$  is the spectral radiance responsivity of the instrument, which is the ratio of the output of the instrument to that of the spectral radiance of the observed object (units of [(V or A)/( $\text{W} \cdot \text{m}^{-2} \cdot \text{sr}^{-1} \cdot \mu\text{m}^{-1}$ )]). The responsivity can be written as

$$\mathfrak{R}_L(\lambda) = \mathfrak{R}_L(\lambda_0) r(\lambda) = C_{L2s} r(\lambda), \quad (2)$$

where  $C_{L2s} \equiv \mathfrak{R}_L(\lambda_0)$  is the spectral responsivity at the wavelength at which  $\mathfrak{R}_L$  obtains its maximum value, i.e. at wavelength  $\lambda_0$ , so that  $r(\lambda) = \mathfrak{R}_L(\lambda)/C_{L2s}$  forms the normalized spectral responsivity, which are often used in these type of measurement equations (see e.g. [10–12]).  $C_{L2s}$  forms a wavelength independent conversion factor (and therefore removable from under the integration sign in Eq. (1)), which both scales the calculated radiance back to the correct level and also converts it into instrument signal units ( $L$  to  $s$ ), whenever the normalized spectral responsivity  $r$  is used in the measurement equation as is shown later in Eq. (4). The use of  $r$  introduces a simplification in the notation used in the technique under development, with  $r$  containing only the essence of the desired information to be retrieved— the shape of the spectral response and not so much the absolute level of this spectrum.

The object radiance,  $L_{obj}(\lambda)$ , describes all contributions from all sources of radiance reaching the instrument, but in the rest of this section it will be considered to consist only of a blackbody, described by Planck's law



$$L_{bb}(T, \lambda) = \frac{2hc^2}{\lambda^5} \frac{1}{e^{\frac{hc}{\lambda kT}} - 1}, \quad (3)$$

with  $L_{bb}(T, \lambda)$  being the blackbody radiance,  $c$  the velocity of light,  $h$  the Planck constant,  $k$  the Boltzmann constant and  $T$  the temperature of the blackbody. The implied assumption when setting  $L_{obj} = L_{bb}$  in the measurement equation, is that the radiance observed by the instrument is only from this one source having a fixed temperature  $T$  and a constant spectral emissivity of  $\epsilon = 1$ , and that there are no exogenous influences on this blackbody measurement from the atmosphere or any other sources, like the thermal radiation from the camera itself. This assumption will serve in assisting the demonstration of the proposed technique, but will be adapted in Section 3 when real measurements are used in the application of the technique. Eq. (1) can now be rewritten as

$$s(T) = C_{L2s} \int_{\lambda_a}^{\lambda_b} L_{bb}(T, \lambda) r(\lambda) d\lambda \equiv C_{L2s} L_{pn}(T), \quad (4)$$

describing the signal obtained from the measuring instrument when observing a blackbody with temperature  $T$ , for which the radiance spectrum  $L_{bb}(T, \lambda)$  is theoretically known. The peak-normalized radiance [13,14] for the instrument specific  $r(\lambda)$ , as defined in the above equation, is denoted by  $L_{pn}(T)$ . It must be noted that Eq. (4) is a Fredholm Integral equation of the First Kind (IFK) [15–17], which have the generic form  $g(y) = \int_{x_1}^{x_2} K(y, x) f(x) dx$ , where the kernel  $K(y, x)$  is a known function of the two variables  $x$  and  $y$ ,  $f(x)$  is an unknown function to be solved and  $g(y)$  is known for different values of  $y$ , usually obtained from measurements. With the kernel in Eq. (4) being Planck's law, the goal is now to obtain the unknown  $r(\lambda)$ , or  $C_{L2s} r(\lambda)$ , after which the value of  $C_{L2s}$  can also be obtained in a straightforward manner. Note that the  $L_{bb}(T, \lambda)$  kernel is not separable into factors containing only  $T$  and  $\lambda$  respectively, which negates the possibility of removing  $T$  from under the integral sign, thereby complicating any analytical solution.

The first step is to discretize the integral in Eq. (4) by means of a quadrature formula. A closed quadrature formula for numerical integration yields

$$L_{pn}(T) \approx \sum_{j=1}^n w_j L_{bb}(T, \lambda_j) r(\lambda_j), \quad (5)$$

with  $\lambda_1 = \lambda_a$  and  $\lambda_n = \lambda_b$ , where  $w_j$  are the weights associated with the chosen quadrature formula. For equally spaced wavelength intervals  $\Delta\lambda = \lambda_{i+1} - \lambda_i$ , the extended trapezoidal rule [16] prescribes the weights to be  $w_1 = w_n = \Delta\lambda/2$  and  $w_2 = w_3 = \dots = w_{n-1} = \Delta\lambda$ . For each measurement made of a blackbody at a specific temperature  $T_i$ , as is done during calibration of an instrument, Eq. (4) can now be written as

$$s_i = C_{L2s} L_{pn}(T_i) \approx C_{L2s} \sum_{j=1}^n w_j L_{bb}(T_i, \lambda_j) r(\lambda_j) = C_{L2s} \sum_{j=1}^n L_{ij} r_j, \quad (6)$$

where the shorthand  $s_i \equiv s(T_i)$ ,  $L_{ij} \equiv w_j L_{bb}(T_i, \lambda_j)$  and  $r_j \equiv r(\lambda_j)$  is used. Each of  $m$  temperature measurements can be described by Eq. (6), thereby forming a system of equations, which can be written in matrix form as

$$C_{L2s} \begin{bmatrix} w_1 L_{1,1} & w_2 L_{1,2} & \dots & w_n L_{1,n} \\ w_1 L_{2,1} & w_2 L_{2,2} & \dots & w_n L_{2,n} \\ \vdots & \vdots & \ddots & \vdots \\ w_1 L_{m-1,1} & w_2 L_{m-1,2} & \dots & w_n L_{m-1,n} \\ w_1 L_{m,1} & \dots & \dots & w_n L_{m,n} \end{bmatrix} \begin{bmatrix} r_1 \\ r_2 \\ \vdots \\ r_{n-1} \\ r_n \end{bmatrix} = \begin{bmatrix} s_1 \\ s_2 \\ \vdots \\ s_{m-1} \\ s_m \end{bmatrix} \quad (7)$$

If

$$\mathbf{L} \equiv \begin{bmatrix} w_1 L_{1,1} & w_2 L_{1,2} & \dots & w_n L_{1,n} \\ w_1 L_{2,1} & w_2 L_{2,2} & \dots & w_n L_{2,n} \\ \vdots & \vdots & \ddots & \vdots \\ w_1 L_{m-1,1} & w_2 L_{m-1,2} & \dots & w_n L_{m-1,n} \\ w_1 L_{m,1} & \dots & \dots & w_n L_{m,n} \end{bmatrix}, \mathbf{r} \equiv \begin{bmatrix} r_1 \\ r_2 \\ \vdots \\ r_{n-1} \\ r_n \end{bmatrix} \text{ and } \mathbf{s} \equiv \begin{bmatrix} s_1 \\ s_2 \\ \vdots \\ s_{m-1} \\ s_m \end{bmatrix}, \quad (8)$$

the system of calibration measurement equations, given by Eq. (7),

can now be written in a more compact form as

$$C_{L2s} \mathbf{L} \mathbf{r} = \mathbf{s}. \quad (9)$$

The columns of the radiance matrix  $\mathbf{L}$  represent the model space  $\mathbb{R}^n$ , with its dimension  $n$  being determined by the number of wavelengths over which the model (blackbody radiance) is described. The rows of  $\mathbf{L}$  represent the data space  $\mathbb{R}^m$ , with its dimension  $m$  being determined by the number of measurements available. If  $m = n$ , the system is square and an exact solution might exist. If  $m < n$ , the system is under-determined with infinitely many or no solutions, which is not useful in obtaining a unique solution of  $\mathbf{r}$ . If  $m \geq n$ , the system is square or overdetermined and a least-squares (LS) solution can be obtained. In the context of this work, Eq. (7) is considered to represent either a square or an overdetermined system of equations with the number of wavelength nodes  $n$ , at which the blackbody emission (model) values are calculated, being the same or less than the number of blackbody temperatures  $m$ . It, however, makes sense to use the maximum allowable value of the modelling parameter  $n$  without the system being under-determined, so that  $n = m$  is mostly used in the remainder of the work, except where the effect of  $n < m$  will be illustrated later. The aim with a LS solution is to minimize the Euclidian residual vector norm, i.e. it is attempted to obtain

$$\min \|C_{L2s} \mathbf{L} \mathbf{r} - \mathbf{s}\|. \quad (10)$$

The solution for  $\mathbf{r}$  in Eq. (10) is obtained by multiplying both sides of Eq. (9) from the left by the transpose of  $\mathbf{L}$ , i.e.  $\mathbf{L}^T$ , and then multiplying both sides from the left by  $\frac{1}{C_{L2s}} (\mathbf{L}^T \mathbf{L})^{-1}$ , giving the set of normal equations

$$\mathbf{r} = \frac{1}{C_{L2s}} (\mathbf{L}^T \mathbf{L})^{-1} \mathbf{L}^T \mathbf{s} = \frac{1}{C_{L2s}} \tilde{\mathbf{L}}^{-1} \mathbf{L}^T \mathbf{s}, \quad (11)$$

with  $\tilde{\mathbf{L}} \equiv \mathbf{L}^T \mathbf{L}$ .

Eq. (11) has a unique solution whenever matrix  $\tilde{\mathbf{L}}$  is invertible (and  $\mathbf{s} \neq 0$ ) [16]. Unfortunately, IFKs are often extremely ill-conditioned [16], with very unpleasant properties inherent to them [15], and are therefore not easily invertible. It is in fact stated by Wing [15], that "A solution to ... the IFK ... can seldom be obtained in closed form. Frequently, in practical situations, a reliable approximation to the solution cannot even be found ... It is usually necessary to settle for less information than we would like". The author then states that he prefers to rather speak of *resolving*, than *solving*, IFK problems, a preference which will be maintained in this article as far as possible synonymously with the term *recovered*. Wing also states that it is clear from the unboundedness of the inverse kernel and the fact that small changes in the measured data ( $\mathbf{s}$  in this context) may produce "wild" behaviour in the solution ( $\mathbf{r}$ ), that a means must often be found to "tame" this solution function; "Researchers should be quite aware that they have a great deal of control over and responsibility for this taming". The making of subjective judgements and the use of insight, intuition and educated guesses are then stated as necessities in solving IFK problems. Inverse blackbody radiation problems, similar to the one addressed here but for which a different parameter than emissivity is sought, are no different [18,19]. It is the intention to show in this article what is required to tame the spectral response solution function, and to show the degree of success of what can be achieved with error free synthetic data as well as data containing uncertainties from a MWIR camera.

In order to easily diagnose the condition of  $\tilde{\mathbf{L}}$  (i.e. how invertible it is), the singular value decomposition (SVD) technique is firstly be used to factor  $\mathbf{L}$  (being an  $m \times n$  matrix) into an  $m \times m$  orthogonal matrix  $\mathbf{U}$ , an  $n \times n$  diagonal matrix  $\mathbf{D}$  having singular values  $d_i$  on the diagonal and the transpose of an  $n \times n$  orthogonal matrix  $\mathbf{V}$  [16], i.e.

$$\mathbf{L} = \mathbf{U} \mathbf{D} \mathbf{V}^T. \quad (12)$$

The SVD of  $\mathbf{L}$  then allows easy calculation of the condition number,  $C$ , of  $\tilde{\mathbf{L}}$  since



$$C(\tilde{L}) = \frac{d_{max}^2}{d_{min}^2}, \quad (13)$$

where  $d_{max}$  and  $d_{min}$  are the largest and smallest singular values amongst  $d_i$  respectively. This condition number assists in determining the behaviour of  $\tilde{L}$  upon inversion – if  $C = \infty$ , the matrix is singular; if  $C \gg 1$  (not infinite) the matrix is ill-conditioned; if  $C$  is closer to one, the matrix is well-conditioned [15,16,20].

The approach towards the stable inversion of  $\tilde{L}$  in this work is by means of the regularization method of Tikhonov [15,17,19]. In this method, the minimization of the residual vector norm in Eq. (10) is replaced by the penalized LS problem

$$\min\{\|C_{L2s}Lr-s\|^2 + \alpha \|C_{L2s}r\|^2\}, \quad (14)$$

i.e. solutions of large norm  $r$  is now penalized, with the scalar  $\alpha > 0$  being called the regularization parameter. The first term, when small, guarantees that  $r$  is ‘nearly’ a LS solution, while the second term tends to damp out instabilities in  $r$  [19]. The balance between the two terms, i.e. the normal LS solution of  $r$  and the damping of instabilities in  $r$ , is determined by the value of  $\alpha$  (some literature uses  $\alpha^2$ ). This regularized version of Eq. (10) now represents a well-posed problem from which a well behaved solution should be obtainable. The LS solution for Eq. (14) is

$$r_\alpha = \frac{1}{C_{L2s}}(\tilde{L} + \alpha I)^{-1}L^T s, \quad (15)$$

where  $I$  is an identity matrix with the same dimensions as  $\tilde{L}$ . The solution is unique for a specific value of  $\alpha$  and is called the Tikhonov approximation to  $L^\dagger s$ , the minimum norm solution of the normal equations, where  $L^\dagger$  is the Moore-Penrose generalized inverse of  $L$  [19]. It can be seen that Eq. (15) is identical to Eq. (11), except for  $\tilde{L}$  which is now replaced by  $\tilde{L} + \alpha I$ , i.e. the scalar value  $\alpha$  was added to all elements on the diagonal of  $\tilde{L}$ .

Substitution of Eq. (12) into Eq. (15) results in the SVD implementation of the Tikhonov regularization [17]

$$r_\alpha = \frac{1}{C_{L2s}}V(D^T D + \alpha I)^{-1}D U^T s. \quad (16)$$

It was found in the work of Section 2.2 that the above SVD version of the Tikhonov regularization results in more stable solutions than Eq. (15) when  $\alpha \rightarrow 0$ , and was therefore used in this work.

The  $\alpha$  values added to the diagonal elements of  $D^T D$  in Eq. (16), stabilizes the solution of  $r_\alpha$  by improving the condition number of the matrix to be inverted, which is now [20]

$$C(\tilde{L} + \alpha I) = \frac{d_{max}^2 + \alpha}{d_{min}^2 + \alpha} \quad (17)$$

It can be seen that as  $\alpha \rightarrow 0$ , Eq. (15) approaches its original form of Eq. (11) and a more accurate solution should be reached. This is, however, at the cost of numerical stability of the solution as can be seen from Eq. (17) which approaches Eq. (13) when  $\alpha \rightarrow 0$ , so that a compromise between an accurate solution for  $r_\alpha$  with small  $\alpha$ , lying close to an erratic solution (i.e. ill-conditioned), and a less accurate solution for  $r_\alpha$  with larger  $\alpha$ , being more stable (i.e. well-conditioned), exists (cf. [17,21]).

If  $C_{L2s}$  is not known, Eq. (16) can be rewritten as

$$C_{L2s}r_\alpha = V(D^T D + \alpha I)^{-1}D U^T s \quad (18)$$

and  $r_\alpha$  can be obtained by normalizing the solution obtained on the right hand side of Eq. (18) with respect to its maximum component, i.e. by dividing by  $\max(C_{L2s}r_\alpha)$ .

The optimal value of  $\alpha$  can be determined by visual inspection of the results (visual inspection is also used by Wing [15] to determine the best solution) – the value of  $\alpha$  can be continually decreased up to the point where the solution starts to appear erratic; the optimal  $\alpha$  value would be that used in obtaining the solution that just precedes the start

of the erratic behaviour. Two noticeable, more formal methods for optimal  $\alpha$  value determination are that of the Discrepancy Principle, which connects the  $\alpha$  determination with the error level of the data (if known) [17,19,22], and the L-curve method [17,22], which requires no knowledge of the error/noise level of the data. In the L-curve method, solutions must first be calculated for a range of  $\alpha$  values,  $\alpha_k$ , with  $k$  the index referring to a specific  $\alpha$  value in the range, so that a range of solutions  $r_{\alpha_k}$  is obtained. The values of the logarithm of the residual norm  $\|C_{L2s}Lr_{\alpha_k}-s\|$ , appearing in the first term of Eq. (14), is plotted against the logarithm of the solution norm  $\|C_{L2s}r_{\alpha_k}\|$ , appearing in the second term of Eq. (14), which then typically forms an L-shaped curve. This L-curve displays the compromise between the minimization of the residual norm (good LS solution) and the solution norm (damping of instabilities). The optimal  $\alpha$  value is the specific  $\alpha$  value used in the calculation of the data point situated in the corner of the L-curve, defined as the point on the curve that has maximum curvature. The selection of the corner data point on the L-curve can be done manually or an attempt can be made to calculate its position – a discussion by Hansen on the difficulties involved in computing the point of maximum curvature can be found in [22]; the manual method is used and illustrated in the subsequent sections.

## 2.2. Spectral response recovery from modelled measurements

The following aspects/parameters are controllable during the design and setup of the measurement equation, Eq. (9), and the application of the penalized LS solution, Eq. (15) (and the subsequent SVD implementation thereof as given in Eq. (16)), for resolving the spectral recovery:

1. The number of temperature measurements,  $m$  ( $T_i$ , with  $i = 1 \dots m$ ), or equivalently the temperature difference  $\Delta T$  between temperature values over a given temperature range. The temperature difference, however, needs not to be constant.
2. The temperature range covered by the measured  $T_i$ , [ $T_i$ ,  $T_m$ ].
3. The number of wavelength nodes,  $n$  ( $\lambda_j$ , with  $j = 1 \dots n$ ), or equivalently the wavelength difference  $\Delta \lambda$  between equally spaced wavelength values. The wavelength difference needs to be constant when the Trapezoidal quadrature rule is used in the numerical integration.
4. The wavelength range/band covered by  $\lambda_j$ , [ $\lambda_1$ ,  $\lambda_n$ ], over which the blackbody spectrum is modelled.
5. The value of  $\alpha$ .

The first two parameters are measurement parameters which must be decided on during the planning of a measurement session, while the following two parameters are modelling parameters which must be fixed before it is attempted to resolve the spectral response with the technique outlined in Section 2.1. The last parameter,  $\alpha$ , is the solution regularization parameter which must also be fixed before the actual application of Eq. (16). The dependency of the technique on these parameters will now be demonstrated by making use of modelled ‘synthetic’, noise free values for  $s$  containing no measurement uncertainties. These values are obtained by first calculating  $L$  in Eq. (8) by using Eq. (3) and the weights prescribed by the Trapezoidal rule, after which  $L$  is multiplied an arbitrarily designed normalized response spectrum  $r$  to obtain  $Lr$ . In order to obtain the right hand side of Eq. (9), the value of  $C_{L2s}$  is chosen to be  $C_{L2s}=1/\max(Lr)$  so that vector  $Lr$  is normalized by its maximum value with the convenient effect that the components of  $s$  is scaled between zero and one over the covered temperature range. Note the implicit assumption that  $s$  is directly proportional to  $L_{pn}$ . For these, and all other calculations in this work, the Matlab® software package (version 9.0.0.341360 - R2016a) was used on a 64 bit personal computer. The aspects influencing the calculation of  $L$  and the impact thereof on the exact values of  $L_{pn}$  as obtained from  $Lr$  will firstly be discussed, before it is attempted to resolve  $r$  from only  $L$  and the fabricated  $s$ .

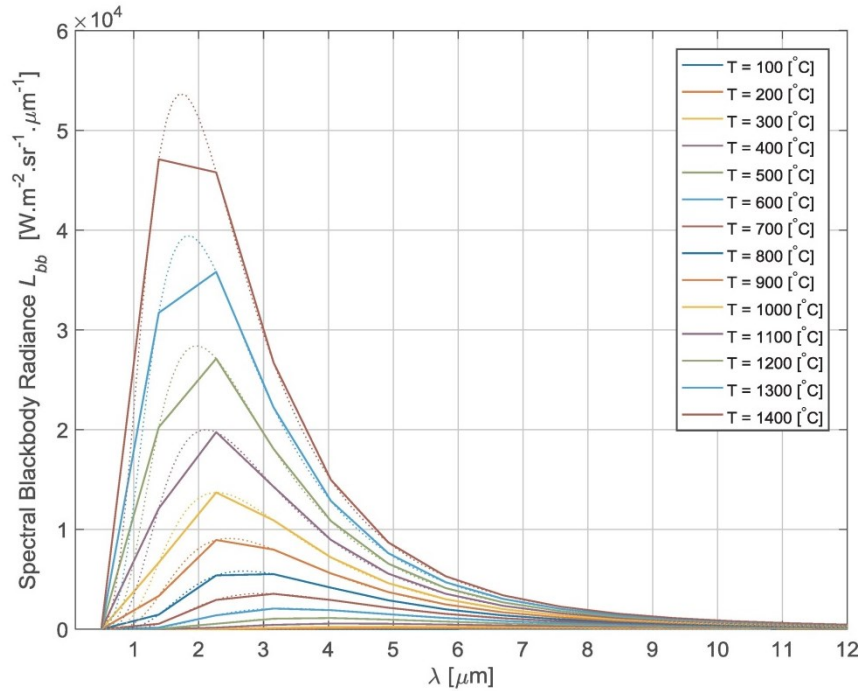


**Fig. 1.** Illustration of blackbody spectra over 0.5–12 $\mu\text{m}$  for different temperatures. It can be seen how the low resolution spectra with  $n = 14$  and  $\Delta\lambda = 0.9\mu\text{m}$  (solid lines) deviates from the more accurate high resolution spectra  $n = 116$  and  $\Delta\lambda = 0.1\mu\text{m}$  (dotted lines), especially around the peak of each spectrum associated with the higher temperatures.

Fig. 1 shows the blackbody spectra  $L_{BB}(T, \lambda)$ , calculated from Eq. (3), for a set of  $m = 14$  temperatures  $T = \{100, 200, \dots, 1400\}$  °C. The modelled low resolution spectra, with  $n = m = 14$  wavelength nodes having resolution of  $\Delta\lambda \approx 0.9 \mu\text{m}$ , compared to the high resolution spectra with  $n = 116$  wavelength nodes with resulting resolution of  $\Delta\lambda = 0.1 \mu\text{m}$ , clearly show the deviation of the lower resolution spectrum from the more accurate, smoother high resolution spectra. This deviation is especially obvious close to the peak value associated with each blackbody temperature (described by Wien's displacement law). It should therefore come as no surprise that the areas under the respective curves might differ and the integral of the high resolution curve would be more accurate than the integral of the low resolution curve for a blackbody of specified temperature. The implication is that the value of  $n$ , and therefore the value of  $\Delta\lambda$ , would have an impact on the calculation of a numerical integral of  $L_{bb}$  in Eq. (3) over a specified wavelength range. The value of  $n$  therefore impacts on the calculation of the accuracy of the numerical integral given by Eq. (5) – the parameter  $n$  should be large enough in order to model the measured signal with adequate accuracy.

Fig. 2 shows the peak-normalized 3–5  $\mu\text{m}$  band radiance modelled 'calibration' curves for different values of  $m$ , with  $n = m$  in each instance, calculated with Eq. (5) for a normalized spectral responsivity  $r(\lambda)$  having a flat spectral response with value of one over 3–5  $\mu\text{m}$  and zero response outside this region (this spectral block response is shown in the graphs of Fig. 4 by a thick black curve). The smoothness of each curve increases as the number of data points defining the curve, i.e. the number of chosen temperatures  $m$  in the 100–1400 °C temperature range, increases – the least smooth curve is for  $m = 11$ , while the smoothest curve is for  $m = 1301$ . Furthermore, as noted in the previous paragraph, the accuracy of the calculations using Eq. (5) increases as the number of wavelength nodes  $n$  increases, so that, with  $n = m$ , the accuracy of each curve increases as the number of temperatures  $m$  increases. It can be seen that as  $m$  increases, the different curves converge towards and settles on the curve with the highest value of  $m$ ,

i.e. the curve with 1301 temperature values with  $\Delta T = 1$  °C and an accompanying number of 1301 wavelength nodes.

It should be noted that the accuracy of the curves in Fig. 2 is, besides being influenced by  $m$ , also influenced by the specific wavelength range/band of interest as covered by  $[\lambda_1, \lambda_n]$  and as imposed by  $r(\lambda)$ , since for the same  $n$  and  $\Delta\lambda$  used in the calculations, a calculated value of  $L_{pn}(T_i)$  at a specific  $T_i$  can be more accurate in one wavelength range than in another, e.g. the calculated  $L_{pn}$  at a high value of  $T_i$  is more accurate in the 3–5  $\mu\text{m}$  band than in the 1–3  $\mu\text{m}$  band. This is due to the larger approximation errors (as touched on earlier) of the numerical integral around the peak radiance values, which are situated in 1–3  $\mu\text{m}$ ; this can easily be gathered by comparison of the solid and dotted blackbody curves for high temperatures show in Fig. 1 in this band. It can be said that above some value of  $n(=m)$ , the values of  $L_{pn}$  would be adequately modelled in a specific wavelength band for a specific response spectrum.

Fig. 3 shows the relationship between the modelled and  $L_{pn}$  values as calculated by Eq. (6) for the 3–5  $\mu\text{m}$  block response and temperature values used in Fig. 1 for the case when  $m = 14$  (with  $n = m$ ), i.e. for  $T = \{100, 200, \dots, 1400\}$  °C. The relationship is ideal in the sense that is directly proportional to  $L_{pn}$ , as can be gathered from Eqs. (6) and (9), with no noise threshold or any non-linearities present in  $s$ . For cases where  $m > 14$ , as will be used later in resolving  $r$ , the gradient of the straight line fit to the data points will be different to the one shown in the figure due to the improved accuracy of the calculated  $L_{pn}$  values.

Having gained some insight into the importance of the role played by the measurement parameter  $m$  (and the associated  $\Delta T$ ) and the modelling parameters  $n$  (with associated  $\Delta\lambda$ ) and wavelength band  $[\lambda_1, \lambda_n]$  in setting up the measurement equation given by Eq. (9), the dependency of the recovery technique, as condensed by Eq. (16) or (18), on these as well as the remaining parameters of  $\alpha$  and temperature range  $[T_i, T_m]$ , will now be demonstrated; in this respect, Fig. 4 shows the results (to be discussed) of various spectral response recoveries in which different values of the mentioned parameters were used, given



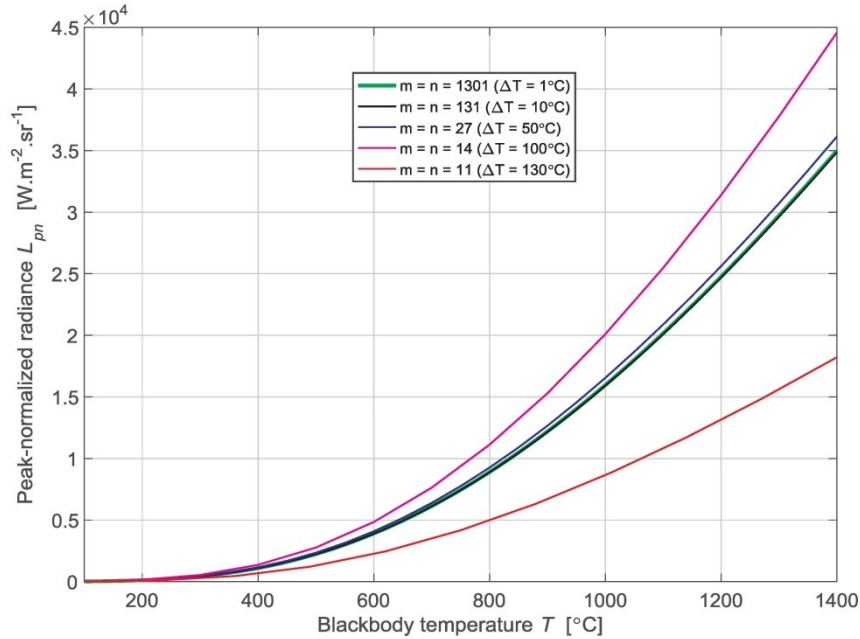


**Fig. 2.** The peak-normalized radiance as a function of blackbody temperature for the block spectral response over 3–5 μm shown in Fig. 4, i.e. calibration curves. The curves were calculated using different numbers of blackbody temperatures,  $m$ , and wavelength nodes,  $n$ , although  $n$  was chosen so that  $n = m$ . Only straight line interpolation between data points was used in plotting these curves.

only the  $s$  and  $L$  values (as calculated from the mentioned 3–5 μm block response) as input. Although the value of  $C_{L2s}$  was considered to be unknown, the value of  $r_a$  could be obtained in each instance by normalizing the vector calculated on the right hand side of Eq. (18) by its largest component.

To start off with, calibration measurements were modelled for blackbody spectra over the temperature range 100–1400 °C with

$\Delta T = 100$  °C. The number of wavelength nodes was set equal to the number of temperatures, i.e.  $n = m$ , with  $m = 14$  and therefore  $\Delta\lambda \approx 0.9$  μm over a wavelength range of  $\lambda = 0.5$ –12 μm (the applicable calibration curve, with  $\Delta T = 100$  °C and  $m = n = 14$ , is shown in Fig. 2). The characteristics of the Tikhonov approximation towards the spectral response recovery for these setup parameters can be observed as a function of  $\alpha$  in Fig. 4a – at the relatively large value of  $\alpha = 1$  the

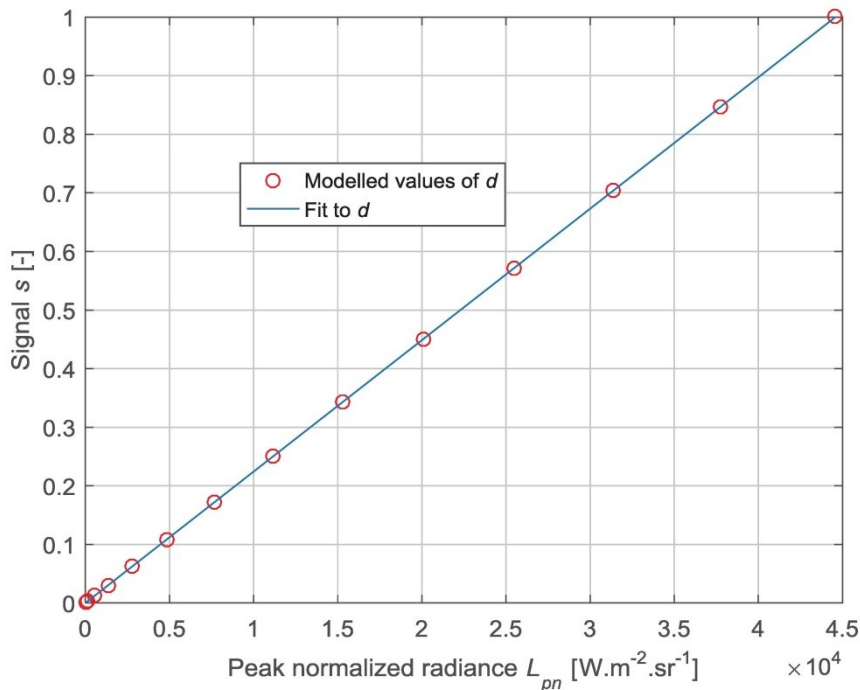


**Fig. 3.** The modelled signal values,  $s$ , resulting from the peak normalized radiance,  $L_{pn}(T)$ , at different blackbody temperatures.

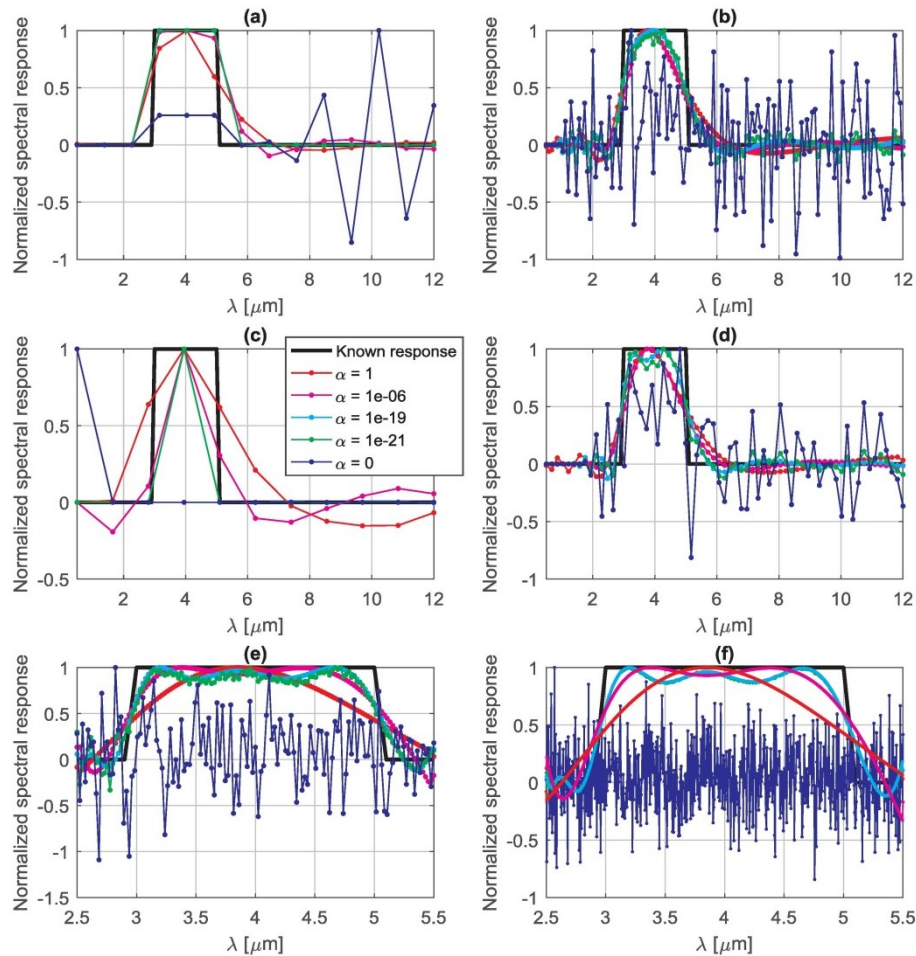


**Fig. 4.** The correct spectral response,  $r(\lambda)$ , used in the calculation of the instrument output signal,  $s$ , is shown by thick black curves together with the resolved response spectra,  $r_c$ , obtained by using different values of  $\alpha$  for modelled blackbody measurements with, (a)  $\Delta T = 100^\circ\text{C}$  covering the range  $100\text{--}1400^\circ\text{C}$ , the number of wavelength nodes equal to the number of temperatures, i.e.  $n = m = 14$  and therefore  $\Delta\lambda \approx 0.885\mu\text{m}$  over a wavelength range of  $\lambda = 0.5\text{--}12\mu\text{m}$ . Note that cyan and green curves lie on top of each other. (b)  $\Delta T = 10^\circ\text{C}$  covering the range  $100\text{--}1400^\circ\text{C}$ , with  $n = m = 131$ ,  $\Delta\lambda \approx 0.088\mu\text{m}$  over  $\lambda = 0.5\text{--}12\mu\text{m}$ . (c)  $\Delta T = 10^\circ\text{C}$  covering the range  $200\text{--}300^\circ\text{C}$  with  $n = m = 11$ ,  $\Delta\lambda \approx 1.15\mu\text{m}$  over  $\lambda = 0.5\text{--}12\mu\text{m}$ . Note that cyan and green curves lie on top of each other. (d)  $\Delta T = 10^\circ\text{C}$  covering the range  $100\text{--}1400^\circ\text{C}$  with  $n = 65 \approx \frac{1}{2}m$ ,  $\Delta\lambda \approx 0.18\mu\text{m}$  over  $\lambda = 0.5\text{--}12\mu\text{m}$ . (e)  $\Delta T = 10^\circ\text{C}$  covering the range  $100\text{--}1400^\circ\text{C}$  with  $n = m = 131$ ,  $\Delta\lambda \approx 0.023\mu\text{m}$  over  $\lambda = 2.5\text{--}5.5\mu\text{m}$ . (f)  $\Delta T = 2^\circ\text{C}$  covering the range  $100\text{--}1400^\circ\text{C}$  with  $n = m = 651$ ,  $\Delta\lambda \approx 0.005\mu\text{m}$  over  $\lambda = 2.5\text{--}5.5\mu\text{m}$ . Note that cyan and green curves lie on top of each other. (For interpretation of the references to colour in this figure legend, the reader is referred to the web version of this article.)

solution is stable, although not that accurate; at the smallest value of  $\alpha = 0$  (i.e. no regularization), the solution becomes erratic, with extreme values outside the MWIR response wavelength band; over some optimal range of  $\alpha$  values, between  $\alpha = 10^{-19}$  and  $\alpha = 10^{-21}$  in this case (note that the green coloured curve lies on top of the cyan coloured curve), the resolved response spectrum appears to be reasonable in comparison with the correct spectrum shown in black (in spite of its calibration curve in Fig. 2 seeming less than adequately accurate). The value of  $\alpha$  can also be obtained from the  $\alpha$  values used in the calculation of the corner point(s) of the L-curve shown in Fig. 5, calculated from  $\alpha = 10^0, 10^{-2}, 10^{-4}, \dots, 10^{-26}, 10^{-28}$ . The values of  $\alpha$  for the three points clustered in the corner position of the curve are  $\alpha = 10^{-18}, 10^{-20}$  and  $10^{-22}$ , which agrees with the results obtained from the visual inspection. The L-curves obtained for the remainder of the solutions shown in Fig. 4b–f (discussion to follow hereafter) all had optimal  $\alpha$  values over this wide range, with small to no distinction that could be made between their solutions.

Modelling of the measurements of the previous paragraph were repeated over the same blackbody temperature range of  $100\text{--}1400^\circ\text{C}$

but with an increase in the number of temperatures from  $m = 14$  to  $m = 131$ , with the resultant value of the constant temperature interval decreasing from  $\Delta T = 100^\circ\text{C}$  to  $\Delta T = 10^\circ\text{C}$ . The modelling parameter  $n$  was again set equal to the now larger value of  $m$ . Using these ‘measurements’, the resolved spectra in Fig. 4b are now smoother for the three largest values of  $\alpha$  due to the higher wavelength resolution, although these spectra are not necessarily better solutions than those obtained in Fig. 4a. A value of  $\alpha = 1 \times 10^{-21}$  was found to give a relatively good recovery of the response spectrum, although instability is already starting to show. The value of  $\alpha = 0$  results in a totally erratic response spectrum.

Fig. 4c shows the recovered response spectra for the same temperature interval of  $\Delta T = 10^\circ\text{C}$  between different blackbody modelled measurements as used for Fig. 4b, but for a much narrower temperature range of  $T = 200\text{--}300^\circ\text{C}$ . The most useable solution was also found at  $\alpha = 10^{-21}$ . Although the wavelength resolution of the spectrum is not ideal ( $n = m = 11$ ), the recovered response can still be used in determining the wavelength band in which the instrument operates (clearly MWIR in this case). This solution is, however, not as good as



S.J.P. Retief

Infrared Physics and Technology 92 (2018) 249–265

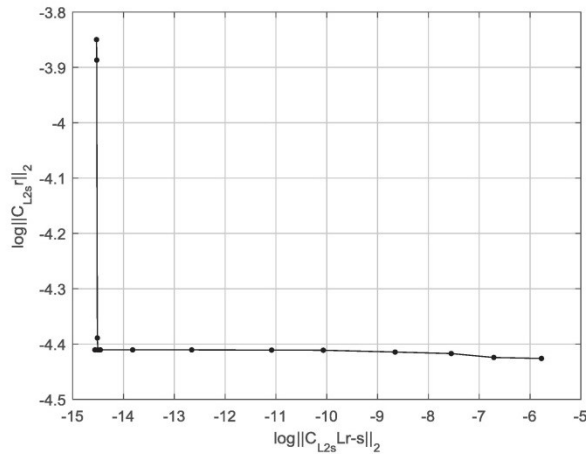


Fig. 5. The L-curve of the solutions shown in Fig. 4a. The  $\alpha$  value(s) used for the calculation of the data points in the corner of the curve give the optimal value (s) of  $\alpha$ . The  $\alpha$  values used in the calculation of the curve was  $\alpha = 10^0, 10^{-2}, 10^{-4}, \dots, 10^{-26}, 10^{-28}$ .

that obtained in Fig. 4a and b.

In Fig. 4d, the same temperature range and interval was used than in Fig. 4b, but with  $n \approx \frac{1}{2}m$  (now an overdetermined system of measurement equations). Although the wavelength resolution is half that than for Fig. 4b, the quality of the best recovered response spectra ( $\alpha = 10^{-19}$ – $10^{-21}$ ) appears to be similar than that of Fig. 4b.

The parameter values used in obtaining the recovered spectra shown in Fig. 4e are the same as those used for Fig. 4b, except for the wavelength range which was chosen to be relatively narrow around the MWIR band, i.e.  $\lambda = 2.5$ – $5.5 \mu\text{m}$ , and the resulting smaller value of  $\Delta\lambda \approx 0.023 \mu\text{m}$  (i.e. higher wavelength resolution). It can be seen that the recovered response spectrum in Fig. 4e ( $\alpha = 10^{-19}$ – $10^{-21}$ ) agrees more closely to the correct spectrum than that shown in Fig. 4b.

The spectra shown in Fig. 4f were obtained by increasing the temperature resolution used for Fig. 4e by setting  $\Delta T = 2^\circ\text{C}$  with a resulting change from  $\Delta\lambda \approx 0.023 \mu\text{m}$  to  $\Delta\lambda \approx 0.005 \mu\text{m}$ . Comparison of the recovered high resolution spectra of Fig. 4f and the lower resolution spectra of Fig. 4e yields little difference between them, as was the case in the comparisons of Fig. 4b with Fig. 4a and Fig. 4b with Fig. 4d.

The spectral recovery of synthetically generated data is now further explored in order to illustrate that the technique is also able to recover spectra of more complex shapes than that of the 3–5  $\mu\text{m}$  block response used so far.

From Eq. (5) it is clear that due to the dependency of  $L_{pn}(T)$  on  $r(\lambda)$ , different shapes of  $r(\lambda)$  should result in different  $L_{pn}$  vs.  $T$  curves. Fig. 6b illustrates the calibration curves of peak-normalized radiance calculated from Eq. (5) as a function of blackbody temperature (similar to curves in Fig. 2) covering  $T = 50$ – $500^\circ\text{C}$  with  $\Delta T = 10^\circ\text{C}$  as modelled for the different instrument spectral responses shown in Fig. 6a. These calibration curves (Fig. 6b) differ from each other as a result of the mentioned differences in the spectral responses – note how some curves cross each other, indicating that these curves do not just differ by a scaling factor.

Using an adequate temperature and wavelength range and resolution (cf. the discussion on the curve accuracies in Fig. 2), the spectral response should be resolvable from the curves of Fig. 6. In order to demonstrate this claim, the resolved normalized response spectrum of each of these instrument response curves are shown in Fig. 7. In each case, the wavelength range was chosen as to tightly fit around the known response spectrum. This can always be done for any unknown  $r(\lambda)$  by firstly recovering the spectrum over a wide wavelength region, as shown in Fig. 4a–d, and then narrowing down on the wavelength region in which  $r_\alpha(\lambda)$  is shown to have a non-zero response, as was done

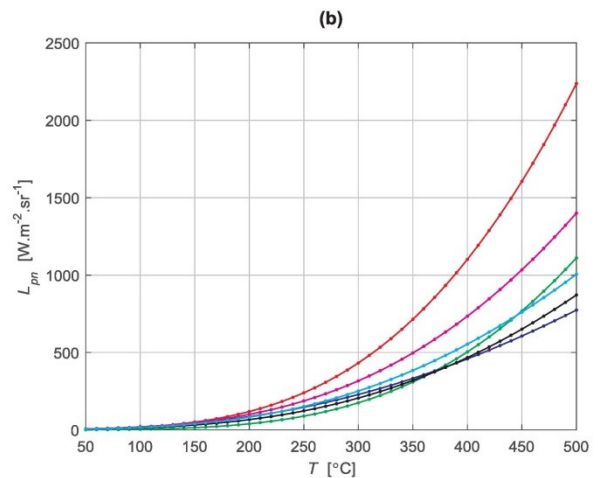
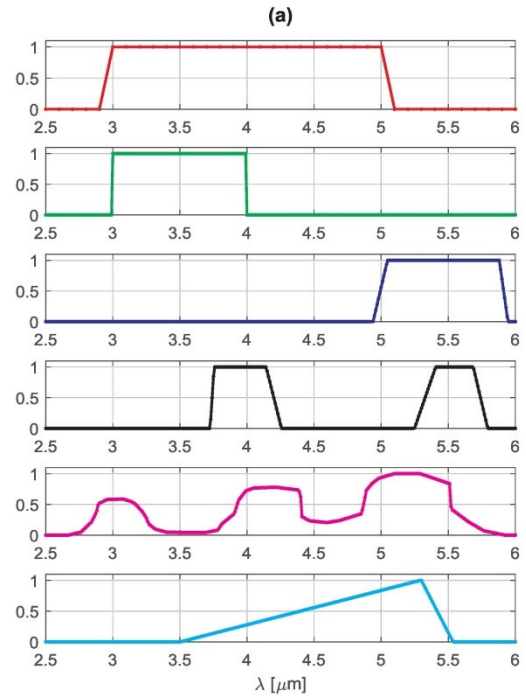


Fig. 6. The (b) modelled peak-normalized radiance,  $L_{pn}(T)$ , as a function of blackbody temperature,  $T$ , as calculated from (a) different normalized response spectra  $r(\lambda)$ . The colours and line types of the spectra in (b) agrees with the colours used in (a). (For interpretation of the references to colour in this figure legend, the reader is referred to the web version of this article.)

in Fig. 4e–f. The optimal values of  $\alpha$  were obtained from the method of visual inspection as well as the L-curve procedure.

### 2.3. Insights gained from applying the technique to the modelled measurements

During the application of Tikhonov regularization in Eq. (16) to the data as modelled by Eq. (9), the value of the regularization parameter  $\alpha$  was obtained on the basis of visual inspection of the computed solution as well as from the L-curve selection method. During the visual inspection method, the order of magnitude of the smallest value of  $\alpha$ , which is supposed to give the best representation of the actual response function, was easily (and quickly) obtained by calculating the solution

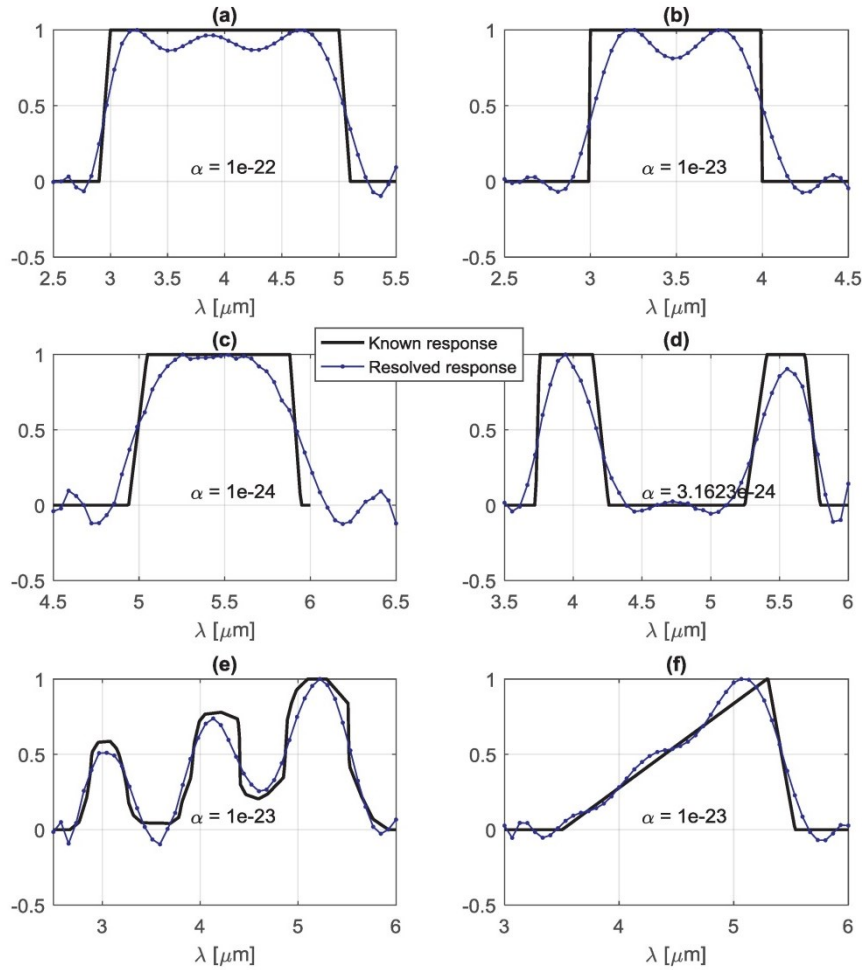


Fig. 7. The resolved normalized spectral response of the various, arbitrary response spectra shown in Fig. 6, for  $T = 50\text{--}500\text{ }^\circ\text{C}$  and  $\Delta T = 10\text{ }^\circ\text{C}$ . The number of wavelength nodes was chosen such that  $n = m$ .

$r_\alpha(\lambda)$  for a decreasing series of  $\alpha$  values. The value of  $\alpha$  to be used is that which almost results in numerical instability of the computed solution – this could just as easily be seen in the results of Fig. 4. Changes to the value of  $\alpha$  within the correct order of magnitude do typically not result in any critical changes to the computed solution, so that the visual inspection method with systematic experimentation with the  $\alpha$  value is a viable method of resolving the response spectrum.

Determination of the optimal value of  $\alpha$  using the L-curve method resulted in answers which were in good agreement with the visual inspection method. In some cases, more than one data point cluttered together in the corner of the L-curve. The use of the  $\alpha$  values of these cluttered data points resulted in recovered spectra which were mostly indistinguishable from each other, thus giving a range of optimal  $\alpha$  values.

Although the study in Section 2.2 on the behaviour of the applied technique with respect to the different measurement and modelling parameters was not exhaustive, some important insights could still be gained:

- The number of wavelength nodes  $n$  should be large enough to enable accurate modelling of  $L_{pn}$  in the measurement equation, Eq. (9). It would therefore be good practice to set  $n$  equal to the maximum value for which the system of measurement equations is not underdetermined, i.e. a square system with  $n = m$ . The implication is

that the number of temperatures  $m$  should be sufficient to allow accurate modelling of  $L_{pn}$ .

- Although higher values of  $n$  results in a recovered response spectrum with higher wavelength resolution, it does not guarantee the increased stability of the solution.
- A wider range of temperature values resulted in a better solution of the response spectrum, so that it is advisable to cover the widest possible temperature range that can be measured.
- Since complex shapes generally require more data points to describe them, complex response spectra can only be described by spectral response data with sufficiently high wavelength resolution, specified by  $n$ . However, if  $n$  is too large (and therefore  $\Delta\lambda$  too small),  $L_{i,j}$  and  $L_{i,j+1}$  become very close in value, resulting in columns  $j$  and  $j + 1$  of matrix  $\tilde{L}$  to be nearly equal. These nearly equal columns cause  $\tilde{L}$  to be almost singular, and  $L^{-1}$  can be expected to exhibit poor behaviour [15]. Other quadrature schemes than the Trapezoidal method, possibly better fitted to the combination of blackbody curve and expected shape and region covered by the response spectrum, can be used and might improve the numerical results [15].
- The modelling wavelength range should fit tightly around the expected wavelength region covered by the response spectrum. If this region is unknown, the calculations can be started over a wide range, and then repeated over a narrower range after the region of active spectral response has been determined.



Resolving the IFK in Eq. (4) not only requires a regularization method, but also subject knowledge regarding the problem at hand. In this respect, it is known that the normalized spectral responsivity is bounded by  $0 \leq r(\lambda) \leq 1$ . Finalization in resolving  $r_\alpha(\lambda)$ , e.g. the spectra shown in Figs. 4 and 7, can be obtained by imposing responsivity boundaries of  $r_\alpha(\lambda) = 0$  for all negative values of  $r_\alpha(\lambda)$ . Furthermore, from knowledge of the detector material (e.g. InSb or HgCdTe) when working with a real instrument and qualitative transmission properties of the optical system (e.g. knowledge of the infrared band for which the lens was manufactured, e.g. LWIR), it should be known whether only one (Fig. 7a–c and f) or several (Fig. 7d and e) wavelength regions of non-zero spectral responsivity exist. If only one region exists, then all  $r_\alpha(\lambda) > 0$  can be set to zero in wavelength regions suspected not to partake in the instrument responsivity. In order to determine whether the adjustments to  $r_\alpha(\lambda)$  during finalization of the resolution has not wrecked the true response  $r(\alpha)$ , the left hand side of Eq. (9) can be calculated using  $r_\alpha(\lambda)$ , i.e.  $\mathbf{Lr}_\alpha$ , and its relationship with the measured  $\mathbf{s}$  can be tested (as in Fig. 3) to determine whether the expected linear dependency exists. Any major deviation from this assumed linear relationship would indicate an inadequately resolved responsivity. Care must however be taken if it is known that the instrument has such a nature that the output signal varies non-linearly with the observed radiance. In such a case, the non-linearity must first be characterised and then an attempt can be made to linearize the output signal [23,24], after which the outlined technique can possibly be applied.

### 3. Determining the spectral response of an infrared camera

The spectral response for a (2003 model) Cedis Jade III MWIR camera, our camera under investigation (CUI), with a cooled InSb SCD Gemini detector was determined using the three methods mentioned in Section 1, i.e. theoretically, purely experimentally and by using the technique outlined in Section 2.1. This camera has an image resolution of  $320 \times 240$  pixels with a field of view (FOV) of approx.  $11^\circ \times 8^\circ$  obtained by using a 50 mm lens with an f-number of  $f/\# = 2$ .

#### 3.1. Theoretically and purely experimentally

Theoretically, the spectral responsivity for this instrument can be written as

$$\mathfrak{R}_{instr}(\lambda) = \mathfrak{R}_{detector}(\lambda)\tau_{dewar}(\lambda)\tau_{ar}(\lambda)\tau_{lens}(\lambda) \quad (19)$$

where  $\mathfrak{R}_{detector}(\lambda) = k\eta(\lambda)\lambda$  is detector responsivity,  $k$  is a constant,  $\eta$  is the spectral quantum efficiency and  $\tau_{dewar}(\lambda)$ ,  $\tau_{ar}(\lambda)$  and  $\tau_{lens}(\lambda)$  are the spectral transmissions of the dewar window, anti-reflection coating on the dewar window and the lens respectively. The normalized detector spectral responses would then be

$$r_{detector}(\lambda) = \frac{\mathfrak{R}_{detector}(\lambda)}{\mathfrak{R}_{detector}(\lambda_d)} \quad (20)$$

and the normalized instrument response is

$$r_{instr}(\lambda) = \frac{\mathfrak{R}_{instr}(\lambda)}{\mathfrak{R}_{instr}(\lambda_0)}, \quad (21)$$

where  $\mathfrak{R}_{detector}(\lambda)$  has a maximum value at  $\lambda_d$  and  $\mathfrak{R}_{instr}(\lambda)$  has a maximum value at  $\lambda_0$ . Typically representative transmission data of  $\tau_{dewar}(\lambda)$  and  $\tau_{ar}(\lambda)$  for this camera model were obtained from the manufacturer and are shown in Fig. 8 together with  $r_{detector}(\lambda)$  and  $r_{instr}(\lambda)$ . The silicon lens, with its own anti-reflection coatings, has a flat transmission spectrum in the MWIR region (not shown in the figure).

The spectral response of two camera models identical to the CUIs, one with a 50 mm lens ( $r_{instr1}$ ) and the other with a 100 mm lens ( $r_{instr2}$ ), were obtained purely experimentally with the use of a circular variable filter (CVF) wheel (model S134-LR of Optical Coatings Laboratory Inc.) [25]. The spectral responses so obtained are also shown in Fig. 8. It can be seen that these response curves differ from the theoretically

determined curve, and they also differ from each other (although not much) – this indicates the probable deviations of the manufactured components of the camera from the typical data available on these components. The experimentally determined camera responses will be considered as the most accurate representation of their actual response spectra, with the response spectrum of the camera with the 50 mm lens that will be used as a reference spectrum to verify any resolved spectrum against.

#### 3.2. Resolving the instrument response by the proposed technique

The measurement with an ideal instrument of the infrared radiation from an object of interest, with no influences on the measurement by the environment, was described in Section 2.1. The CUI is, however, a real instrument subjected to influences from its environment and a realistic model of the signal output from the instrument should be constructed before attempting to resolve its spectral responsivity.

##### 3.2.1. Refinement of the proposed technique for a non-ideal instrument

When the CUI is observing a blackbody, the measurement equation for the total signal output of the camera,  $s_{tot}$ , can be modelled (cf. [26,27]) by

$$s_{tot} = \frac{d}{dt}[s(T) + s_e(T_e) + s_d(T_d) + \dots]t + \Delta s, \quad (22)$$

where  $s(T)$  is the component of  $s_{tot}$  originating from the observed blackbody radiance (as defined in Section 2.1),  $s_e(T_e)$  is the component of  $s_{tot}$  originating from the inside environment of the camera which has stabilized at the camera internal temperature,  $T_e$ , and  $s_d(T_d)$  is the signal component resulting from the detector dark current, which is dependent on the detector temperature,  $T_d$ . The contribution of these components are all dependent on the integration time setting,  $t$ , of the camera during a measurement. Any possibly remaining integration time dependent signal components are represented by “...” in Eq. (22). Any  $t$  independent contributions to  $s_{tot}$ , like an offset in the readout circuitry, is represented by  $\Delta s$ . The influence of the outside environment is considered to be limited to the blackbody radiance when observed over a small distance, so that atmospheric radiation (path radiance) and attenuation are assumed to be negligible.

If, before the start of a set of measurements, the camera has stabilized in an environment with a controlled and constant climate, the values of  $T_e$  and  $T_d$  and probably any other remaining  $t$  dependent parameters, can be considered as constant so that the dependency of  $s_{tot}$  on the variables  $T$  and  $t$  can be explicitly written as

$$s_{tot}(T, t) = \frac{ds(T)}{dt}t + \frac{d}{dt}[s_e(T_e) + s_d(T_d) + \dots]t + \Delta s. \quad (23)$$

The blackbody contribution is separated from the rest of  $t$  dependent terms in the above equation. The first goal is to determine the value of  $s(T)$ , when having only available the values of  $s_{tot}(T, t)$  for given blackbody temperatures and integration times. This goal is addressed by removal of the blackbody during a measurement so that the remainder of the terms, resulting from the instrument being a real instrument as opposed to an ideal instrument, can be determined. With the values of these terms known, the value of  $s(T)$  can easily be determined.

If a blackbody, or any other object, with temperature of  $0K$  is measured by an ideal instrument under a non-intervening environment, the instrument should have a zero output signal. When measured with a real instrument, like the CUI, the contribution of the first term in Eq. (23) should be zero, so that the measurement equation for this measurement now becomes

$$s_{tot}(T = 0K, t) = \frac{d}{dt}[s_e(T_e) + s_d(T_d) + \dots]t + \Delta s. \quad (24)$$

After substitution of Eq. (24) into Eq. (23), the measurement



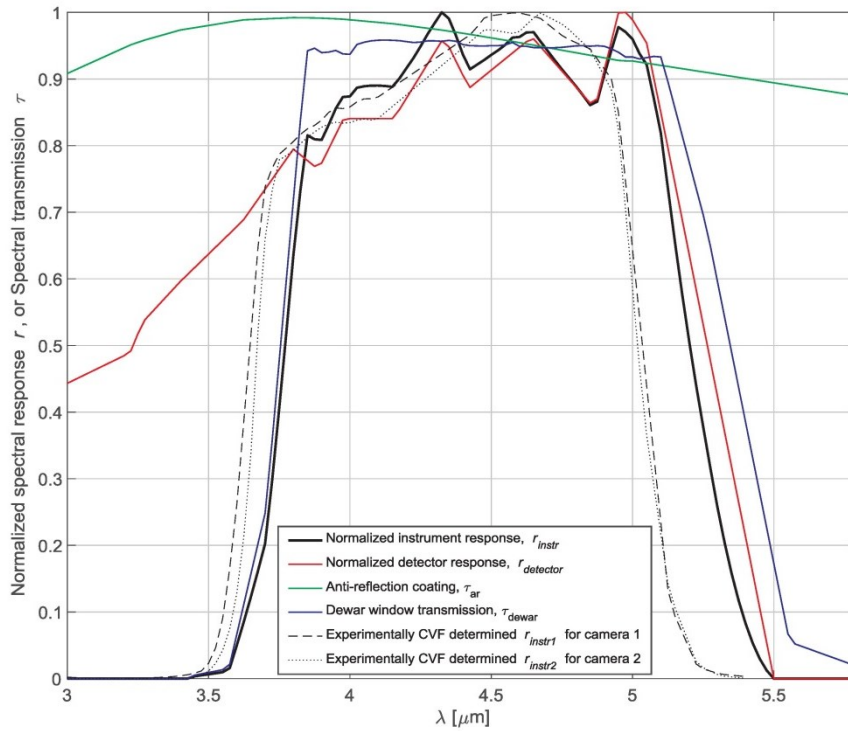


**Fig. 8.** The spectral transmissions of the optical components ( $\tau_{ar}$  and  $\tau_{dewar}$ ) and normalized detector responsivity ( $r_{detector}$ ) of the MWIR camera, together with the normalized instrument response ( $r_{instr}$ ) calculated from these variables and experimentally determined instrument responses ( $r_{instr1}$  and  $r_{instr2}$ ) by using a CVF.

equation becomes

$$s_{tot}(T, t) = \frac{ds(T)}{dt}t + s_{tot}(T = 0 \text{ K}, t), \quad (25)$$

and the value of  $s(T)$  is obtained as

$$\frac{ds(T)}{dt}t = s_{tot}(T, t) - s_{tot}(T = 0 \text{ K}, t), \quad (26)$$

i.e. for a given integration time  $t = t_k$ ,

$$s(T, t_k) = s_{tot}(T, t_k) - s_{tot}(T = 0 \text{ K}, t_k). \quad (27)$$

Resolvment of the normalized spectral response  $r(\lambda)$  can now be attempted by replacement of the signal from an ideal instrument  $s(T)$  in Eq. (4) by  $s(T, t_k)$ , i.e.

$$C_{L2s} \int_{\lambda_a}^{\lambda_b} r(\lambda) L_{bb}(T, \lambda) d\lambda = s_{tot}(T, t_k) - s_{tot}(T = 0 \text{ K}, t_k). \quad (28)$$

The components of the signal vector  $s$  in Eq. (16) are, for the specific  $t_k$  used during measurements, now set to

$$s_i = s_{tot}(T_i, t_k) - s_{tot}(T_i = 0 \text{ K}, t_k) \quad (29)$$

after which  $r_{\alpha}$  can be resolved.

### 3.2.2. Measurement setup and results

Measurements were obtained after alignment of the CUI with each of two types of blackbodies, a cavity blackbody and a flat-plate calibrator, respectively. The 25 mm aperture cavity blackbody, an EOI model CS1250-100, has an emissivity of 0.97 to 0.99 with a stability of  $\pm 0.25^\circ\text{C}$  [28] and was calibrated by an accredited service provider over the temperature range of  $50^\circ\text{C}$  to  $1200^\circ\text{C}$  with a measurement uncertainty of  $\pm 5^\circ\text{C}$ . The Fluke 9133 portable infrared calibrator, shown in Fig. 9, has a target circular area with diameter of 57 mm, stability of  $\pm 0.1^\circ\text{C}$  and is capable of covering a temperature range of  $-30^\circ\text{C}$  to  $150^\circ\text{C}$ . Its target area plate was painted with Nextel 811-21, having an approximate constant spectral emissivity of 0.97 [29] over

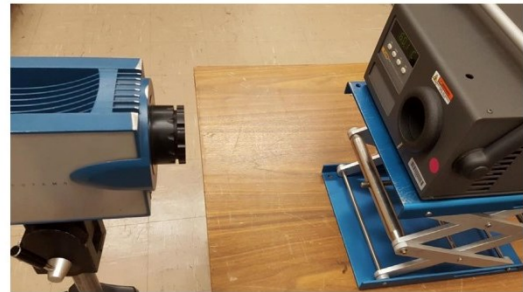


**Fig. 9.** The MWIR camera under investigation aligned with a flat-plate blackbody.

the MWIR band. The accuracy of its temperature settings is not known.

The output signal  $s$  of the CUI is a 14-bit digitized voltage signal, with dynamic range of  $0-16383(2^{14}-1)$  digital levels [DL], also called grey levels. Signal values above  $14000DL$  are not used in order to stay well clear from any saturation effects close to the camera's saturation level of  $16383DL$ . Before starting any measurements at a specific integration time  $t$ , a two-point non-uniformity correction (NUC) of the image pixels is done by means of measurements of a uniform flat-plate filling the FOV of the camera.

The cavity blackbody was used for high temperature measurements (above the upper limit of the flat-plate blackbody) using a short integration time, while the flat-plate blackbody was used for lower temperatures recorded with longer integration times. Measurements were done within a climate controlled environment after the CUI's internal temperature has stabilized, thereby attempting to keep the output signal originating from the camera's internal emission constant. The temperature of the camera detector is always kept constant during operation at  $75\text{K}$  by its own internal control system, thereby maintaining the dark current at a constant level.

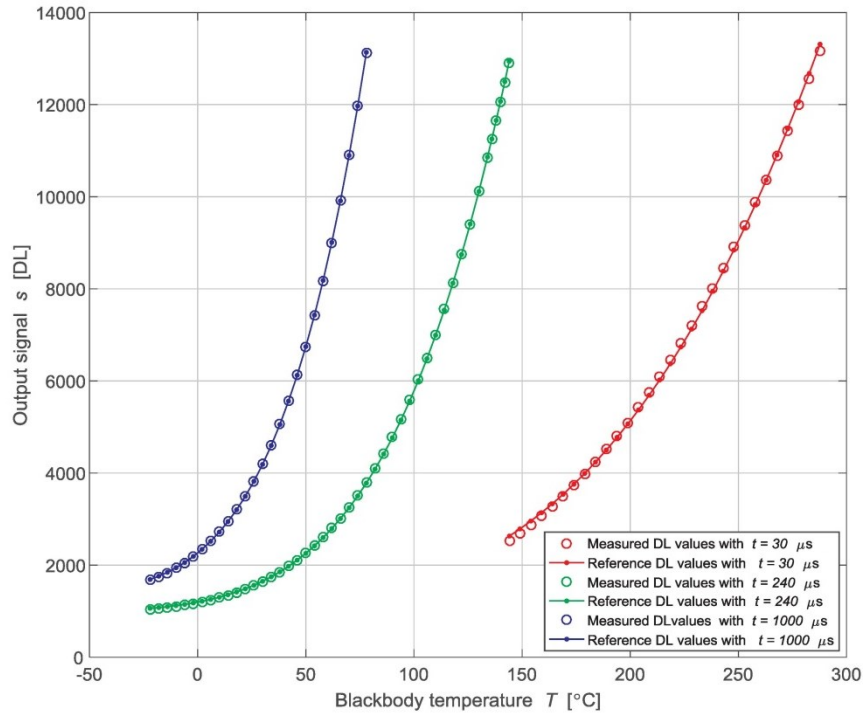


**Fig. 10.** The measured instrument output signals (circular markers) as a function of blackbody temperature. The cavity blackbody was used for integration time  $t = 30\mu\text{s}$ , while the flat plate blackbody was used for  $t = 240\mu\text{s}$  and  $t = 1000\mu\text{s}$ . Also shown is the reference  $s$  values (solid markers and lines) obtained by fitting the measured  $s$  to the calculated  $L_{pn}$  (shown in Fig. 11) by using the reference spectrum  $r_{instr1}$  in Section 3.1. Note the small differences between the measured and reference  $s$  values, especially for  $t = 30\mu\text{s}$ .

To realize Eq. (24), measurements of liquid nitrogen (77K) over a short range of about 10cm were considered as sufficient in order to ensure that no measurable, external blackbody/object radiation is observed by the camera. It was then attempted to do measurements of the blackbody over the widest temperature range possible (without the addition of a neutral density filter to the CUI) – for this reason three different integration times, collectively covering the lowest up to the highest temperatures measurable by the CUI, were used. The recording of a sequence of at least 100 image frames over 5–10 s of each of the blackbodies at each of the temperature settings  $T_i$  followed. The values of  $\Delta T$  was  $\sim 5^\circ\text{C}$  over the temperature range [144, 288] °C for the integration time  $t = 30\mu\text{s}$  with  $m = 26$ ,  $\sim 4^\circ\text{C}$  over the temperature range for  $t = 240\mu\text{s}$  (except for the highest temperatures for which  $\Delta T$  was decreased to  $\sim 2^\circ\text{C}$ ) with  $m = 45$  and  $\sim 4^\circ\text{C}$  over the temperature range [–22, 78] °C for  $t = 1000\mu\text{s}$  with  $m = 30$ . In consideration of the uncertainties related to the blackbodies' settings, stability and exact output spectra, values of  $\Delta T$  much smaller than  $\sim 5^\circ\text{C}$  was not considered sensible. Fig. 10 shows the measured output signal  $s$  of a group of  $4 \times 4$  pixels (averaged over the 16 pixels in each image frame as well as over the sequence of the recorded frames) near the centre of the recorded images as function of the blackbody temperature  $T$  at the different CUI integration times respectively. It can be seen that the three integration times span different blackbody temperature ranges and that the number of blackbody temperatures at which measurements were made within these ranges differ.

The internal temperature of the camera was kept as constant as possible, although during the  $t = 30\mu\text{s}$  measurements, the camera temperature still varied by up to  $2^\circ\text{C}$ ; during the  $t = 240\mu\text{s}$  and  $1000\mu\text{s}$  measurements, it was possible to maintain the camera temperature variation below  $0.3^\circ\text{C}$ . Although an NUC was applied for each integration time, such a correction is rarely ever perfect over a wide range of recorded temperatures, so that small variations between pixel values will persist. In spite of an imperfect NUC, different selections of pixels

did not influence the results significantly – experimentation with  $DL$  values obtained from single pixels or groups of pixels at different positions in the image did not have any significant influence on the solutions to be presented in Section 3.2.3. However, it is expected that as the quality of the NUC worsens, the measurement results will be negatively influenced with a subsequent negative effect on the spectral response resolutions.

Fig. 11a, c and e show the measured signals  $s$  at the three different values of  $t$  vs. the peak-normalized values  $L_{pn}$ , with  $L_{pn}$  calculated from Eq. (6) by employing the reference response spectrum  $r_{instr1}$  (of Section 3.1). As mentioned in Section 3.1,  $r_{instr1}$  is considered as the most accurate representation of the actual response spectra of the CUI, and a linear relationship is expected between  $s$  and  $L_{pn}$ , especially for this CUI [26]. Deviations from such a linear relationship are therefore considered to be the result of measurement inaccuracies resulting from the blackbody source and CUI and not of an inadequate/inaccurate responsivity spectrum of the CUI (as might be the case as stated at the end of Section 2.3).

A least squares straight line fit was applied to the measured  $s$  and  $L_{pn}$  data in order to determine the deviation of the measured  $s$  values from the fitted line. The difference between the measured values and the values predicted by the fitted line, which will be referred to as the reference  $s$  values, is shown in Fig. 11b, d and f for the three respective integration times, with the associated Root Mean Square Error (RMSE) also indicated in the figure caption. It is expected that more accurately known spectra from the blackbody instrument and a more stable measuring instrument would result in an improved  $s$  vs.  $L_{pn}$  straight line fit with a smaller RMSE.

### 3.2.3. Resolving the camera normalized spectral response

An important difference between the modelled measurements of Section 2.2 and the real measurements obtained with the CUI in this



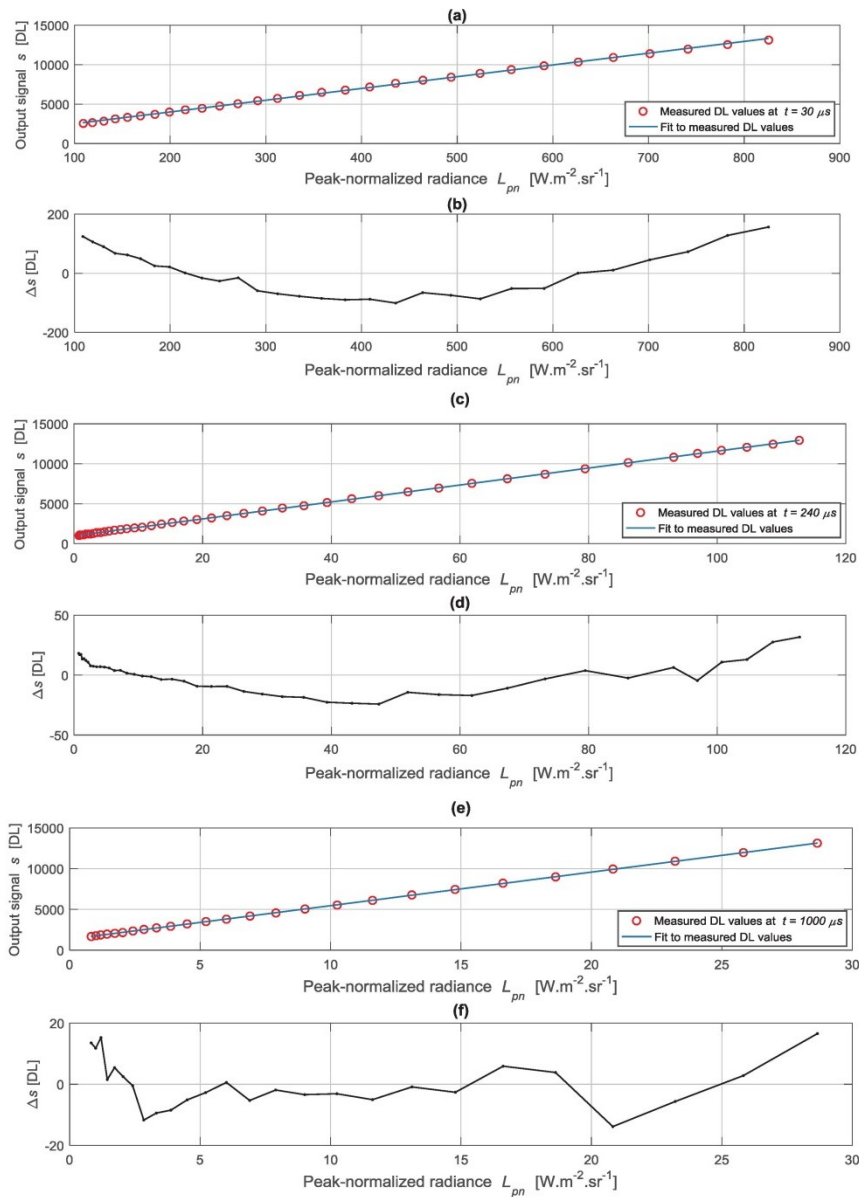


**Fig. 11.** The camera measured output signal  $s$  (red circles) vs.  $L_{pn}(T)$ , with  $L_{pn}(T)$  calculated from Eq. (6) using  $n_{instr}$  for (a)  $t = 30 \mu s$ , (c)  $t = 240 \mu s$  and (e)  $t = 1000 \mu s$ . The straight blue line in each graph is the least squares fit to the data. The difference between the straight line fit and the measured signal values for the three different  $t$  values used in (a), (c) and (e) are shown in (b) with  $RMSE = 74.4$  (0.45% of dynamic range), (d) with  $RMSE = 13.3$  (0.08% of dynamic range) and (f) with  $RMSE = 7.8$  (0.05% of dynamic range) respectively. (For interpretation of the references to colour in this figure legend, the reader is referred to the web version of this article.)

section is the measurement inaccuracies present in the real recordings. As mentioned in Section 2.1 when Wing [15] was quoted, small changes in the measured data may produce wild behaviour in the solution so that the solution have to be tamed using various means. Although great care was taken doing the CUI calibration type measurements as accurately as possible with the available equipment, non-ideal features of the measurements existed in the form of uncertainties of the emissivity, stability and temperature settings of the two blackbodies. Furthermore, variations occurred in the internal temperature of the CUI during the measurements (which would have an influence on the recorded DL values), in spite of a conscience effort to control and stabilize its environment. However, processing of the different sets of data obtained for the different integration times from the two different types of

blackbodies used, with all the uncertainties involved, is considered to be a good test for the consistency of the proposed technique.

Recovery of the CUI response spectrum was attempted by using the measured DL values as shown in Fig. 10, as well as the reference  $s$  (DL) values obtained from the straight line fit to the data which can be considered as a more accurate set of measurements. Recovered spectra were obtained for a range of  $\alpha$  values for each integration time, using as modelling parameter values both a wide wavelength range covering 1–12  $\mu m$  and a narrower range covering 3–6  $\mu m$  during the application of Eq. (16). The results for the reference DL values are discussed first, where after the solutions for the measured DL values are discussed.

Starting with the CUI reference DL recordings done with integration time  $t = 30 \mu s$  of  $m = 26$  temperatures over the range [144, 288] °C with



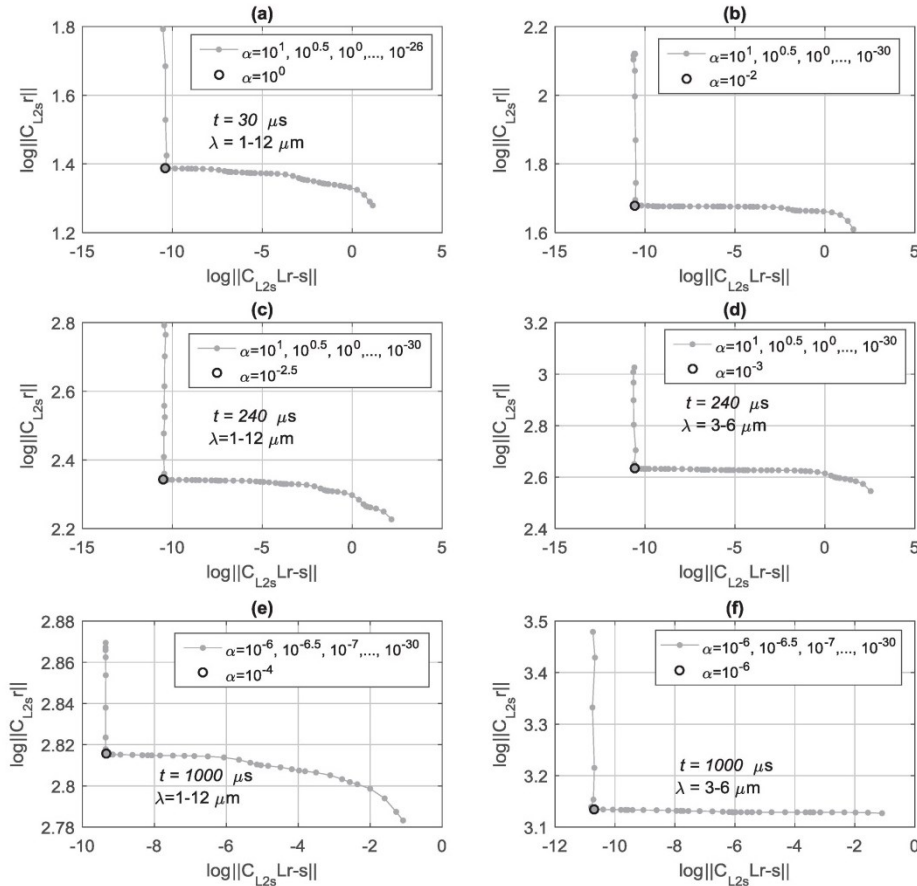


**Fig. 12.** The L-curves obtained from the response spectra as recovered from the *reference* data. The integration time and wavelength region used during recovery are shown for each graph. The  $\alpha$  values used for the creation of the L-curves are also indicated (grey solid markers), as well as the  $\alpha$  value associated with the corner point of the curve (black circle). (For interpretation of the references to colour in this figure legend, the reader is referred to the web version of this article.)

$\Delta T \approx 5^\circ \text{C}$ , solutions of the spectral response were obtained with the modelling parameters  $n = 26$  (i.e.  $\Delta \lambda \approx 0.38 \mu\text{m}$ ) and  $[\lambda_1, \lambda_m] = 1-12 \mu\text{m}$  for  $\alpha = \{10^1, 10^{0.5}, 10^0, \dots, 10^{-26}\}$ . The logarithmic values of the solution norms  $\|C_{L2s}, r\|$  and residual norms  $\|C_{L2s}, Lr-s\|$ , as associated with the solutions resulting from each  $\alpha$  value, were plotted against each other to obtain the L-curves as shown in Fig. 12a. The corner position obtained from  $\alpha = 10^0 = 1$  was easily identified and are marked in the figure. The recovered response spectrum associated with this  $\alpha$  value is shown by the black curve in Fig. 13a. Identification of the active response region within the wide band covering 1–12  $\mu\text{m}$  can easily be identified as the 3–6  $\mu\text{m}$  MWIR band, so that the modelling wavelength range was subsequently narrowed down to 3–6  $\mu\text{m}$ . The L-curve for this narrowed wavelength band, with a corner point associated with  $\alpha = 10^{-2}$ , is shown in Fig. 12b with the resulting recovered spectrum shown by the black curve in Fig. 13b. It can be seen that this recovered spectrum, which represents the best solution for all the  $\alpha$  values, is a reasonable representation of the known  $r_{instr1}$  spectrum shown in blue.

The recovered spectra associated with the corner point  $\alpha$  values in the remaining figures Fig. 12c–f for the *reference* DL recordings with integration times  $t = 240 \mu\text{s}$  and  $1000 \mu\text{s}$ , as solved over  $[\lambda_1, \lambda_m] = 1-12 \mu\text{m}$  and 3–6  $\mu\text{m}$ , are shown in Fig. 12c–f respectively. The similarities in the recovered response spectra solved over the 1–12  $\mu\text{m}$  range are easily observed, as is the case for the spectra solved over 3–6  $\mu\text{m}$ .

The spectra were then also recovered for the *measured* DL values, i.e. from the ‘less accurate’ unadjusted measurements. In the same fashion as described above, L-curves were obtained from solutions associated

with different  $\alpha$  values – these L-curves are shown in Fig. 14. The solutions obtained for the  $\alpha$  values of the corner points of the curves are plotted in red in Fig. 13. It was found that not all spectra recovered using these  $\alpha$  values gave acceptable results – this was the case for the spectra shown in Fig. 13d and f. Acceptable solutions were found by visual inspection for the data points indicated in green on the L-curves; the solutions calculated with the associated  $\alpha$  values are also plotted in green in Fig. 13d and f. Also shown in Fig. 13e is the slightly improved solution of the response spectrum when the  $\alpha$  value of the data point next to the corner point of the L-curve in Fig. 14e was used.

In Fig. 15 the theoretical and experimentally CVF determined (*reference*) response spectra of Section 3.1 are shown together with some of the resolved spectra based on the solutions shown in Fig. 13. Finalization in resolving the spectra were done according to procedure described in Section 2.3, i.e. all negative values were changed to zero and any non-zero responses separated from the main response settled in the 3.5–5.5  $\mu\text{m}$  region were also changed to zero. A few remarks can be made regarding the shown spectra:

- There is a reasonable (though not perfect) agreement in the wavelength position of maximum values of the resolved spectra with that of the reference spectrum  $r_{instr1}$ .
- The theoretically adjusted signal values compare relatively well with  $r_{instr1}$ , and compare better than the theoretically calculated response spectrum  $r_{instr}$ .
- In comparing the resolved spectrum using the unadjusted signal measurements with that obtained by using the theoretically adjusted

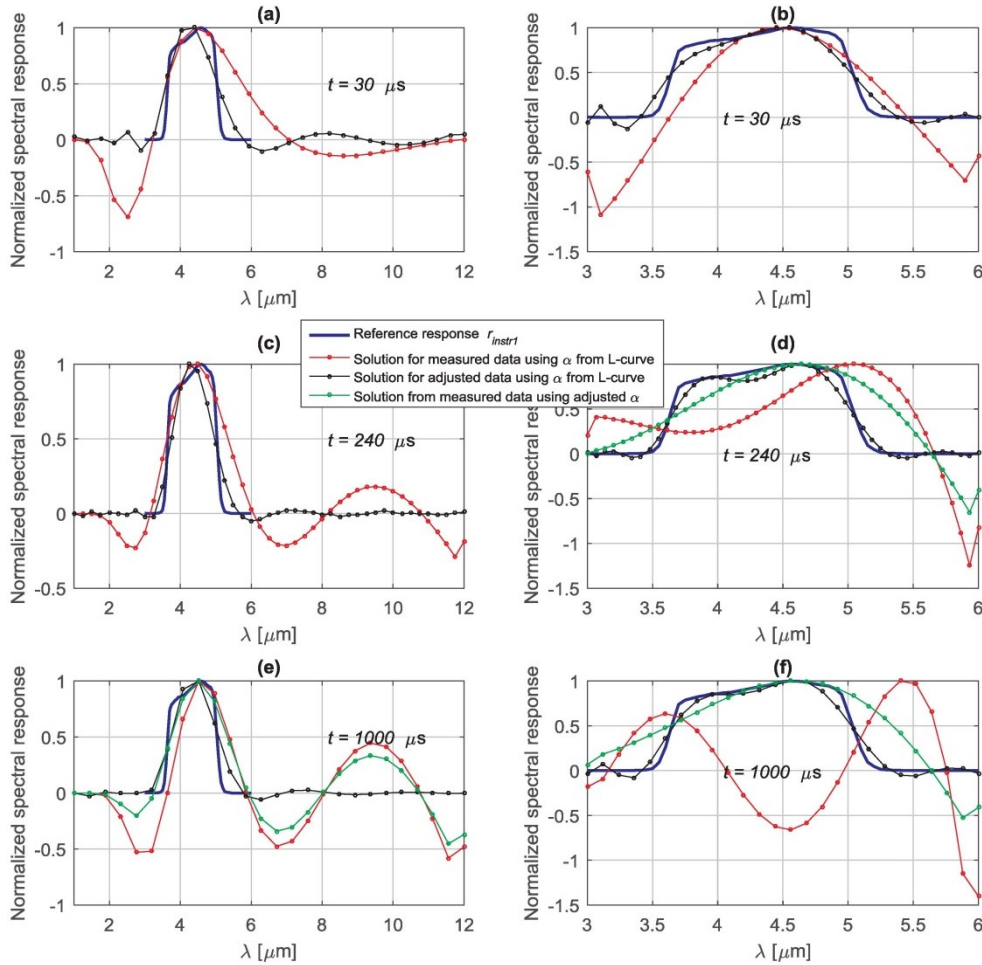


Fig. 13. The known spectral response  $r_{instr}$  (in blue) and the solutions to the spectral response of the CUI from measurements (in red) and theoretically adjusted reference measurements (in black) at different integration times, as indicated on the plots, and for the different wavelength ranges of  $\lambda = 1\text{--}12\mu\text{m}$  and  $\lambda = 3\text{--}6\mu\text{m}$  used as input. The applicable parameters used in obtaining these solutions are shown in the corresponding sub-figures of Fig. 12 and Fig. 14. (For interpretation of the references to colour in this figure legend, the reader is referred to the web version of this article.)

signal measurements, it can be inferred that measurements made with improved accuracy would result in improved spectral response recovery.

#### 4. Conclusion

A technique was presented for resolving the spectral response of a wide-band infrared measuring instrument based on calibration type measurements of a blackbody at different temperatures and the mathematical technique as outlined in Section 2. The technique addresses the solution of a Fredholm integral equation of the first kind, which describes blackbody measurements by the measuring instrument. It was shown that during the attempt to solve the instrument response spectrum, subject matter knowledge is required in tailoring the inputs to the technique as well as the initial solution produced by the technique, and hence this process is referred to as ‘resolving’ the response spectrum.

A significant part of the mathematical technique is centred on the Tikhonov regularization method used during the inversion of the radiance matrix in the Fredholm equation, which is constructed from modelled values of blackbody spectra. The suitability of the blackbody spectral model, and thus the accuracy of the radiance matrix, is subject to the fidelity of the commercially available blackbody source instruments in accurately representing Planck’s law in their emission spectra

at different temperature settings.

The technique was first tested by means of error-free, synthetically generated instrument output signals resulting from a ‘measured’ blackbody source. It was shown that the solutions obtained from the synthetic signals for the response spectra were in reasonable agreement with the response spectra used in the generation of these signals. The accuracy of the resolved spectra is highly dependent on the value of the regularization parameter  $\alpha$  – a larger value of  $\alpha$  results in a more stable solution, but with lower accuracy, whereas a smaller value of  $\alpha$  results in a more accurate solution, but with an increasing tendency of instability. The method of visual inspection as well as the L-curve method were explained and used to obtain optimal  $\alpha$  values, which can typically cover a range of values.

It is stated by Wing [15] that the optimal value of  $\alpha$  is not only determined by the matrix to be inverted ( $\tilde{L}$  in this work), but also by the statistical distribution of the error in the data and the data itself; this can be confirmed by the attempt to recover the response spectrum of an IR camera by using real calibration type measurements, considered to contain relative large uncertainties, that were done with the camera. In this respect, not all response spectra could be successfully recovered by the L-curve method, and the method of visual inspection had to be employed in order to obtain reasonable response spectra. The measurements made were then also adjusted to be representative of



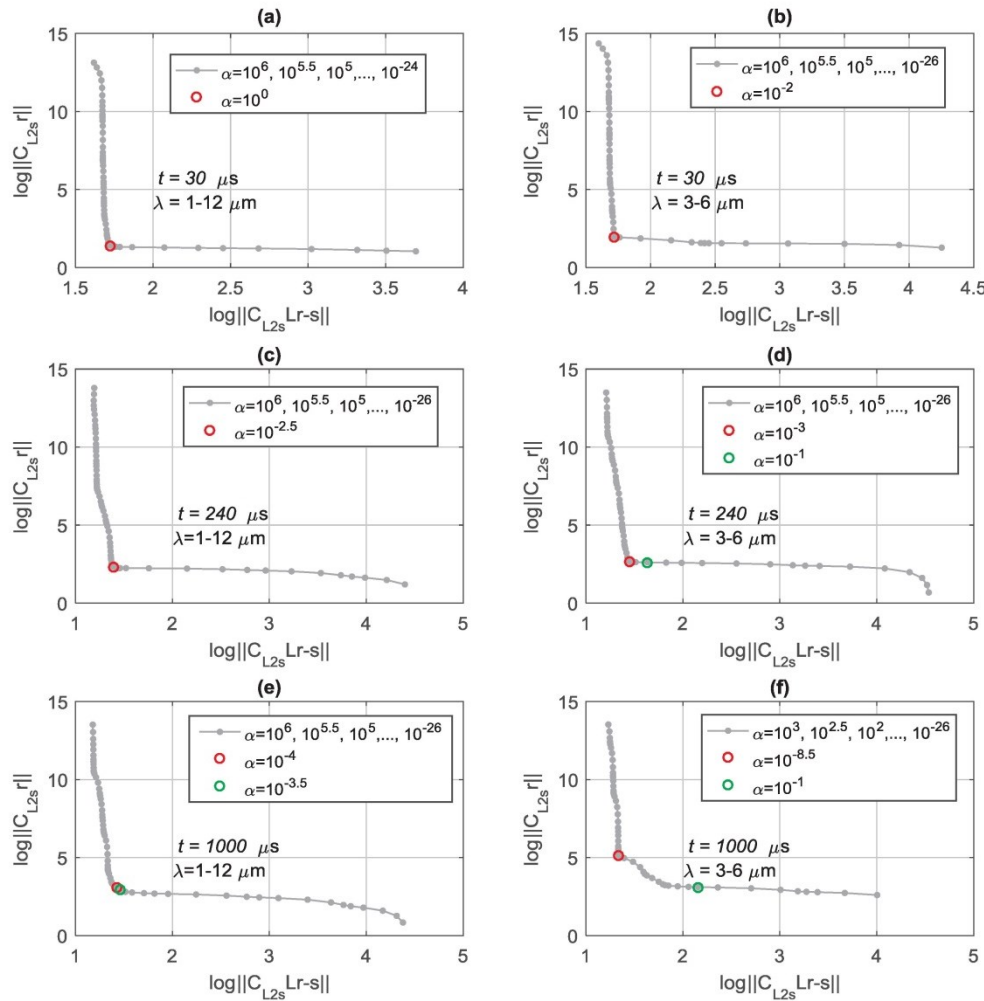


**Fig. 14.** The L-curves obtained from the response spectra as recovered from the *measured* data. The integration time and wavelength region used during recovery are shown for each graph. The  $\alpha$  values used for the creation of the L-curves are also indicated (grey solid markers), as well as the  $\alpha$  value associated with the corner point of the curve (red circle) and the  $\alpha$  value resulting in the best visual agreement with the known response spectrum (green circle). (For interpretation of the references to colour in this figure legend, the reader is referred to the web version of this article.)

more accurate measurements, after which the instrument spectrum could be recovered with great success by using only the L-curve method. In consideration of these results, together with the results of the error free synthetic data, it seems that the technique requires a high degree of accuracy in the measurements in order to be applied successfully. Quantification of the required degree of accuracy, as well as the investigation into possible improvements of the presented method, is foreseen in future research.

In the use of the response spectrum during normal data reduction activities for obtaining the IR characteristics of objects of interest (as described in Section 1), differences in the actual response spectrum and the resolved response spectrum might, under certain operational circumstances, become less critical – for example, for measurements of objects over long distances, the atmosphere introduces a cut-off for radiation with  $\lambda > 5\mu\text{m}$  in the MWIR band (easily verifiable using radiative transfer code like Modtran™). Such an environmental filter would make the over-extension of a resolved response spectrum to wavelengths longer than  $5\mu\text{m}$  (see e.g Fig. 15) of little consequence during data reduction when used together with the modelled atmospheric spectral transmission.

Other infrared sources with known emission spectra can also be

used after appropriate modification of the radiance matrix, which could result in a more stable matrix inversion. Also, other methods than Tikhonov regularization for stable matrix inversion exist and need to be investigated for possible improved solutions when using measurements characterised by non-negligible margins of error.

Application of the technique can, besides instrument spectral response recovery, also be extended to optical filter transmission characterization if high accuracy measurements are possible, or at least filter transmission band identification of unspecified filters when only lower accuracy measurements are possible.

**Acknowledgements**

The author would like to acknowledge and thank Dr. WH Gunter of the Institute of Maritime Technology in Simon's Town, South Africa, for supplying data on the experimentally determined response spectra of the camera under discussion. Special thanks are also extended to my colleagues Hannie van den Bergh and Neels Brink, as well as to Prof. A Kijko of the University of Pretoria, for valuable discussions regarding the topic of this research. This research did not receive any specific grant from funding agencies in the public, commercial, or non-profit



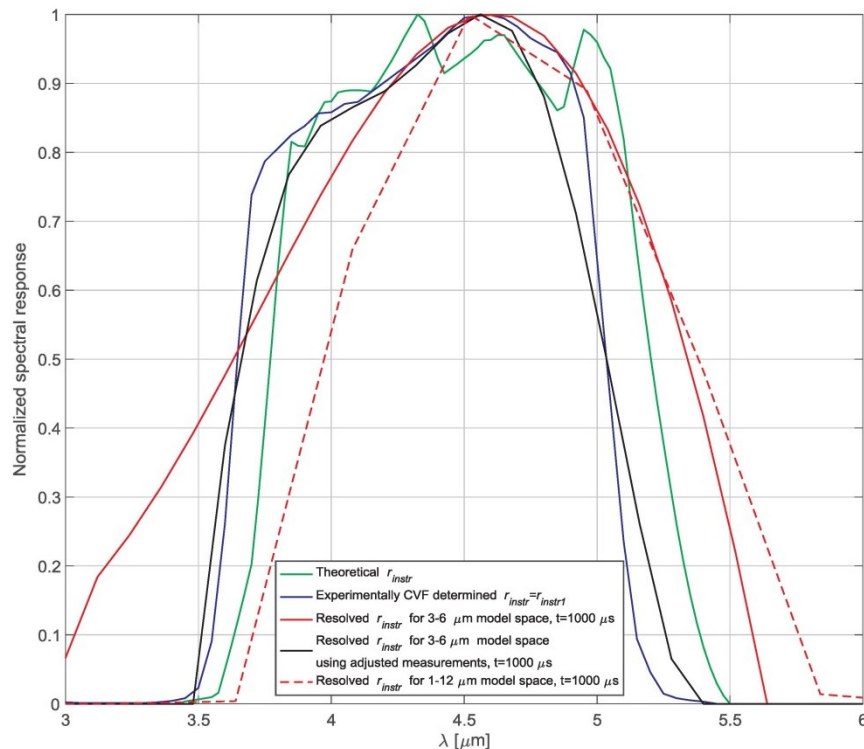


Fig. 15. The resolved spectral response for the CUI together with the theoretical and experimentally determined responses as presented in Section 3.1.

sectors.

## References

- [1] J.M. Palmer, B.G. Grant, Chapter 1 - Introduction to radiometry, *Art Radiom.* SPIE Press, Bellingham, 2009, pp. 1–9.
- [2] C.J. Willers, Chapter 3 - Sources, *Electro-Optical Syst. Anal. Des. A Radiom. Perspect.* SPIE - The International Society for Optical Engineering, Bellingham, 2013, pp. 57–96.
- [3] A. Rogalski, K. Chrzanowski, *Infrared devices and techniques (revision)*, *Opto-Electron. Rev.* 10 (2002) 111–136.
- [4] A. Rogalski, *Progress in focal plane array technologies*, *Prog. Quantum Electron.* 36 (2012) 342–473, <http://dx.doi.org/10.1016/j.pquantelec.2012.07.001>.
- [5] W.L. Wolfe, Chapter 14 - Radiometric temperatures, *Introd. to Radiom.* SPIE, 1000, 20th Street, Bellingham, WA 98227-0010, USA, 1998, pp. 143–149 <http://ebooks.spiedigitallibrary.org/book.aspx?doi=10.1117/3.287476>.
- [6] S.J.P. Retief, P. Smit, M.M. Dreyer, Mid-wave infrared characterization of an aircraft plume, in: *Saudi Int. Electron. Commun. Photonics Conf. 2011, SIEPCP 2011*, 2011, pp. 1–6. <http://doi.org/10.1109/SIEPCP.2011.5876932>.
- [7] J.M. Palmer, B.G. Grant, Chapter 5 - Detectors of optical radiation, *Art Radiom.* SPIE Press, Bellingham, 2009, pp. 127–213.
- [8] V.B. Podobedov, G.P. Eppeldauer, L.M. Hanssen, T.C. Larason, Calibration of spectral responsivity of IR detectors in the range from 0.6 μm to 24 μm, in: B.F. Andresen, G.F. Fulop, C.M. Hansen, P.R. Norton (Eds.), *Infrared Technol. Appl. XLII*, 2016, p. 98190P1–98190P11.
- [9] J.M. Palmer, B.G. Grant, Chapter 7 - Radiometric measurement and calibration, *Art Radiom.* SPIE Press, Bellingham, 2009, pp. 241–268.
- [10] C.J. Willers, Chapter 5 - Optical Detectors, *Electro-Optical Syst. Anal. Des. A Radiom. Perspect.* SPIE - The International Society for Optical Engineering, Bellingham, 2013, pp. 63–86, <http://dx.doi.org/10.1002/9781118014103.ch4>.
- [11] W.L. Wolfe, Chapter 9 - Normalization, *Introd. to Radiom.* SPIE, 1000, 20th Street, Bellingham, WA 98227-0010, USA, 1998 <http://ebooks.spiedigitallibrary.org/book.aspx?doi=10.1117/3.287476>.
- [12] C.L. Wyatt, *Radiometric Calibration: Theory and Methods*, 1978.
- [13] F.E. Nicodemus, Normalization in radiometry, *Appl. Opt.* 12 (1973) 2960–2973.
- [14] C.J. Willers, Chapter 7 - Radiometry techniques, *Electro-Optical Syst. Anal. Des. A Radiom. Perspect.* SPIE - The International Society for Optical Engineering, Bellingham, 2013.
- [15] G.M. Wing, *A Primer on Integral Equations of the First Kind*, Society for Industrial and Applied Mathematics, 1991, <http://doi.org/10.1137/1.9781611971675>.
- [16] W. Press, B. Flannery, S. Teukolsky, W. Vetterling, *Numerical Recipes in C: The Art of Scientific Computing*, second ed., Cambridge University Press, 2002.
- [17] R.C. Aster, B. Borchers, C.H. Thurber, *Parameter Estimation and Inverse Problems*, second ed., Elsevier, 2013 10.1016/B978-0-12-385048-5.00002-1.
- [18] P. Yang, X.-W. Feng, W.-J. Liang, K.-S. Wu, Numerical solutions of inverse black body radiation problems with Gaussian-Laguerre quadrature formula, *Int. J. Theor. Phys.* 54 (2015) 519–525.
- [19] C.W. Groetsch, Integral equations of the first kind, inverse problems and regularization: a crash course, *J. Phys. Conf. Ser.* 73 (2007) 012001.
- [20] S.J. Gibowicz, A. Kijko, Chapter 4 - Location of seismic events in mines, *An Introd. to Min. Seismol.* Academic Press Inc., 1994, pp. 48–71.
- [21] M.S. Zhdanov, Chapter 2 - Ill-posed problems and the methods of their solution, *Inverse Theory Appl. Geophys.* second Ed., Elsevier, 2015, pp. 33–61.
- [22] P.C. Hansen, Chapter 7 - Parameter-choice methods, *Rank. Discret. Ill-Posed Probl. Society for Industrial and Applied Mathematics*, 1998, pp. 175–208.
- [23] J.B. Shumaker, *Linearity Considerations and Calibrations*, Chapter 11, *Self-Study Man. Opt. Radiat. Meas.* National Bureau of Standards (U.S.) Tech. Note 910-3, 1984, p. 31.
- [24] C.L. Wyatt, *Radiometric Calibration: Theory and Methods*, Academic Press Inc., 1978.
- [25] W.H. Gunter, Institute for Maritime Technology, Personal communication, 2006.
- [26] L. Shkedy, O. Amir, Z. Calahora, J. Oiknine-Schlesinger, I. Szafrank, Temperature dependence of spatial noise in InSb focal plane arrays, in: E.L. Dereniak, R.E. Sampson (Eds.), *Infrared Detectors Focal Pl. Arrays VI*, SPIE - The International Society for Optical Engineering, 2000, pp. 481–488, <http://dx.doi.org/10.1117/12.391762>.
- [27] J.K. Ji, J.R. Yoon, K. Cho, Nonuniformity correction scheme for an infrared camera including the background effect due to camera temperature variation, *Opt. Eng.* 39 (2000) 936–940.
- [28] Electro Optical Industries Inc., CS SERIES High Temperature Sources specification sheet, 1999.
- [29] A. Adibekyan, E. Kononogova, C. Monte, J. Hollandt, High-accuracy emissivity data on the coatings Nextel 811–21, Herberths 1534, Aeroglaze Z306 and Aktkar Fractal Black, *Int. J. Thermophys.* 38 (2017) 1–14.

## CHAPTER 7 CONCLUSION

The solving of inverse radiometric problems arising from infrared measurements was addressed in this thesis in the following manner:

- A measurement equation describing objects being observed with an infrared instrument was formulated. Emphasis was placed on the measurement of a gaseous object in the form of an aircraft plume since the characteristics of this object are often of practical importance in the military environment. By selecting the terms of the measurement equation correctly, the measurement of solid type objects could also be described.
- Having the correct measuring equation as starting point, the inverse radiometric problem was formulated for obtaining a data reduction equation so that the source/absolute radiance values of the object under observation could be determined. The source radiance values were cleared from any unwanted influences on the measurements such as atmospheric transmission losses to the target object's radiation, atmospheric emission contributions to the target object's radiation, contributions from foreground reflections against the target, contributions from the background of the target as transmitted through transparent type targets, and the non-ideal response of the instrument to the measurements.
- It was shown how the inverse radiometric problem was formulated for an axi-symmetric aircraft plume from a radiative transfer modelling viewpoint. The solution of the inverse problem resulted in acquiring the inner radiance structure of the plume, which was then used to model the plume from any arbitrary observer position outside the plume.
- It was lastly shown that an inverse radiometric problem could be formulated for determining a wide-band infrared instrument's spectral response from calibration type measurements, without the need of a spectrally tuneable radiation source. Solving such an inverse problem is a non-trivial process that points towards strict requirements in terms of measurement accuracy. This work, however, opens an avenue towards the investigation of more techniques and methods to adequately address the retrieval of the spectral response of instruments by means of the described measurements.

The objectives that were addressed are seen to contribute towards the continual need for improved measurement methods and data reduction techniques in order to improve the accuracy of infrared models of objects of interest.



## REFERENCES

- [1] W.L. Wolfe, Chapter 2 - Radiometric quantities, the language, in: *Introd. to Radiom.*, SPIE, 1000 20th Street, Bellingham, WA 98227-0010 USA, 1998. doi:10.1117/3.287476.
- [2] S.J.P. Retief, M.M. Dreyer, C. Brink, Infrared recordings for characterizing an aircraft plume, in: M. du Plessis (Ed.), *Sensors, MEMS Electro-Optical Syst.*, SPIE - The International Society for Optical Engineering, 2014: p. 92570C. doi:10.1117/12.2066290.
- [3] S.J.P. Retief, P. Smit, M.M. Dreyer, Mid-wave infrared characterization of an aircraft plume, *Saudi Int. Electron. Commun. Photonics Conf. 2011, SIEPCP 2011.* (2011) 1–6. doi:10.1109/SIEPCP.2011.5876932. © 2011 IEEE, reprinted with permission.
- [4] F. Sircilli, S.J.P. Retief, L.B. Magalhaes, L.R. Ribeiro, A. Zanandrea, C. Brink, M. Nascimento, M.M. Dreyer, Measurements of a micro gas turbine plume and data reduction for the purpose of infrared signature modeling, *IEEE Trans. Aerosp. Electron. Syst.* 51 (2015) 3282–3293. doi:10.1109/TAES.2015.140392. © 2015 IEEE, reprinted with permission.
- [5] S.J.P. Retief, Aircraft plume infrared radiance inversion and subsequent simulation model, in: D.H. Titterton, M.A. Richardson (Eds.), *Technol. Opt. Countermeas. IX*, SPIE - The International Society for Optical Engineering, 2012: p. 85430P. doi:10.1117/12.970539.
- [6] S.J.P. Retief, A technique for resolving the spectral response of a wide-band infrared measuring instrument from measurements without the need for a spectrally tuneable radiation source, *Infrared Phys. Technol.* 92 (2018) 249–265. doi:10.1016/j.infrared.2018.06.004.
- [7] W.L. Wolfe, Chapter 1 - Introduction, in: *Introd. to Radiom.*, SPIE, 1000 20th Street, Bellingham, WA 98227-0010 USA, 1998: pp. 41579–41580. doi:10.1117/3.287476.
- [8] J.M. Palmer, B.G. Grant, Chapter 1 - Introduction to radiometry, in: *Art Radiom.*, SPIE Press, Bellingham, 2009: pp. 1–9.
- [9] B.G. Grant, *Field Guide to Radiometry*, SPIE Press, Bellingham, 2011.
- [10] C.J. Willers, Preface, in: *Electro-Optical Syst. Anal. Des. A Radiom. Perspect.*, SPIE - The International Society for Optical Engineering, Bellingham, 2013.
- [11] J.M. Palmer, B.G. Grant, Chapter 2 - Propagation of optical radiation, in: *Art Radiom.*, SPIE Press, Bellingham, Weinheim, Germany, 2009: pp. 17–37. doi:10.1002/9783527619269.ch2e.
- [12] R.W. Boyd, Chapter 2 - Radiometry, in: *Radiom. Detect. Opt. Radiat.*, John Wiley & Sons, Inc., 1983: pp. 13–27.
- [13] C.J. Willers, Chapter 2 - Introduction to radiometry, in: *Electro-Optical Syst. Anal. Des. A Radiom. Perspect.*, SPIE - The International Society for Optical Engineering, Bellingham, 2013: p. 184. doi:10.1117/3.287476.
- [14] X. Pan, X. Wang, R. Wang, L. Wang, Infrared radiation and stealth characteristics

- prediction for supersonic aircraft with uncertainty, *Infrared Phys. Technol.* 73 (2015) 238–250. doi:10.1016/j.infrared.2015.09.012.
- [15] K. Han, W. Lee, J.W. Hahn, Effect of spectral line broadening and instrument function on the spectrum of a mid-infrared flare in a realistic environment, *Combust. Sci. Technol.* 188 (2016) 1152–1164. doi:10.1080/00102202.2016.1174219.
- [16] B. Gu, S.W. Baek, H. Jegal, S.M. Choi, W.C. Kim, Infrared signature characteristic of a microturbine engine exhaust plume, *Infrared Phys. Technol.* 86 (2017) 11–22. doi:10.1016/j.infrared.2017.08.014.
- [17] H. Zheng, T. Bai, Q. Wang, F. Cao, L. Shao, Z. Sun, Experimental study of multispectral characteristics of an unmanned aerial vehicle at different observation angles, *Sensors.* 18 (2018) 428. doi:10.3390/s18020428.
- [18] F. Sircilli, S.J.P. Retief, B.L. Magalhaes, L.R. Ribeiro, A. Zanandrea, C. Brink, M. Nascimento, M.M. Dreyer, Infrared characterization of a micro turbine engine plume, in: *XV Simpósio Apl. Operacionais Em Áreas Def.*, 2013: pp. 107–112.
- [19] J.R. Fincke, Tomographic reconstruction of volume emission coefficients from line integral data, *Plasma Chem. Plasma Process.* 6 (1986).
- [20] R.J. Hall, P.A. Bonczyk, Sooting flame thermometry using emission/absorption tomography, *Appl. Opt.* 29 (1990).
- [21] H. Uchiyama, M. Nakajima, S. Yuta, Measurement of flame temperature distribution by IR emission computed tomography, *Appl. Opt.* 24 (1985).
- [22] J. Wen, Z. Liang, An inversion formula for the exponential Radon transform in spatial domain with variable focal-length fan-beam collimation geometry, *Med. Phys.* 33 (2006).
- [23] S. Bellini, M. Piacentini, C. Cafforio, F. Rocca, Compensation of tissue absorption in emission tomography, *IEEE Trans. Acoust.* 27 (1979) 213–218. doi:10.1109/TASSP.1979.1163232.
- [24] V.Y. Panin, G.L. Zeng, G.T. Gullberg, A Method of Attenuation Map and Emission Activity Reconstructon from Emission Data, *IEEE Trans. Nucl. Sci.* 48 (2001).
- [25] P.M. Brisley, G. Lu, Y. Yan, S. Cornwell, Three-dimensional temperature measurement of combustion flames using a single monochromatic CCD camera, *IEEE Trans. Instrum. Meas.* 54 (2005).
- [26] G. Gilabert, G. Lu, Y. Yan, Three dimensional visualisation and reconstruction of the luminosity distribution of a flame using digital imaging techniques, *J. Phys. Conf. Ser.* 15 (2005) 167–171.
- [27] W. Fischer, H. Burkhardt, Three-dimensional temperature measurements in flames by multispectral tomographic image analysis, in: A.G. Tescher (Ed.), *Proc. SPIE 1349, Appl. Digit. Image Process.* XIII, 1990: pp. 96–105. doi:10.1117/12.23521.